SISSA
Scuola
Internazionale
Superiore di
Studi Avanzati

Mathematics Area – PhD course in

Mathematical Analysis, Modelling, and Applications

Reduced order parameterized viscous optimal flow control problems and applications in coronary artery bypass grafts with patient-specific geometrical reconstruction and data assimilation

Candidate:
Zakia Zainib

Advisor:
Prof. Gianluigi Rozza
Co-advisor:
Dr. Francesco Ballarin

Academic Year 2018 - 19

To my parents and my sister, Aliza.

Abstract

***

Coronary artery bypass graft surgery is an invasive procedure performed to circumvent partial or complete blood flow blockage in coronary artery disease (CAD). In this thesis, we will construct a numerical framework combining parametrized optimal flow control and reduced order methods and will apply to real-life clinical case of triple coronary artery bypass grafts surgery. In this mathematical framework, we will propose patient-specific physiological data assimilation in the optimal flow control part, with the aim to minimize the discrepancies between the patient-specific physiological data and the computational hemodynamics. The optimal flow control paradigm proves to be a handy tool for the purpose and is being commonly used in the scientific community. However, the discrepancies between clinical measurements and computational hemodynamics modeling are usually due to unrealistic quantification of hard-to-quantify outflow conditions and computational inefficiency. In this work, we will utilize the unknown control in the optimal flow control pipeline to automatically quantify the boundary flux, specifically the outflux, required to minimize the data misfit, subject to different parametrized scenarios. Furthermore, the challenge of attaining reliable solutions in a time-efficient manner for such many-query parameter dependent problems will be addressed by reduced order methods.

Acknowledgements

***

This thesis has been kept on track and has been seen through to completion with the support and encouragement of numerous people. First of all, I would like to extend my gratitude to my advisor *Prof. Gianluigi Rozza*, for giving me this great opportunity of working under his keen and expert supervision. His valuable ideas and encouraging attitude played a vital role in the completion of this task. Thank you for teaching me to aim higher and broaden my horizons.

I would also like to warmly thank my co-advisor *Dr. Francesco Ballarin* for the detailed intellectual discussions, innovative ideas, and for the countless efforts of guidance. I am sincerely obliged to him for providing me with his valuable time, the insightful suggestions and support at every step of this expedition. Thank you for smoothing the academic path for me throughout this journey. I also want to express my gratitute to our collaborators, *Prof. Piero Triverio* and *Dr. Laura Jiménez-Juan* for the scientific support and for providing us with the surgical data.

I appreciate the support and help provided by the faculty members and the students of Mathematical Analysis, Modeling and Applications, specially by SISSA mathLab. My special thanks goes to my colleague and friend *Dr. Shafqat Ali* and his wife *Asma Shafqat* for the academic as well as emotional support throughout this journey. I would also like to thank my friends *Caruso*, *Mulita* and *Siddiqa* for always keeping my spirits up and for bearing my nuisances.

I would like to express my most warmth appreciation for the people who helped me reach where I stand today, my family, specially my mother and my late father who always believed in me. Lastly, I convey my deepest gratitude to my sister, who has been a best friend, an inspirational figure, a source of nothing but consistent support and love to me. Thank you *behna*, I owe you everything!

Zakia Zainib

Contents

***

Chapter 1

Introduction and Motivation

***

Congenital heart diseases such as coronary artery disease (CAD), that is atherosclerosis of coronary arteries, is among the top causes of morbidity worldwide. In CAD, plaque builds up inside the arteries, narrows them down and therefore, partially or completely blocks the oxygen-rich blood supply. Partially blocked supply can result in myocardial ischemia, that is, the heart muscle starves of oxygen and can result in angina. Furthermore, complete blockage can cause the death of heart muscle, medically known as myocardial infarction. This can lead to heart attack and hence, can be prove fatal. Cardiovascular diseases, in general, account for 31 % of global morbidity rate and 85 % of this is caused by myocardial infarction. From statistical point of view, recently carried out research have shown that heart failure is responsible for 3.9 million deaths per year in Europe only and 1.8 million deaths in European Union per year [77, 107]. Furthermore, heart attack kills about 0.735 million people in the United States every year [78] and the morbidity rate by strokes increased from 3% to 8% in England during $2011 - 13$ [25]. Thus, without a doubt, it

can be established that ischaemic diseases such as CAD, are the leading cause of death worldwide.

In less severe cases, the disease can be managed with a healthy life-style and medication, however, reasonably severe extent of the disease requires surgical treatments. Bypass graft surgery or heart bypass surgery is one of the possible invasive treatments to restore the blood supply to the heart muscle. In this surgical procedure, the blood flow blockage caused in congenital heart diseases is circumvented by attaching additional vessels after the point of blockage. The additional conduit act as an alternative pathway for the blood to flow. Patency rate of the coronary artery bypass grafts (CABGs) depends upon a number of factors, including extent of stenosis in diseased artery, the material used for graft vessels, shape and type of graft and patient-dependent factors such as age, weight and gender. While one cannot control the latter for patients, the former can however be managed by determining the hemodynamics parameters, such as blood flow velocity, wall shear stress, pressure drop and fractional flow reserve, through non-invasive computational fluid dynamics techniques. A-priori knowledge of hemodynamics behavior, depicted by the aforementioned parameters, in the grafted vessels contributes towards pre- and post-surgery clinical decisions, such as optimal treatment choice, optimal surgical device design, extent of blockage and its location, and patency of the surgical devices [83, 101, 105, 44].

Reliability and efficiency are vital characteristics for patient-specific computational hemodynamics models to be helpful in daily-based clinical decisions. Thanks to improved imaging and computational techniques, the patient-specific computational hemodynamics modeling [14, 104] has come a long way in terms of real-life geometries [11, 109, 32], prediction of best suitable shape of surgical device [17, 18] and modeling of patient-specific physiological data [96, 36]. Despite these accomplishments, the gap between patient-specific hemodynamics modeling and computational methods needs to filled. The discrepancies in this regard are usually ought to two critical factors, namely the boundary conditions and the computational inefficiency. The work in this thesis is directed towards addressing and overcoming these factors through parametrized reduced order optimal flow control framework with proposed patient-specific data assimilation from 4D-flow magnetic resonance images (MRIs) [33].

In this chapter, we will first familiarize the reader with the anatomy of coronary arteries and coronary artery bypass grafts. In the third section we will introduce the motivation and theme of this thesis and afterwards, we will cover some literature on the patient-specific computational hemodynamics modeling, optimal flow control problems and reduced order methods. Then, we will summarize the algorithm followed in this work to reconstruct patient-specific geometrical models of coronary artery bypass grafts from clinical images. We will end the chapter by presenting organization of this thesis.

We would like to acknowledge the scientific collaboration with Dr. *Stephen Fremes* and Dr. *Laura Jiménez-Juan* (*Sunnybrook Health Sciences Center, Toronto, Canada*), and Prof. *Piero Triverio* (*University of Toronto, Toronto, Canada*) and we express our gratitude for providing us with patient-specific medical images, that will be used in the geometrical

reconstruction part in the next sections.

1.1. Anatomical introduction: coronary arteries

In this section, we will give a general anatomical overview of coronary arteries. The coronary arteries arise from the aortic sinuses and converge towards the apex of the heart [110]. These arteries and their branches are responsible for infusing the entire heart muscle with oxygen-rich blood. Main branches can be namely classified as left coronary artery (LCA), right coronary artery (RCA), left anterior descending artery (LAD) and left circumflex artery (LCx). LCA and RCA originate from ascending aorta just above the aortic valve, otherwise known as coronary ostia, and LAD and LCx originate from the same main trunk of LCA (see figure 1.1.1). RCA, LAD and LCx are further divided into sub branches that will be overviewed in the upcoming discussion and we refer the reader interested in the anatomical details of coronary arteries to [58, 110, 7].

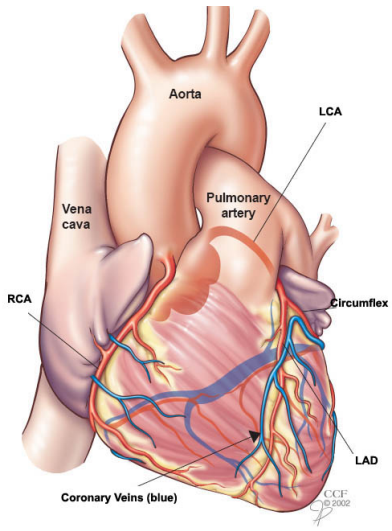

Figure 1.1.1: Anatomical introduction: coronary arteries (shown in red color), coronary veins (shown in blue color). Figure is courtesy of `my.clevelandclinic.org`.

1.1.1 Right coronary artery (RCA)

The right coronary artery originates from the right aortic sinus or sinus of Valsalva, passes anteriorly and to the right between the right auricle and the pulmonary artery, and then descends into the right atrioventricular groove. It bends at the crux of the heart and continuous posteriorly in the interventricular sulcus. It supplies blood to the right atrium, right ventricle, the sino-atrial and atrioventricular nodes, some posterior portion of left

ventricle and posterior part of interventricular septum. Its length ranges from $120mm$ to $180mm$ and typically it, first, branches off into conus artery, then a sinoatrial nodal artery, followed by the diagonal first and second acute marginal arteries (AM1, AM2). As it curves posteriorly onto the posterior surface of heart, it gives rise to atrioventricular nodal artery and terminates into posterior descending artery (PDA) and posterior left ventricular branch (PLV) (see figure 1.1.2(a)).

Acute marginal artery (AM)

Acute marginal artery (AM) is the longest branch of right coronary artery. It originates as RCA reaches the acute margin of the heart and continues towards cardiac apex and supplies anterior wall of the right ventricle (RV).

Posterior descending artery (PDA)

Posterior descending artery (PDA) runs along the diaphragmatic surface in the posterior interventricular sulcus toward the inferior septum and supplies posterior wall of left ventricle and posterior portion of interventricular septum. If the circulation is right dominant (in $\sim 60-65\%$), PDA is a branch of RCA. Otherwise RCA can peter out in acute marginal artery (in $\sim 35-40\%$) and in this case, known as left dominant, PDA is a branch of left circumflex artery (LCx).

1.1.2 Left coronary artery (LCA)

Left coronary artery (LCA), also known as left main coronary artery (LCMA), originates from left coronary ostia and runs in lateral direction behind pulmonary artery (PA), alongside heart walls and posterior to the right ventricular outflow tract. It has short main trunk and quickly bifurcates into LAD and LCx (see figure 1.1.2(a)). Owing to heterogeneity among humans anatomy, LCA can occasionally (in $\sim 15\%$) trifurcate into LAD, LCx and an additional intermediate branch, called *ramus intermedius*. In some cases, LCA can be absent and LAD and LCx can originate from left coronary ostia directly. LCA runs from 1 mm to 25 mm before bifurcating into LAD and LCx and supplies the left atrium, left ventricle and anterior portion of interventricular septum.

1.1.3 Left anterior descending artery (LAD)

Left anterior descending artery (LAD) continues from LCA and courses around left side of pulmonary artery (PA) in anterior atrioventricular sulcus, towards the apex of heart and anterior to the interventricular septum. Generally it runs from 100 mm to 130 mm and occasionally it gives rise to septal branches which run down along interventricular sulcus towards the apex. These branches are numbered from base to apex, that are, S1 and S2 and supply the two-third anterior of interventricular septum. Afterwards, LAD bifurcates

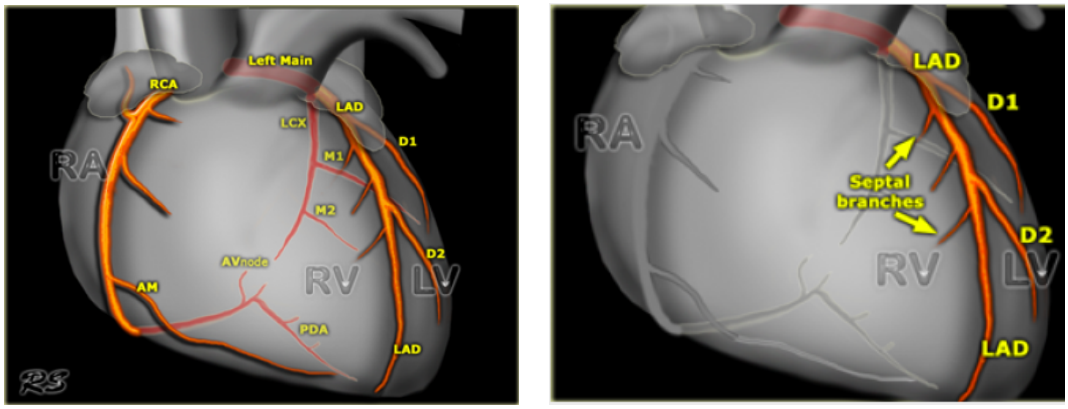

(a). (b).

Figure 1.1.2: (a). Right coronary artery (RCA), left main coronary artery (LMCA) and corresponding branches. (b). Left anterior descending artery (LAD) and its branches. Figures are courtesy of `www.radiologyassistant.nl`.

into diagonal branches that originate at acute angles and run diagonally towards the acute margin and the apex (see figure 1.1.2(b)).

Diagonal branch

Diagonal branches originate from LAD at acute angle and run over the left ventricle diagonally towards the acute margin and the apex of the heart. These branches are usually numbered from 2 to 9 and run parallel to each other. Generally first diagonal branch (D1) is more visible, however, in the presence of ramus intermedius the diagonal branches arise more distally and are less prominent [40, 58]. Around the apex, LAD connects with the terminal branches of PDA.

1.1.4 Circumflex artery (LCx)

Circumflex artery or left circumflex artery (LCx) originates as the other branch from the trunk of left main coronary artery, almost at 90 deg. It usually runs from 50 mm to 80 mm and it courses the left atrioventricular sulcus towards the crux of the heart (see figure 1.1.2(a)). However, occasionally it might diagonally descend upon the left ventricular side towards the apex of the heart and terminate at the mid portion of interventricular sulcus. This branch supplies most of the left atrium, the posterior and lateral free walls of the left ventricle, and part of the anterior papillary muscle of the bicuspid valve. It gives rise to anterior, marginal or posterior branches, with the names depend upon their corresponding points of origin and in left dominant case, it gives rise to PDA.

Obtuse marginal artery (OM)

Obtuse marginal artery branches off from left circumflux artery and travels along the left margin of the heart and descends towards its apex. These arteries are usually more than one and are numbered accordingly, for example, first obtuse marginal (OM1) and second obtuse marginal (OM2).

The general segmentation of these arteries in the case of left dominance and right dominance flows is shown in figure 1.1.3, where, proximal stands for close to ascending aorta or the artery of origin, mid is between proximal and distal and distal is stands for away from the aorta or the artery of origin. Moreover, apical means near the apex of heart.

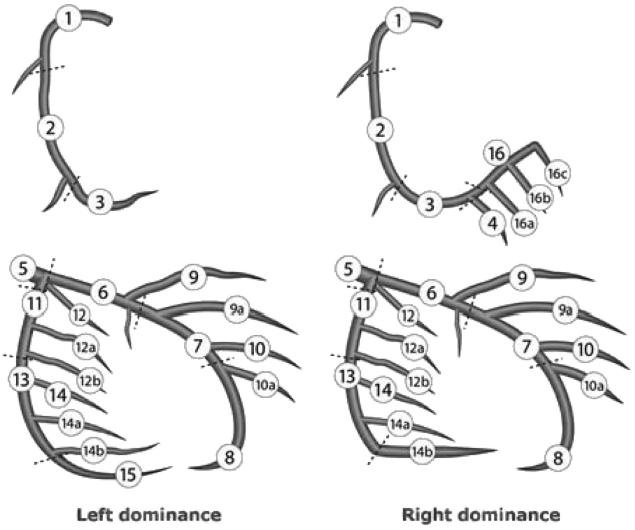

Figure 1.1.3: Segmentation of coronary arteries in left dominant (left) and right dominant (right) case according to SYNTAX `http://www.syntaxscore.com` [62, 111].

1. RCA proximal,
2. RCA mid,
3. RCA distal,
4. Posterior descending (right dominance),
5. Left main,
6. LAD proximal,
7. LAD mid,
8. LAD apical,
9. first diagonal,

$9a$. add. first diagonal,

10. second diagonal,

$10a$. add. second diagonal,

11. proximal circumflex,
12. intermediate/anterolateral,

$12(a), 12(b)$. obtuse marginal,

13. distal circumflex,

$14, 14a, 14b$. left posterolateral

15. posterior descending (left dominance),

$16, 16a, 16b, 16c$. posterolateral from RCA.

1.2. Anatomical introduction: Coronary artery disease and bypass graft surgery

Coronary artery disease (CAD) is the narrowing of coronary arteries due to plaque built up, leading to reduction in blood supply to the heart muscle. Cholesterol and fat deposits on the inner walls of the coronary arteries constitute this plaque and as it grows, the originally elastic arteries become more rigid and narrow, a process called atherosclerosis. The narrowed arteries allow less blood to flow and inadequate blood supply to the heart muscle can cause the oxygen starvation (ischemia). Varying with respect to degree of severity,

myocardial ischemia can result in heart ache, known as angina. In some cases, the particles from plaque can break up and through the blood stream, they can enter and get lodged in the smaller arteries. This can cause complete blockage of the blood supply and can lead to death of the heart muscle, otherwise known as myocardial infarction. Myocardial infarcation results in heart failure or heart attack and hence, death. Furthermore, atherosclerosis of coronary arteries and plaque rupture increase the chances of thrombosis, that is formation of blood clots that can travel to other arteries and cause the blockage.

Recent studies have marked inflammation as a major contributor in atherogenesis in coronary arteries and in all the stages of atherosclerosis [68, 69, 39]. Common risk factors for cardiovascular diseases, for example, smoking, high cholesterol, insulin-resistance, hypertension, high blood pressure and also, the aging can trigger production of impaired nitric oxide and loss of antithrombotic properties of the coronary endothelium cells. This, in turn, can augment the adhesion of blood leukocytes to the inner surface of the arterial wall. Once the leukocytes reside in the arterial intima, they communicate with endothelial and smooth muscle cells, which migrate into the intima. These cells proliferate a complex extracellular matrix that modulates the cell functions such as cell death, migration, activation, healing or destruction of the extracellular matrices of myocardium [69, 68].

Based on common symptoms of coronary artery disease such as chest pain, heartburn, fatigue, severe shortness of breath, nausea, etc., different clinical tests can be implemented for diagnosis purposes. Some examples include *blood tests* to check the level of risk factors such as cholesterol and sugar, etc., *stress tests* to examine the functioning of the heart under physical stress. Advanced and non-invasive medical imaging techniques can then be used to follow up on the initial confirmations. For example, *cardiac computed tomography (CT) scans* can detect the calcium deposits in the arteries and therefore, are used to detect the presence and extent of coronary artery disease, *cardiac MRIs (magnetic resonance imaging)* are used to detect the tissue problems and obstruction of blood flow, these can also further follow up the results of CT scans, and coronary angiography can detect the location of stenosis through injection of a colored dye. A prediction about extent of stenosis can be made by measuring the time taken by the dye to travel through the blocked artery.

The treatment choices for coronary artery disease vary according to the extent of disease, medical history of the patients and their age, etc. Thus, ranging from mild to severe degree of stenosis, the doctors recommend healthy life-style changes, medication and surgical procedures to open the blocked arteries. *Coronary artery bypass graft surgery* (CABG) is among the commonly practiced surgical treatments. Coronary artery disease can affect multiple vessels and accordingly in the coronary artery bypass graft surgery, new connections are made to the blocked vessels with the help of other arteries and veins extracted from other parts of body (see figure 1.2.1(a)). A schematic illustration of the graft connection techniques is shown in figure 1.2.1(b) for conventional end-to-side anastomosis. These external arteries are called *bypass grafts* and common choices for bypass grafts include internal thoracic artery, radial artery extracted from arm and saphenuous vein extracted from leg. The patency of bypass grafts takes many properties into account such as the

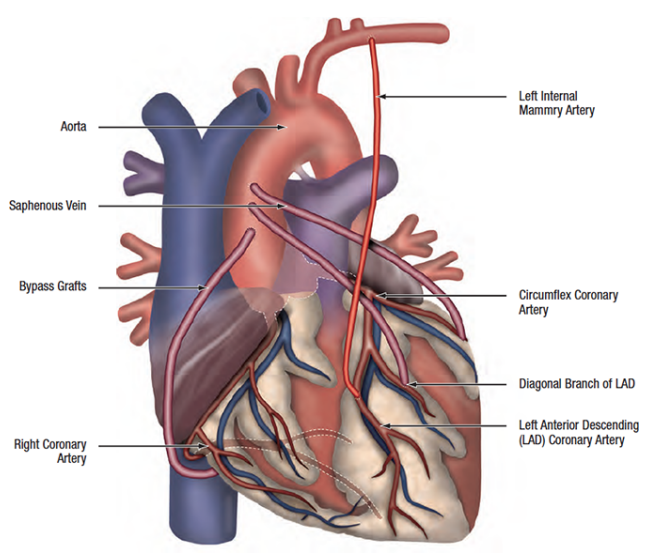

(a).

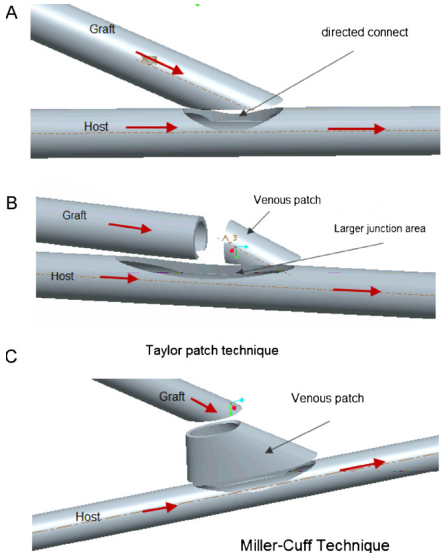

(b).

Figure 1.2.1: (a). Illustration of coronary artery bypass grafts, courtesy of `www.ottawacvcentre.com`. (b). Schematic illustration of conventional end-to-side anastomosis [83].

antithrombotic properties of the graft, compatibility at high blood flow rate, its diameter, length and compliance. Furthermore, arterial and vein grafts can tend to develop intimal hyperplasia, that is, thickening of intimal layer of the artery or vein because of cell deposits, and collapse within a time range of a few days to a few years post-surgery. The plaque development in these grafts has been associated to the angle of grafting, position of graft as well as the medical condition of the patient. About a decade ago, prosthetic grafts gained some popularity however their diameter is to be kept sufficiently large to avoid the atherosclerosis and hyperplasia and therefore, they are *not* implemented as coronary bypass grafts [59]. Next, we will discuss the common choices for coronary artery bypass grafts, namely internal thoracic artery, radial artery and saphenuous vein.

1.2.1 Graft choice: internal thoracic artery

Internal thoracic artery (ITA), also commonly known as *internal mammary artery (IMA)* is the most common choice for coronary arterial revascularization. It is usually classified as *right internal mammary artery* (RIMA) or (RITA) and *left internal mammary artery* (LIMA) or (LITA). In general, both are branches of subclavian artery and originate from its first portion. In some cases, LITA can orginate from the trunk with other arteries originating from the subclavian artery [48]. To be used as a graft, the artery is extracted

from its original position while in most cases, keeping the portion at origin intact (see figure 1.2.2(a)). ITA runs around 150 mm lateral to the sternum edge and it can be harvested using either skeletonized technique or pedicle technique. In the former, it is harvested from the superior-most level near the internal thoracic vein (ITV) and in the latter, the initial incision is made approximately 100 mm lateral and medial to the artery and it is harvested as a pedicle including the fascia, muscle, connective tissue, and both veins.

The harvest length depends upon the coronary artery to which the anastomosis is to be made. Generally, LITA is used to bypass LAD, ramus intermedius and the diagonal branches and RITA is used to bypass obtuse marginal arteries, PDA and ramus intermedius and with both arteries, usually a maximum length is harvested. The graft connections can be made in single or in sequential manner, depending upon the circumstances and the connections can be made at different angles (for example, parallel, perpendicular, etc.) as appropriate. Both the number of graft connections and the angle identify different types of grafts. ITA is the most common and preferable choice of graft for CABG surgery, owing to its resistance to atherscleros is in $85 - 90\%$ cases for about $7 - 10$ years. An eight year followup for 894 patients who had purely internal thoracic artery grafts showed 86% survival rate at 5 years and 75% survival rate at 8 years [103].

1.2.2 Graft choice: radial artery

Radial artery (RA) is a major artery in human forearm and it is close to the underside of the forearm. This artery is important because it is a superficial artery, that is, the damage is easily repairable and in case of damage, other arteries can take over, thus making it a possible graft choice. Although ITA is the most common arterial bypass conduit choice, it still has limitations such as the length of harvest time and risk of sternal wound infection in patients with diabetes and obesity, etc. In that case, radial artery, which is usually $200 - 250$ mm in the length depending upon stature of the patient, has easy accessibility and does not risk the sternal wound infection. Furthermore, its diameter is $2 - 3$ mm similar to that of coronary arteries. Radial artery is harvested in a pedicle form and through atraumatic no-touch technique, where the first incision is performed in the lateral third of the arm (see figure 1.2.2(b)). This reduces the spasm tendency of the radial artery, owing to its muscular wall.

Radial artery is usually used as a second graft to ITA, in the cases when more arterial grafts are needed. Furthermore, the results have shown that it is safer to use radial artery graft when the occlusion is of severe degree.

1.2.3 Graft choice: saphenuous vein

Saphenuous vein (SV) is the longest superficial vein in the leg. It originates at the bottom of the leg, from the union of dorsal vein the great toe and dorsal venuous network of the foot and travels upwards along the medial side of the lower leg towards the anterior region

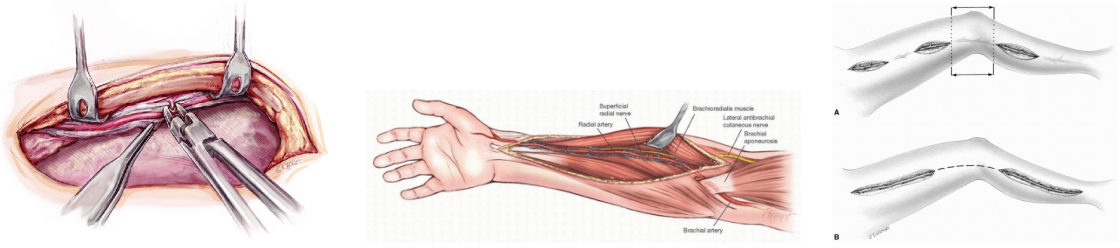

(a). (b). (c).

Figure 1.2.2: (a). Illustration of pedicle harvest of Internal thoracic artery (ITA). (b). Illustration of pedicle harvest of radial artery (RA). (c). Illustration of endoscopic bridge technique harvest of saphenuous vein.

of thigh where it joins the femoral vein. The procedure of extraction is similar to the harvest procedure of the arteries, that is, pedicle technique, where long incision is made on the inner side of the leg and the vein can be divided into multiple segments to perform multiple anastomoses (see figure 1.2.2(c)). Vein grafts have more tendency to fail and therefore, another surgery is needed in most cases, in fact the occulsion rate is more than 50% after 10 years [75]. Despite this, saphenuous vein offers more length and therefore, better access to any coronary artery even multiple arteries, easy access and minimally invasive harvest procedure.

1.3. Motivation and theme of thesis

In this section, we will introduce motivation and objective of this thesis. This thesis is directed at methodological development of numerical methods for patient-specific computational hemodynamics modeling and the corresponding applications in the real-life coronary artery bypass grafts surgery.

Motivation

As discussed in previous sections, the blood flow blockage in the coronary arteries is bypassed through new externally connected vessels, called bypass grafts, through invasive surgical procedures. It has also been discussed that the graft patency relies on a number of factors such as the properties of graft material, compatibility with the coronary artery, harvesting procedure, the medical condition, and the position and angle of anastomoses. With the improved imaging techniques, the medical science has come a long way in terms of diagnosis and treatments, yet the medical images cannot give complete information about the extent of stenosis, its location and restenosis in the surgical devices. Thus, computational hemodynamics modeling combined with medical images plays a vital role in predicting these factors. The hemodynamics behavior can identify the restenosis

in the grafts, the position of occlusion and its extent. Furthermore, the surgeons can use apriori hemodynamics knowledge to decide the angle for anastomosis and type of anastomosis related to increased patency of the surgical device. Patient-specific computational hemodynamics modeling has attained popularity since 1990s. It targets at attaining the blood flow information provided the data of a specific patient, and in the geometries modeling his/her cardiovascular domains. The patient-specific computational hemodynamics modeling require patient-specific geometric models constructed from clinical images, mesh discretization, suitable mathematical model and boundary conditions, and numerical techniques to approximate the blood flow. The two challenges in computational hemodynamics modeling that motivated this work are below:

(i). The critical challenge among the aforementioned factors is the quantification of meaningful boundary conditions and specifically outflow boundary conditions. Many studies have utilized zero pressure or no traction boundary conditions, however using such conditions at the outlets lead to unrealistic results [101]. Use of resistance-impedance based 0D or 1D network models has also gain popularity and such models can accurately predict the boundary conditions [101, 102, 109, 32]. However implementation of such models require manual tuning of certain parameters to achieve results with desired accuracy [96, 95, 89].

(ii). A crucial requirement in patient-specific computational hemodynamics modeling is to take into account many-query scenarios modeled by some parameters, for example, Reynolds number, angle of the graft, inflow velocity. Thus, the numerical simulations need to be repeated for different parameter values. The geometries in cardiovascular problems often comprise of large discretization size even when the geometries are truncated to only main vessels of interest. The repeated simulations with fine mesh size are usually computationally very demanding and mostly unbearable.

Theme

The theme of this thesis is construction and implementation of numerical techniques that address the aforementioned challenges, with the aim to model patient-specific physiological data through computational hemodynamics as best as possible [113, 100].

In this thesis, first we will focus on combining optimal flow control problems with computational hemodynamics modeling to minimize the misfit between patient-specific physiological measurements, for example the flow rates or blood flow velocity measured from 4D-flow MRIs, or in other words, to match the patient-specific data with computational hemodynamics in many-query parametrized settings. In such problems, the outflow boundary conditions in our focus will be the ones required to match the desired data. To address the first challenge, the control in this optimal flow control problems will be an additional unknown variable implemented through the outflow boundary conditions and hence, the optimal flow control framework shall yield automated quantification of unknown

boundary conditions. We will particularly focus on putting this mathematical problem in a coupled monolithic-structured system.

Then, our center of attention will be construction of a numerical framework based upon commonly implemented full-order numerical methods to approximate the parametrized optimal flow control problems in a reliable and time-efficient manner while keeping the coupled structural properties [100]. This will address the second challenge. Furthermore, this thesis will illustrate the applications of the complete numerical framework in patient-specific geometric models of coronary artery bypass grafts, constructed through an algorithm that will be briefly discussed in the next sections [113] .

1.4. Literature review

In this section, we will review some earlier and recent efforts made separately in computational hemodynamics modeling, optimal flow control problems and reduced order modeling and the efforts made in combining the optimal flow control framework and model order reduction with real-life applications.

- *From computational hemodynamics modeling to patient-specific computational hemodynamics modeling.*

  In 1999, Bertolotti and Deplano [24] performed 3D hemodynamics simulations in an idealized geometry for a coronary artery bypass graft, with two cases of host artery with and without 75% stenosis. They studied the relation between jet flow from host artery and supplying flow from the graft and the effects on development of hyperplasia. Furthermore, the numerical simulations are performed using finite element methods. In 2001, they extended this work to unsteady flows [37]. In 2002, Bonert et al. [28] studied the hemodynamics in 3D idealized geometrical models for different configurations, that are parallel side-to-side, diamond side-to-side, and end-to- side and concluded that the parallel configuration was better for graft patency, the diamond configuration was better for host artery patency. They implemented finite element methods at the numerical level and further suggested the large graft-to-host diameter ratio to be hemodynamically better than small ratio. Furthermore, in the same year Ku et al. [64] matched the in-vivo blood flow measurements through numerical predictions in real-life surgery-based geometrical models of aorta-bypass grafts in pigs. They utilized pulsatile Womersley profile at the inlets and zero pressure outflow conditions and their results matched the in-vivo MRI measurements with an average difference of 6% in the aorta-to-inlet blood flow ratio.

  In 2004, Boutsianis et al. [29] reconstructed real-life coronary arteries of the pigs, from a CT-scan to study the feasibility of intracoronary coronary flow. They used finite volume methods for the numerical simulations and reported the *computational cost to increase exponentially with the increase in number of mesh elements.* In 2006,

Cacho et al. [31] studied the effects of different incision lengths and corresponding insertion angles for a given graft diameter for the coronary artery and bypass graft from same patient. They used finite elment methods for computational hemodynamics modeling and concluded smaller insertion angles to be hemodynamically beneficial and large incision lengths for the small insertion angles. In $2007-08$ Politis et al. [85, 86] performed comparitive study for idealized geometries of different types of grafts including T-graft, Y-graft, Π-graft and sequential graft using finite element methods. They prescribed a *known inlet velocity* and *uniform outlet pressure* conditions.

In 2006, Clementel et al. [109] studied the *outflow boundary conditions* for 3D real-patient geometric models of coronary arteries through finite element methods. They implemented 1D lumped parameter network at the inlets and outlets and suggested inadequate outflow conditions to be most critical hurdle for accurate pressure approximations. They extended this work in 2010 to study the outflow conditions through the lumped models for non-periodic blood flow in real-life geometries of coronary arteries [32]. Recently Sankaran et al. [96, 95] have modeled patient-specific hemodynamics in patient-specific coronary artery bypass grafts and have implemented resistance-impedance based models at the boundary where they have choosen some parameters randomly (for example, β). Furthermore, Romarowski et al. [89] have implemented a three-element lumped network model approach to model patient-specific hemodynamics in thoracic aorta.

- *From theory of optimal flow control problems to reduced order parametrized optimal flow control problems and applications.*

  Owing to vastness of the topics like optimal flow control problems and reduced order methods, here rather than doing a time-line journey of the work done in these areas, we will try to give a general overview of different efforts made in the methodological aspects of these subjects and in connecting them together, and also with computational hemodynamics modeling.

  The theory of optimal flow control problems was introduced by *Jacques-Louis Lions* [70, 71, 72] during 1960s and 1970s. Lagrange multiplier approach to cast constrained problems into unconstrained ones is presented and utilized in [46, 52, 108, 54, 87, 47]. The optimal flow control problems have been combined with numerical methods such as finite element, least-square and finite volume methods along with applications in by Bochev and Gunzburger [46, 26, 27], Hinze et al. [52] and Rozza [87]. Some recent applications using full-order numerical methods such as finite element methods have been shown in [112, 6].

  The reduced order methods are implemented to approximate parametrized problems in a time-efficient and reliable manner. For details of these methods, we refer the reader to [49, 87]. Rozza et al. [90, 91, 93, 3, 4] developed and implemented the

reduced order framework for shape optimization and optimal control in idealized geometries for aorto-coronary and coronary artery bypass grafts. Furthermore, these methods were implemented by Lassila et al. [66] in inverse hemodynamics problems in idealized geometries. The work by Rozza et al. [90, 91, 93, 3, 4] was recently extended by Ballarin et al. [17, 18] for shape optimization of patient-specific coronary artery bypass grafts and fast hemodynamics simulations in patient-specific geometrical models of coronary artery bypass grafts. Furthermore, in the direction of stabilization of these methods, Veroy and Rozza presented reduced order methods with supremizers stabilization for Stokes equations in [94] and Ballarin et al. extended this work for Navier-Stokes equations in [19]. Recently Ali et al. [9, 8, 51] adopted different stabilization strategies, for these methods, based upon adding stabilization term(s) in the problem formulation.

The optimal flow control problems were combined with the reduced order methods in the early 2000s by Ito, Ravindran and Hou [55, 57, 56, 53]. In 2008, Kunisch et al. presented proper orthogonal decomposition (POD) based reduced order technique for optimal control problems in [65]. In 2007 and 2012, Dedé et al. [34, 35] implemented the reduced order framework for the drag minimization problem and presented some error estimators for the reduced order parametrized optimal control problems with control constraints. Recently, Kärcher [60] implemented these techniques in parametrized distributed control problems constrained by elliptic equations. In $2013 - 2015$, Negri et al. [88, 82, 81] formulated the saddle-point framework for reduced parametrized optimal flow control problems constrained by elliptic equations and Stokes equations. They applied the framework to simple 2D and 3D problems with idealized geometries. Recently, this framework has been applied to control gulf pollution by Strazzullo et al. [99].

1.5. From clinical image to patient-specific coronary artery bypass graft geometries

Here we will rehash the approach employed and discussed by Ballarin et al.[17, 18] to reconstruct cardiovascular anatomical surfaces from clinical images. The algorithm used in this work is similar, makes use of open-source 3-dimensional modeling libraries *Visualization Toolkit* (VTK)[97] and *Vascular Modeling Toolkit* (VMTK) [12], and is implemented using Python. Moreover, we will discuss the algorithm with respect to its application to clinical data received from *Sunnybrook Health Sciences Centre, Toronto, Canada.*

The received medical data is a post-surgery computed tomography (CT) scan from a coronary artery bypass surgery performed on a patient with triple vessel coronary disease. Thus, three different graft connections are made, that is, right internal mammary artery (RIMA) is grafted to bypass the blockage in left anterior descending artery (LAD) and two different connections, using saphenuous vein (SV), are made to first obtuse marginal artery (OM1) and posterior descending artery (PDA). Diseased coronary arteries and cor-

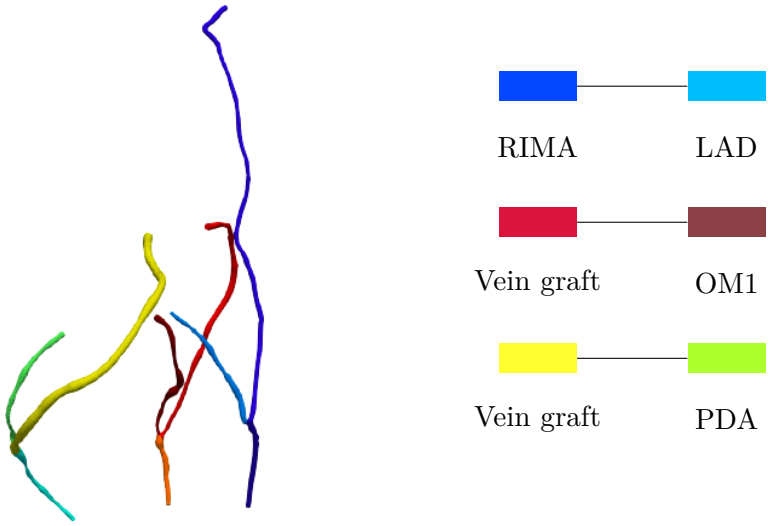

Figure 1.5.1: Clinical case: triple coronary arteries bypass graft surgery

responding grafts, marked with different colors, are shown in figure 1.5.1.

We pre-process the obtained medical image in order to augment image segmentation and geometrical reconstruction process. The pre-processing step is done at three stages, that are resampling, smoothing and enhancement. The resampling stage aims at matching the resolution of the acquired image with the desired image segmentation process. Then, anisotropic diffusion filtering is used to smooth out the image areas with high-frequency noise and finally vessel enhancement filters are applied to enhance the visibility of vessel-shaped structures in comparison to other anatomical structures. For more details, we refer the reader to Antiga et al.[11]. Afterwards, using VMTK we segment the pre-processed image into level sets, based on colliding fronts approach. 3D polygonal surface is then generated through marching cube algorithm and is constructed by placing seed points in user-defined thresholds according to visible intensity of the vessels. Depending upon narrow range of the thresholds and noise in clinical image, the reconstruction process can add such artifacts to the reconstructed geometry, that are not a part of the original vessel. We use VMTK smoothing filters that remove deformities to much extent, however the smoothness of the resulting tubular structures is not sufficient to make them viable as a computational domain.

Our goal is to generate sufficiently smooth surfaces preserving same anatomical structures as reconstructed surfaces. For this purpose, we first extract centerlines, that is the lines between two sections of lumen such that their minimal distance from the boundary is maximal[12, 84, 18]. The extracted centerlines have a maximum inscribed sphere radius value associated to each point on them. The centerlines are, then, averagely smoothened and based on the maximum inscribed sphere radii values, polyballs are inserted around the

Modeling and programming libraries utilized in this work	
VTK	`www.vtk.org`
VMTK	`www.vmtk.org`
TetGen	`www.wias-berlin.de/software/tetgen`
ParaView	`www.paraview.org`
FEniCS	`www.fenicsproject.org`
RBniCS	`mathlab.sissa.it/rbnics`
multiphenics	`mathlab.sissa.it/multiphenics`

centerlines to yield a smooth 3D volume preserving patient-specific anatomical configuration.

The algorithm is summarized in figure 1.5.2. Finally, for computational purposes we generate tetrahedral mesh inside the reconstructed volumes and triangular mesh over the boundaries, using TetGen. To exploit Python based finite element libraries, for example, Dolfin, FEniCS and multiphenics [74, 73, 10, 1], we write the mesh in relative readable formats using VTK.

1.6. Organization of thesis

This thesis comprises of 5 chapters, organized in the following manner:

Chapter 1: Introduction and Motivation.

The first chapter is divided into two main parts, where the first part comprises of anatomical introduction of the coronary arteries, coronary artery disease, bypass graft surgery and corresponding choices. At the end of this part we have introduced the motivation and theme of this thesis which will consist of both methodological development and real-life applications. Then, we have presented some literature review for the patient-specific hemodynamics modeling and reduced order optimal flow control problems with cardiovascular applications such as shape optimization and inverse hemodynamics flow. In the second part of this chapter, we have done a brief overview of the construction of patient-specific geometric models from a CT-scan of real-life triple coronary artery bypass surgery, provided to us by Sunnybrook Health Sciences Centre, Toronto, Canada. At the end of this chapter, we will give some literature review.

Chapter 2: PDEs-constrained optimal flow control problems and numerical approximations.

In the second chapter we will first introduce the optimal flow control problems in a

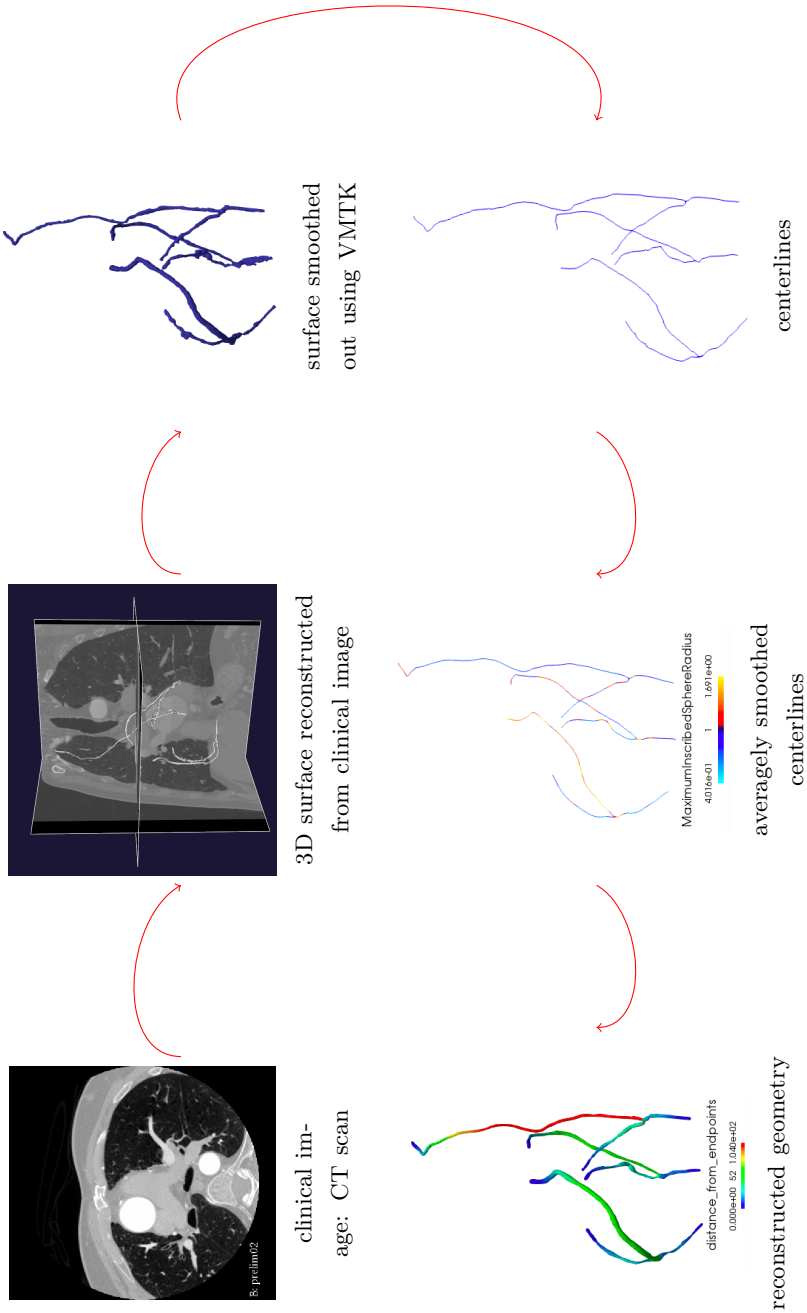

Figure 1.5.2: Algorithm applied for geometrical reconstruction from medical images

general paradigm when the state of fluid flow is modeled by partial differential equations (PDEs) and the objective functional considered is quadratic. We will review the first order sufficient optimality conditions and the derivation of coupled Karush-Kuhn-Tucker (KKT) optimality system in a Lagrangian framework. Afterwards, we will concentrate on the optimal flow control problems with control implemented at *boundaries* and state modeled specifically by Stokes equations and Navier-Stokes equations. We will show the saddle-point formulation of the problem in both cases and further, we will numerically approximate these problems using Galerkin finite element methods. We will also review some basic conditions needed to be fulfilled in order to ensure the existence of a unique stable solution at the continuous and the discrete level. At the end of this chapter, we will illustrate the applications of the numerical optimal flow control framework to patient-specific coronary arteries and will show the quantification of unknown boundary conditions at the outlets, required to match the desired physiological data.

Chapter 3: Reduced order methods for parametrized optimal flow control problems.

In the third chapter, we will consider the extension of the numerical framework discussed in chapter 2 to parametrized optimal flow control problems. The chapter will begin with the introduction of Stokes-constrained optimal flow control framework in parametrized settings. Then we will show construction of a reduced order framework for these problems, based upon proper orthogonal decomposition (POD)–Galerkin approach and we will show that this framework preserves the algebraic structure of the continuous and discrete problems and while slightly increasing the dimensions, we can satisfy the requirements for existence of a unique stable solution at the reduced order level. Furthermore, we will show the phase decoupling of computational procedure in the reduced order framework based upon the assumption of affine decomposition.

Afterwards, we will extend the reduced order framework to non-linear quadratic optimal flow control problems that are constrained by Navier-Stokes equations. The focus will be to retain the algebraic structure, the stability properties and the phase decoupling, which can be challenging owing to non-linearity of the terms. We will show implementation of iterative numerical schemes in such cases and further, we will illustrate the application of both cases to idealized geometries that can be considered close to a Y-graft.

Chapter 4: Applications of reduced order parametrized optimal flow control problems to patient-specific coronary artery bypass grafts.

In the fourth chapter, we will apply the reduced order framework constructed in chapter 3 to the patient-specific coronary artery bypass grafts. We will compare the computational performances with respect to the patient-specific applications shown in chapter 2 in which numerical solution is attained through high order methods. Furthermore, the results will be shown for two cases, first when we will consider a geometry comprising of single graft

and coronary artery and second when we will consider a geometry comprising of two grafts and corresponding coronary arteries, not connected with each other but considered as a single computational domain. In such case, the unknown control will account for the outflow boundary conditions required at the two outlets altogether to match the desired data, provided different inflow velocities at the corresponding inlets.

Chapter 5: Concluding remarks & future perspectives.

In the fifth chapter, we will provide some concluding remarks and some future perspectives with possible extensions of this work. We would like to bring the reader's attention towards the main assumptions kept in this thesis, that are, rigid and fixed geometries, use of unknown control to quantify simple Neumann boundary conditions and arbitrary desired velocity matched through Stokes and Navier-Stokes velocities. With this work, we have shown the construction of a reduced order framework and through its applications to real-life cardiovascular problems, we have shown the reliability and time-efficiency of the framework, however for the aforementioned restrictions. Future directions can include extension of the framework to surpass the restrictions kept in this work, thus, *fluid-structure interaction* problems, unknown control implementation in surrogate boundary conditions models and implementation of 4D patient-specific physiological data are a few of many possible extensions.

Chapter 2

PDEs-constrained optimal flow control problems and numerical approximations

***

In this chapter, we will introduce general formulation of optimal flow control problems constrained by partial differential equations (PDEs) and numerical techniques employed for solving such problems in finite dimensional settings. We will further introduce data assimilation in cardiovascular problems through the optimal flow control regime and will demonstrate its application to patient-specific cardiovascular configurations, with the goal to minimize misfit between clinical data and solution attained through a numerical simulation.

The optimal flow control problems structurally comprise of state modeling equations, a defined objective functional and unknown control quantities affecting fluid flow. Solving such problems, we aim at finding an optimal pair of state and control variables that minimize the objective functional. Thanks to their structure, these problems are being applied to control several phenomena in fluid dynamics. Some examples include recent applications in wind turbines to mitigate power losses caused by turbine wake [112], in thermal sterilization process to control temperature, in marine applications to control parameters responsible for quality of aquatic life and to control gulf pollution [99] and in acoustical applications to control noise [23], etc.

In the last few decades, implementation of the optimal flow control framework has flourished in computational biomedical sciences. Some recent efforts in this direction aim at addressing one of the critical challenges faced in computational hemodynamics modeling, that is quantification of boundary conditions. It is well-known that accuracy of boundary conditions is vital to realistic hemodynamics modeling. In literature, multiscale models such as lumped network models and distributed network models are being used for the purpose [32, 96, 95]. However, when the focus is on computational fluid dynamics or fluid-structure interaction or the exact boundary conditions are known, simpler expressions such as Dirichlet and Neumann conditions are being utilized at the boundaries.

Romarowski et al. [89] have utilized the optimal control framework to quantify parameters for these models imposing outflow boundary conditions for human aorta. Their approach is a pioneer attempt in this direction along with assimilation of the boundary conditions with phase contrast MRI measurements, however, it faces the limitations of high computational cost and lack of patient-specific phyiological data assimilation. Tiago et al. [106] have made a similar attempt by approximating Dirichlet inflow conditions through the optimal flow control problems with focus on data assimilation, that is, matching known data with the fluid flow variables. They have utilized realistic geometries for cerebral aneurysms and the authors claim to have a major drawback of high computational cost. Furthermore, Koltukluoğlu et al. [63] have extended the approach implemented in [106] to data assimilation in glass replica of human aorta. They have used artificially generated data to validate the approach in simplified geometry and denoised 4D-flow MRIs data in the glass replica of human aorta. However, their approach has not been extended to patient-specific biomedical problems and requires large computational effort.

In this chapter, we will discuss the problem formulation and solution strategies for such problems with the aim to address the above mentioned issue for coronary artery bypass

graft surgery. Our focus will be on quantification of outflow conditions through pressure control (Neumann conditions), required to match presumably known patient-specific clinical data in patient-specific cardiovascular configurations. This chapter is arranged in the following order: in the first and the second sections, we will discuss continuous formulation of optimal flow control problems and derivative based optimization strategies, respectively. In the third section, we will discuss the optimality condition and afterwards, we will cast the problem in a monolithic-structured coupled optimality system through saddle-point formulation and first order sufficient optimality conditions. The discussion will be extended to optimal flow control problems with the state modeled by Stokes and Navier-Stokes equations. We will also show some preliminary numerical tests for both cases and in the last section, we will extend the applications to cardiovascular geometries. We remark that in this work we have used both FEniCS [73, 10] and multiphenics [1], an internally developed Python-based library for easy-prototyping of multiphysics problems in FEniCS, for numerical approximation of the optimal flow control problems through Galerkin finite element methods. We further remark that the numerical tests to be discussed in this chapter, were carried out in multiphenics [1].

2.1. Optimal flow control problems

Let us denote state variables modeling the physical characteristics of fluid flow, such as velocity and pressure by $\boldsymbol{s}$ and unknown control variables governing behavior of fluid flow by $\boldsymbol{u}$. Furthermore, let us consider Hilbert spaces S and U such that $\boldsymbol{s} \in S$ and $\boldsymbol{u} \in U$ and an observation space $Q \supseteq S$. In this work, we will consider minimization of a quadratic objective functional $\mathcal{J} : Q \times U \to \mathbb{R}$ subject to linear/non-linear state governing equations. We will use superscript asterisk $(^*)$ to denote dual space and the residual of the state equations will be given by $\mathcal{F} : S \times U \to S^*$. Then, the textbook definition of an optimal flow control problem [71, 52, 46, 108, 87] reads:

Problem 2.1. *Find optimal pair $(\boldsymbol{s}, \boldsymbol{u}) \in S_{ad} \times U_{ad}$ such that*

$$\min_{(\boldsymbol{s},\boldsymbol{u})\in S\times U} \mathcal{J}(\boldsymbol{s},\boldsymbol{u}) \;\; \textit{subject to } \mathcal{F}(\boldsymbol{s},\boldsymbol{u}) = 0, \qquad \boldsymbol{s} \in S_{ad}, \boldsymbol{u} \in U_{ad}, \tag{2.1}$$

where $S_{ad} \subseteq S$ and $U_{ad} \subseteq U$ are the spaces for admissible solutions.

Existence and uniquess of solution to this problem is established by the following theorem given by Hinze et al. [52](section 1.5.2, theorem 1.45):

Theorem 2.1. *A unique solution $(\boldsymbol{s}, \boldsymbol{u}) \in S \times U$ to problem 2.1 will exist if the following assumptions hold true:*

i. $S_{ad} \subseteq S$ and $U_{ad} \subseteq U$ are convex and closed,

ii. $\mathcal{G} \neq \emptyset$, where $\mathcal{G} = \{(\boldsymbol{s}, \boldsymbol{u}) \in S \times U \mid \mathcal{F}(\boldsymbol{s}, \boldsymbol{u}) = 0\}$ is the feasible set,

iii. State governing equations are continuous and well-posed, that is, for every $u \in U$, $\mathcal{F}(\boldsymbol{s}, \boldsymbol{u})$ admits a unique corresponding solution $\boldsymbol{s}(\boldsymbol{u})$,

iv. For any sequence $\{(\boldsymbol{s}, \boldsymbol{u})_i\}_{i \in \mathbb{N}} \in S \times U \rightharpoonup (\boldsymbol{s}, \boldsymbol{u}) \in S \times U$, the objective functional satisfies $\mathcal{J}(\boldsymbol{s}, \boldsymbol{u}) \leq \lim_{i \to \infty} \inf \mathcal{J}((\boldsymbol{s}, \boldsymbol{u})_i)$.

We consider the optimization problem unconstrained with respect to state and control variables, that is, $S_{ad} \equiv S$ and $U_{ad} \equiv U$ and $\mathcal{F}(\boldsymbol{s}, \boldsymbol{u})$ to be the residual of Stokes or Navier-Stokes equations, respectively. Now, we introduce the Lagrangian formulation of problem 2.1, to cast the problem constrained by state equations into an unconstrained problem by imposing the state constraints through Lagrange multipliers. Thus, equation 2.1 can be re-written in a composite Lagrange function $\mathcal{L} : S \times U \times S^{**} \to \mathbb{R}$, defined as:

$$\mathcal{L}(\boldsymbol{s}, \boldsymbol{u}, \boldsymbol{z}) = \mathcal{J}(\boldsymbol{s}, \boldsymbol{u}) + \langle \mathcal{F}(\boldsymbol{s}, \boldsymbol{u}), \boldsymbol{z} \rangle, \tag{2.2}$$

where $\boldsymbol{z} \in S^{**}$ is the Lagrange multiplier. Furthermore, let us rename S^{**} as Z and owing to reflexivity of Hilbert spaces we remark that $Z \equiv S$. Since the Lagrangian formulation casts the constrained problem into an unconstrained one by introducing additional variables, that are the Lagrange multipliers, the dimensions of the problem increase, however rendering it into an easier one as compared to the original constrained problem. Thus, problem 2.1 can now be re-directed as to solve the Lagrangian (2.2) for critical points $(\boldsymbol{s}, \boldsymbol{u}, \boldsymbol{z})$.

2.2. Derivative-based optimization

In this work, we will focus on derivative-based optimization techniques and make the following assumptions:

(*i*). $\mathcal{J} : S \times U \to \mathbb{R}$ and $\mathcal{F} : S \times U \to S^*$ are twice continuously Frèchet differentiable.

(*ii*). $\mathcal{F} : S \times U \to S^*$ has bounded inverse.

(*iii*). The derivative of state equations with respect to state variables, that is $\mathcal{F}_{\boldsymbol{s}}(\boldsymbol{s}(\boldsymbol{u}), \boldsymbol{u})$, is invertible.

We re-write the problem 2.1 with reduced objective functional $\tilde{\mathcal{J}}(\boldsymbol{u}) := \mathcal{J}(\boldsymbol{s}(\boldsymbol{u}), \boldsymbol{u})$ as:

Problem 2.2.

$$\min_{\boldsymbol{u} \in \tilde{U}} \tilde{\mathcal{J}}(\boldsymbol{u})$$

such that

$$\boldsymbol{u} \in \tilde{U} = \{\boldsymbol{u} \in U \mid \mathcal{F}(\boldsymbol{s}(\boldsymbol{u}), \boldsymbol{u}) = 0,\ (\boldsymbol{s}(\boldsymbol{u}), \boldsymbol{u}) \in S \times U\}.$$

Differentiating the objective functional, we get,

$$\left\langle \tilde{\mathcal{J}}'(\boldsymbol{u}), \boldsymbol{v} \right\rangle = \langle \mathcal{J}_{\boldsymbol{s}}(\boldsymbol{s}(\boldsymbol{u}), \boldsymbol{u}), \boldsymbol{s}'(\boldsymbol{u})\boldsymbol{v} \rangle + \langle \mathcal{J}_{\boldsymbol{u}}(\boldsymbol{s}(\boldsymbol{u}), \boldsymbol{u}), \boldsymbol{v} \rangle \tag{2.3}$$

The derivative of state variables with respect to control appearing in equation (2.3) is *sensitivity*, that is to be calculated whenever complete derivative of reduced objective functional is required. In literature, two approaches [52, 46, 26, **?**] can be implemented to deal with it, namely, sensitivity analysis and adjoint approach. We give an overview of these approaches below:

2.2.1 Sensitivity analysis

The simpler method of calculating sensitivity $\boldsymbol{s}'(\boldsymbol{u})\,\boldsymbol{v}$ is through the state constraints. Differentiating $\mathcal{F}(\boldsymbol{s}(\boldsymbol{u}),\boldsymbol{u})=0$ yields:

$$\mathcal{F}_{\boldsymbol{s}}(\boldsymbol{s}(\boldsymbol{u}),\boldsymbol{u})\,\boldsymbol{s}'(\boldsymbol{u})\,\boldsymbol{v}+\mathcal{F}_{\boldsymbol{u}}(\boldsymbol{s}(\boldsymbol{u}),\boldsymbol{u})\,\boldsymbol{v}=0. \tag{2.4}$$

$\Rightarrow$

$$\mathcal{F}_{\boldsymbol{s}}(\boldsymbol{s}(\boldsymbol{u}),\boldsymbol{u})\,\boldsymbol{s}'(\boldsymbol{u})\,\boldsymbol{v}=-\mathcal{F}_{\boldsymbol{u}}(\boldsymbol{s}(\boldsymbol{u}),\boldsymbol{u})\,\boldsymbol{v}. \tag{2.5}$$

Thus, $\boldsymbol{s}'(\boldsymbol{u})\,\boldsymbol{v}$ can be obtained by solving equation (2.5) and the derivative of the reduced objective functional can then calculated through equation (2.3). This approach requires to compute the complete sensitivity operator $\boldsymbol{s}'(\boldsymbol{u})$ in all directions $\boldsymbol{v}\in U_B$, where U_B is a basis for U. Therefore, in this approach, the computational effort will increase with respect to dimensions of U.

2.2.2 Adjoint approach

An alternative approach to deal with sensitivity operator is to re-formulate equation (2.3), such that $\tilde{J}'(\boldsymbol{s}(\boldsymbol{u}),\boldsymbol{u})$ is calculated through so-called *adjoint equation*. We re-write equation (2.3) as:

$$\left\langle \tilde{\mathcal{J}}'(\boldsymbol{u}),\boldsymbol{v}\right\rangle=\left\langle\left\{\boldsymbol{s}'(\boldsymbol{u})^{*}\,\mathcal{J}_{\boldsymbol{s}}(\boldsymbol{s}(\boldsymbol{u}),\boldsymbol{u})+\mathcal{J}_{\boldsymbol{u}}(\boldsymbol{s}(\boldsymbol{u}),\boldsymbol{u})\right\},\boldsymbol{v}\right\rangle$$

or equivalently,

$$\tilde{\mathcal{J}}'(\boldsymbol{u})=\boldsymbol{s}'(\boldsymbol{u})^{*}\,\mathcal{J}_{\boldsymbol{s}}(\boldsymbol{s}(\boldsymbol{u}),\boldsymbol{u})+\mathcal{J}_{\boldsymbol{u}}(\boldsymbol{s}(\boldsymbol{u}),\boldsymbol{u}) \tag{2.6}$$

Evidently, the only unknown required in equation (2.6) is $\boldsymbol{s}'(\boldsymbol{u})^{*}\,\mathcal{J}_{\boldsymbol{s}}(\boldsymbol{s}(\boldsymbol{u}),\boldsymbol{u})$ which can be calculated through differentiation of the state equation. Thus, from equation (2.4), we can write $\boldsymbol{s}'(\boldsymbol{u})=-\mathcal{F}_{\boldsymbol{s}}(\boldsymbol{s}(\boldsymbol{u}),\boldsymbol{u})^{-1}\,\mathcal{F}_{\boldsymbol{u}}(\boldsymbol{s}(\boldsymbol{u}),\boldsymbol{u})$.

$\Rightarrow$

$$\boldsymbol{s}'(\boldsymbol{u})^{*}\,\mathcal{J}_{\boldsymbol{s}}(\boldsymbol{s}(\boldsymbol{u}),\boldsymbol{u})=-\mathcal{F}_{\boldsymbol{u}}(\boldsymbol{s}(\boldsymbol{u}),\boldsymbol{u})^{*}\,\mathcal{F}_{\boldsymbol{s}}(\boldsymbol{s}(\boldsymbol{u}),\boldsymbol{u})^{-*}\,\mathcal{J}_{\boldsymbol{s}}(\boldsymbol{s}(\boldsymbol{u}),\boldsymbol{u}), \tag{2.7}$$

where superscript $(^{*})$ denotes dual operator. Now we consider $\boldsymbol{z}=\boldsymbol{z}(\boldsymbol{u})$ to be solution of the following equation, also known as adjoint equation:

$$\left\langle \mathcal{J}_{\boldsymbol{s}}(\boldsymbol{s}(\boldsymbol{u}),\boldsymbol{u}),\boldsymbol{s}'(\boldsymbol{u})\,\boldsymbol{v}\right\rangle+\left\langle \mathcal{F}_{\boldsymbol{s}}(\boldsymbol{s}(\boldsymbol{u}),\boldsymbol{u}),\boldsymbol{s}'(\boldsymbol{u})\,\boldsymbol{v}\boldsymbol{z}\right\rangle=0, \tag{2.8}$$

then, $\boldsymbol{z} = \boldsymbol{z}(\boldsymbol{u}) := -\mathcal{F}_{\boldsymbol{s}}(\boldsymbol{s}(\boldsymbol{u}), \boldsymbol{u})^{-*} \mathcal{J}_{\boldsymbol{s}}(\boldsymbol{s}(\boldsymbol{u}), \boldsymbol{u})$. Thus, equation (2.7) can be re-formulated as:

$$\boldsymbol{s}'(\boldsymbol{u})^{*} \mathcal{J}_{\boldsymbol{s}}(\boldsymbol{s}(\boldsymbol{u}), \boldsymbol{u}) = \mathcal{F}_{\boldsymbol{u}}(\boldsymbol{s}(\boldsymbol{u}), \boldsymbol{u})^{*} \boldsymbol{z}(\boldsymbol{u}), \tag{2.9}$$

From an algorithmic point of view, one first needs to solve adjoint equation (2.8) for the Lagrange multipliers $\boldsymbol{z}(\boldsymbol{u})$, which are also known as adjoint variables now. Then, $\boldsymbol{s}'(\boldsymbol{u})^{*} \mathcal{J}_{\boldsymbol{s}}(\boldsymbol{s}(\boldsymbol{u}), \boldsymbol{u})$ can be calculated through equation (2.9) and finally, (2.6) can be utilized to calculate $\tilde{\mathcal{J}}'(\boldsymbol{u})$. Through this approach, the operator $\boldsymbol{s}'(\boldsymbol{u})$ is not needed to be calculated explicitly, thus computational cost is lower.

2.3. Optimality equation and Karush-Kuhn-Tucker optimality system

In this section, we will introduce the optimality equation, satisfied by the optimal solution to problem 2.2. We will derive the optimality equation in Lagrangian framework and further cast the optimal flow control problem in a coupled optimality system residing upon state, adjoint and optimality equations.

2.3.1 Optimality equation

The optimality condition for problem 2.2 is given by the following theorem:

Theorem 2.2. *Assume $\tilde{\mathcal{J}}$ to be convex, then, a local minimum $\tilde{\boldsymbol{u}} \in \tilde{U}$ to problem 2.2 will exist iff the variational form of minimum principle or optimality condition is satisfied, that is,*

$$\left\langle \tilde{\mathcal{J}}'(\tilde{\boldsymbol{u}}), \boldsymbol{v} - \tilde{\boldsymbol{u}} \right\rangle \geq 0, \ \forall \ \boldsymbol{v} \in \tilde{U}. \tag{2.10}$$

For proof of the theorem 2.2, we refer the reader to [52]. Furthermore, the local minimum $\boldsymbol{u} \in U$ will also be global minimum if the objective functional $\mathcal{J}$ is convex. It is to be noted that the inequality constraint in optimality equation (2.10) is replaced with equality constraint if $\tilde{U} \equiv U$. Now, to derive the optimality constraint for the Lagrangian (2.2), let us re-write the Lagrangian as:

$$\mathcal{L}(\boldsymbol{s}(\boldsymbol{u}), \boldsymbol{u}, \boldsymbol{z}) = \tilde{\mathcal{J}}(\boldsymbol{u}) + \langle \mathcal{F}(\boldsymbol{s}(\boldsymbol{u}), \boldsymbol{u}), \boldsymbol{z} \rangle. \tag{2.11}$$

We suppose that a local minimum $\boldsymbol{u} \in U$ exists for this Lagrangian. Differentiation of the Lagrangian 2.11 yields:

$$\begin{aligned} \langle \mathcal{L}'(\boldsymbol{s}(\boldsymbol{u}), \boldsymbol{u}, \boldsymbol{z}), \boldsymbol{v} \rangle &= \langle \mathcal{L}_{\boldsymbol{s}}(\boldsymbol{s}(\boldsymbol{u}), \boldsymbol{u}, \boldsymbol{z}), \boldsymbol{s}'(\boldsymbol{u}) \boldsymbol{v} \rangle + \langle \mathcal{L}_{\boldsymbol{u}}(\boldsymbol{s}(\boldsymbol{u}), \boldsymbol{u}, \boldsymbol{z}), \boldsymbol{v} \rangle \\ &= \left\langle \tilde{\mathcal{J}}'(\boldsymbol{u}), \boldsymbol{v} \right\rangle + \langle \mathcal{F}'(\boldsymbol{s}(\boldsymbol{u}), \boldsymbol{u}), \boldsymbol{v}\boldsymbol{z} \rangle, \end{aligned}$$

where

$\left\langle \tilde{\mathcal{J}}'(\boldsymbol{u}), \boldsymbol{v} \right\rangle = \langle \mathcal{J}_{\boldsymbol{s}}(\boldsymbol{s}(\boldsymbol{u}), \boldsymbol{u}), \boldsymbol{s}'(\boldsymbol{u}) \boldsymbol{v} \rangle + \langle \mathcal{J}_{\boldsymbol{u}}(\boldsymbol{s}(\boldsymbol{u}), \boldsymbol{u}), \boldsymbol{v} \rangle$ and

$$\langle \mathcal{F}'(\boldsymbol{s}(\boldsymbol{u}),\boldsymbol{u}),\boldsymbol{vz}\rangle = \langle \mathcal{F}_{\boldsymbol{s}}(\boldsymbol{s}(\boldsymbol{u}),\boldsymbol{u}),\boldsymbol{s}'(\boldsymbol{u})\boldsymbol{vz}\rangle + \langle \mathcal{F}_{\boldsymbol{u}}(\boldsymbol{s}(\boldsymbol{u}),\boldsymbol{u}),\boldsymbol{vz}\rangle .$$

Now, we consider $\boldsymbol{z} = \boldsymbol{z}(\boldsymbol{u})$ to be solution of the following equation:

$$\langle \mathcal{L}_{\boldsymbol{s}}(\boldsymbol{s}(\boldsymbol{u}),\boldsymbol{u},\boldsymbol{z}),\boldsymbol{s}'(\boldsymbol{u})\boldsymbol{v}\rangle = 0, \tag{2.12}$$

which is essentially equivalent to the adjoint equation (2.8). Then,

$$\left\langle \tilde{J}'(\boldsymbol{u}),\boldsymbol{v}\right\rangle = \langle \mathcal{L}_{\boldsymbol{u}}(\boldsymbol{s}(\boldsymbol{u}),\boldsymbol{u},\boldsymbol{z}),\boldsymbol{v}\rangle = \langle \mathcal{J}_{\boldsymbol{u}}(\boldsymbol{s}(\boldsymbol{u}),\boldsymbol{u}) + \mathcal{F}_{\boldsymbol{u}}(\boldsymbol{s}(\boldsymbol{u}),\boldsymbol{u})^{*}\boldsymbol{z},\boldsymbol{v}\rangle .$$

Thus, theorem 2.2 can be re-stated in terms of Lagrangian as:

Theorem 2.3. *If a local minimum $\tilde{\boldsymbol{u}} \in \tilde{U}$ exists for problem 2.2, then, it satisfies the following optimality equation:*

$$\langle \mathcal{L}_{\tilde{\boldsymbol{u}}}(\boldsymbol{s},\tilde{\boldsymbol{u}},\boldsymbol{z}),\boldsymbol{v}-\tilde{\boldsymbol{u}}\rangle \geq 0,\ \forall\ \boldsymbol{v}\in\tilde{U}, \tag{2.13}$$

or equivalently,

$$\langle \mathcal{J}_{\tilde{\boldsymbol{u}}}(\boldsymbol{s},\tilde{\boldsymbol{u}}) + \mathcal{F}_{\tilde{\boldsymbol{u}}}(\boldsymbol{s},\tilde{\boldsymbol{u}})^{*}\boldsymbol{z},\boldsymbol{v}-\tilde{\boldsymbol{u}}\rangle \geq 0,\ \forall\ \boldsymbol{v}\in\tilde{U}. \tag{2.14}$$

Here, we reiterate that the inequality in optimality conditions (2.13) and (2.14) is replaced by equality if $\tilde{U} \equiv U$.

2.3.2 Karush-Kuhn-Tucker optimality system

Next, we cast the optimal flow control problem in a coupled optimality system, derived from first order sufficient optimality conditions, also known as Karush-Kuhn-Tucker (KKT) optimality conditions, provided by following theorem:

Theorem 2.4. *If the solution $(\boldsymbol{s},\boldsymbol{u},\boldsymbol{z}) \in S\times U\times Z$ exists for problem 2.2 then it satisfies following conditions:*

$$(A)\quad \begin{cases} \mathcal{F}(\boldsymbol{s},\boldsymbol{u}) = 0, \\ \mathcal{J}_{\boldsymbol{s}}(\boldsymbol{s},\boldsymbol{u}) + \mathcal{F}_{\boldsymbol{s}}(\boldsymbol{s},\boldsymbol{u})^{*}\boldsymbol{z} = 0, \\ \left\langle \tilde{\mathcal{J}}_{\boldsymbol{u}}(\boldsymbol{s},\boldsymbol{u}) + \mathcal{F}_{\boldsymbol{u}}(\boldsymbol{s},\boldsymbol{u})^{*}\boldsymbol{z},\boldsymbol{v}-\boldsymbol{u}\right\rangle \geq 0. \end{cases}$$

(A) is the coupled Karush-Kuhn-Tucker (KKT) optimality system comprising of state, adjoint equations, and optimality equations in the unknowns $\boldsymbol{s},\boldsymbol{z}$ and $\boldsymbol{u}$ respectively. For the Lagrangian, the KKT optimality system can be derived by satisfying first order optimality conditions for the Lagrangian. Thus,

Theorem 2.5. *Let $(\boldsymbol{s},\boldsymbol{u}) \in S\times U$ be the solution of optimal control problem 2.1, then there exists Lagrange multiplier $\boldsymbol{z}\in Z$ such that*

$$\nabla\mathcal{L}(\boldsymbol{s},\boldsymbol{u},\boldsymbol{z})[\boldsymbol{\xi},\boldsymbol{\tau},\boldsymbol{\kappa}] = 0,\ \forall(\boldsymbol{\xi},\boldsymbol{\tau},\boldsymbol{\kappa}) \in S\times U\times Z, \tag{2.15}$$

or equivalently,

$$\begin{cases} \langle \mathcal{L}_{\boldsymbol{z}}(\boldsymbol{s},\boldsymbol{u},\boldsymbol{z}),\boldsymbol{\kappa}\rangle = 0,\ \forall\ \boldsymbol{\kappa}\in Z \\ \langle \mathcal{L}_{\boldsymbol{s}}(\boldsymbol{s},\boldsymbol{u},\boldsymbol{z}),\boldsymbol{\xi}\rangle = 0,\ \forall\ \boldsymbol{\xi}\in S \\ \langle \mathcal{L}_{\boldsymbol{u}}(\boldsymbol{s},\boldsymbol{u},\boldsymbol{z}),\boldsymbol{\tau}\rangle \geq 0,\ \forall\ \boldsymbol{\tau}\in U, \end{cases}$$

or equivalently,

$$\begin{cases} \langle \mathcal{F}(\boldsymbol{s},\boldsymbol{u}),\boldsymbol{\xi}\rangle = 0,\ \forall\ \boldsymbol{\xi}\in S \\ \langle \mathcal{J}_{\boldsymbol{s}}(\boldsymbol{s},\boldsymbol{u}) + \mathcal{F}_{\boldsymbol{s}}(\boldsymbol{s},\boldsymbol{u})^{*}\boldsymbol{z},\boldsymbol{\kappa}\rangle = 0,\ \forall\ \boldsymbol{\kappa}\in Z \\ \left\langle \tilde{\mathcal{J}}_{\boldsymbol{u}}(\boldsymbol{s},\boldsymbol{u}) + \mathcal{F}_{\boldsymbol{u}}(\boldsymbol{s},\boldsymbol{u})^{*}\boldsymbol{z},\boldsymbol{\tau}\right\rangle \geq 0,\ \forall\ \boldsymbol{\tau}\in U. \end{cases}$$

The KKT optimality system can be solved through *one-shot* approach (see for example, [46, 98]), that targets for directly solving the system for all the unknown variables. However, such direct solution of such coupled systems can be complicated and therefore, require implementation of numerical approximation schemes. Thus, in the upcoming sections, we will solve the optimal flow control problem with *optimize-then-discretize* strategy, hence, dividing the solution process into two steps: *optimization*, that is, deriving coupled KKT optimality system, and *discretization*, that is, implementing numerical methods to solve the KKT system. Alternatively, one can opt for discretize-then-optimize approach, however, the choice is problem dependent.

2.4. Saddle-point framework for boundary control problems

In this section, we will implement the *optimization step* in the optimal flow control problems constrained by linear and non-linear primal equations, that are Stokes and Navier-Stokes equations respectively. In both cases, we consider a bounded domain $\Omega \subseteq \mathbb{R}^d, d \in \{2,3\}$ with Lipschitz boundary $\partial\Omega$. We divide $\partial\Omega$ into three parts, that are, Γ_{in}, the opening from which fluid enters Ω, Γ_o, the opening from which fluid leaves Ω and Γ_w, the lateral walls of Ω. Moreover, we assume Γ_w to be rigid and non-permeable.

Here, we will focus on derivation of the KKT optimality system from saddle-point definition of boundary control problems, to be introduced in the upcoming discussion and we will exploit the stability theory developed by Brezzi [30] and Babuška [15] for the saddle-point problems. In the next section, we will utilize the block-structure arising in such problems in implementation of the numerical schemes. We remark that in boundary control problems, the control is defined at the boundary ($\partial\Omega$) or parts of boundary, whereas, the distributed control problems quantify the control in entire computational domain (Ω) or its parts. We remark that although the formulation is similar in both cases, the former provides with an opportunity to quantify the unknown boundary conditions needed to match desired data in cardiovascular problems, which is the ultimate objective of this work.

2.4.1 Stokes constrained optimal flow control problem

Let us first consider steady-state Stokes equations modeling fluid flow in Ω. These state-constraints are defined in strong form as:

$$\begin{cases} -\eta \Delta \boldsymbol{v} + \nabla p = \boldsymbol{f}, & \text{in } \Omega, \\ \nabla \cdot \boldsymbol{v} = g, & \text{in } \Omega, \end{cases} \tag{2.16}$$

where $\boldsymbol{v}$ is velocity of the fluid, p is the pressure, $\boldsymbol{f}$ are body forces, $\eta > 0$ is kinematic viscosity and $g = 0$ leads to incompressible fluids case. We impose an arbitrary known velocity $\boldsymbol{v}_{in}$ in Dirichlet sense at the inlets Γ_{in} and owing to the non-permeability of Γ_w, we assume no-slip conditions there. Furthermore, we rely on simple Neumann conditions at the outlets and to quantify these conditions, we propose control implementation in them. Thus, with $\boldsymbol{u}$ representing control variables and $\boldsymbol{n}$ representing the outward normal to the outlets, the boundary conditions can be written as:

$$\begin{cases} \boldsymbol{v} = \boldsymbol{v}_{in}, & \text{on } \Gamma_{in}, \\ \boldsymbol{v} = \boldsymbol{0}, & \text{on } \Gamma_w, \\ -\eta \left(\nabla \boldsymbol{v}\right) \boldsymbol{n} + p\boldsymbol{n} = \boldsymbol{u}, & \text{on } \Gamma_o. \end{cases} \tag{2.17}$$

Moreover, we introduce quadratic tracking type objective functional $\mathcal{J}$ in our problem formulation, defined as:

$$\mathcal{J}\left(\boldsymbol{v}, p, \boldsymbol{u}\right) = \frac{1}{2}\|\boldsymbol{v} - \boldsymbol{v}_o\|^2_{Q(\Omega)} + \frac{\alpha}{2}\|\boldsymbol{u}\|^2_{U(\Gamma_o)}, \tag{2.18}$$

where the first term describes the aim of the problem, that is to match $\boldsymbol{v}$ with $\boldsymbol{v}_o$, the observation/desired velocity in Hilbert space $Q \supseteq V$. Moreover, $\alpha > 0$ will be manually tuned for to regularize the energy of control and the norms for fluid velocity, pressure and control are considered in respective Hilbert spaces V, P and U. Furthermore, it is to be noted that since we only wish to investigate the control at the outlet Γ_o, we define $U := U\left(\Gamma_o\right)$ and we assume equivalence between state and adjoint spaces, that is, $S = (V \times P) \equiv Z = (Z_{\boldsymbol{v}} \times Z_p)$. We define the Lagrangian by equation (2.2), where, $\langle \mathcal{F}\left(\boldsymbol{s}, \boldsymbol{u}\right), \boldsymbol{z} \rangle$ denotes residual of weak form of state constraints, given below:

$$\begin{cases} \mathrm{a}\left(\boldsymbol{v}, \boldsymbol{w}\right) + \mathrm{b}\left(p, \boldsymbol{w}\right) + \mathrm{c}\left(\boldsymbol{u}, \boldsymbol{w}\right) = \langle \boldsymbol{f}, \boldsymbol{w} \rangle, & \forall\ \boldsymbol{w} \in V, \\ \mathrm{b}\left(q, \boldsymbol{v}\right) = \langle g, q \rangle, & \forall\ q \in P. \end{cases} \tag{2.19}$$

Here the bilinear forms $\mathrm{a} : V \times V \to \mathbb{R}$ and $\mathrm{b} : V \times P \to \mathbb{R}$ are defined as:

$$\mathrm{a}\left(\boldsymbol{v}, \boldsymbol{w}\right) = \eta \int_\Omega \nabla \boldsymbol{v} \cdot \nabla \boldsymbol{w}\ d\Omega, \qquad \mathrm{b}\left(q, \boldsymbol{v}\right) = -\int_\Omega q \left(\nabla \cdot \boldsymbol{v}\right)\ d\Omega, \tag{2.20}$$

and $\mathrm{c} : U \times V \to \mathbb{R}$ is the bilinear term arising from non-homogenuous Neumann boundary conditions and is defined as:

$$\mathrm{c}\left(\boldsymbol{u}, \boldsymbol{w}\right) = -\int_{\Gamma_o} \boldsymbol{u} \cdot \boldsymbol{w} \; d\Gamma_o. \tag{2.21}$$

Furthermore, the objective functional $\mathcal{J}\left(\boldsymbol{s}, \boldsymbol{u}\right)$ can be re-written as:

$$\mathcal{J}\left(\boldsymbol{s}, \boldsymbol{u}\right) = \frac{1}{2}\mathrm{m}\left(\boldsymbol{v} - \boldsymbol{v}_o, \boldsymbol{v} - \boldsymbol{v}_o\right) + \frac{\alpha}{2}\mathrm{n}\left(\boldsymbol{u}, \boldsymbol{u}\right), \tag{2.22}$$

where, $\mathrm{m} : V \times V \to \mathbb{R}$ and $\mathrm{n} : U \times U \to \mathbb{R}$, defined below:

$$\mathrm{m}\left(\boldsymbol{v} - \boldsymbol{v}_o, \boldsymbol{\xi_v} - \boldsymbol{v}_o\right) = \left(\boldsymbol{v} - \boldsymbol{v}_o, \boldsymbol{\xi_v} - \boldsymbol{v}_o\right)_{Q(\Omega)}, \quad \mathrm{n}\left(\boldsymbol{u}, \boldsymbol{\xi_u}\right) = \left(\boldsymbol{u}, \boldsymbol{\xi_v}\right)_{U(\Gamma_o)}, . \tag{2.23}$$

The Lagrangian $\mathcal{L}\left(\boldsymbol{s}, \boldsymbol{u}, \boldsymbol{z}\right)$ can, thus, be written as:

$$\begin{aligned}\mathcal{L}\left(\boldsymbol{s}, \boldsymbol{u}, \boldsymbol{z}\right) = \frac{1}{2}\mathrm{m}\left(\boldsymbol{v} - \boldsymbol{v}_o, \boldsymbol{v} - \boldsymbol{v}_o\right) + \frac{\alpha}{2}\mathrm{n}\left(\boldsymbol{u}, \boldsymbol{u}\right) + \mathrm{a}\left(\boldsymbol{v}, \boldsymbol{w}\right) + \\ \mathrm{b}\left(p, \boldsymbol{w}\right) + \mathrm{b}\left(q, \boldsymbol{v}\right) + \mathrm{c}\left(\boldsymbol{u}, \boldsymbol{w}\right) - \left\langle \boldsymbol{f}, \boldsymbol{w}\right\rangle - \left\langle g, q\right\rangle\end{aligned}$$

The coupled KKT optimality system can be derived by requiring the first order optimality condition (2.15) for all $\left(\boldsymbol{\xi} = \left(\boldsymbol{\xi_v}, \boldsymbol{\xi}_p\right), \boldsymbol{\xi_u}, \boldsymbol{\kappa} = \left(\boldsymbol{\kappa_w}, \boldsymbol{\kappa}_q\right)\right) \in S \times U \times Z$ and the problem can be re-formulated as:

Problem 2.3. *Find* $\left(\boldsymbol{s} = \left(\boldsymbol{v}, p\right), \boldsymbol{u}, \boldsymbol{z} = \left(\boldsymbol{w}, q\right)\right) \in S \times U \times Z$ *that satisfies the following optimality system:*

$$\begin{cases} \mathrm{m}\left(\boldsymbol{v}, \boldsymbol{\xi_v}\right) + \mathrm{a}\left(\boldsymbol{w}, \boldsymbol{\xi_v}\right) + \mathrm{b}\left(q, \boldsymbol{\xi_v}\right) & = \mathrm{m}\left(\boldsymbol{v}_{obs}, \boldsymbol{\xi_v}\right), \\ \mathrm{b}\left(\boldsymbol{\xi}_p, \boldsymbol{w}\right) & = 0, \\ \alpha\mathrm{n}\left(\boldsymbol{u}, \boldsymbol{\xi_u}\right) + \mathrm{c}\left(\boldsymbol{\xi_u}, \boldsymbol{w}\right) & = 0, \\ \mathrm{a}\left(\boldsymbol{v}, \boldsymbol{\kappa_w}\right) + \mathrm{b}\left(p, \boldsymbol{\kappa_w}\right) + \mathrm{c}\left(\boldsymbol{u}, \boldsymbol{\kappa_w}\right) & = \left\langle \boldsymbol{f}, \boldsymbol{\kappa_w}\right\rangle, \\ \mathrm{b}\left(\boldsymbol{\kappa}_q, \boldsymbol{v}\right) & = \left\langle g, \boldsymbol{\kappa}_q\right\rangle. \end{cases} \tag{2.24}$$

In the system of linear equations (2.24), the first two equations account for adjoint equations, the third equation is the optimality condition and the last two equations are weak form of state constraints. Now, we cast the optimal flow control problem 2.3 in a saddle-point framework. For this purpose, we introduce $X = S \times U$ equipped with the inner product $\left(\cdot, \cdot\right)_X$, defined below:

$$\left(\mathbf{x}, \mathbf{y}\right)_X = \left(\boldsymbol{s}, \mathbf{y}_{\boldsymbol{s}}\right)_S + \left(\boldsymbol{u}, \mathbf{y}_{\boldsymbol{u}}\right)_U, \qquad \forall\ \mathbf{y} = \left(\mathbf{y}_{\boldsymbol{s}}, \mathbf{y}_{\boldsymbol{u}}\right) \in X.$$

Then the state-constraints (2.19) can be reformulated as below:

$$\mathcal{B}\left(\mathbf{x}, \boldsymbol{z}\right) - \left\langle \mathcal{G}, \boldsymbol{z}\right\rangle = 0, \tag{2.25}$$

where, the operator $\mathcal{B} : X \times Z \to \mathbb{R}$ is defined as:

$$\mathcal{B}(\mathbf{x}, \boldsymbol{z}) = \mathrm{a}(\boldsymbol{v}, \boldsymbol{w}) + \mathrm{b}(p, \boldsymbol{w}) + \mathrm{c}(\boldsymbol{u}, \boldsymbol{w}) + \mathrm{b}(q, \boldsymbol{v}), \tag{2.26}$$

and $\langle \mathcal{G}, \boldsymbol{z} \rangle = \langle \boldsymbol{f}, \boldsymbol{w} \rangle + \langle g, q \rangle$.

Moreover, the objective functional (2.22) can be re-written as:

$$J(\mathbf{x}) = \frac{1}{2}\mathcal{A}(\mathbf{x}, \mathbf{x}) - \langle \mathcal{H}, \mathbf{x} \rangle, \tag{2.27}$$

where $\mathcal{A}(\mathbf{x}, \mathbf{y}) = \mathrm{m}(\boldsymbol{s}, \mathbf{y}_{\boldsymbol{s}}) + \alpha \mathrm{n}(\boldsymbol{u}, \mathbf{y}_{\boldsymbol{u}})$ and $\langle \mathcal{H}, \mathbf{y} \rangle = \mathrm{m}(\boldsymbol{s}_{obs}, \mathbf{y}_{\boldsymbol{s}})$ for all $\mathbf{y} = (\mathbf{y}_{\boldsymbol{s}} = (\mathbf{y}_{\boldsymbol{v}}, \mathbf{y}_p), \mathbf{y}_{\boldsymbol{u}}) \in X$. We can re-write the optimal flow control problem 2.3 as the following saddle-point problem:

Problem 2.4. *Find the saddle-points $(\mathbf{x}, \boldsymbol{z}) \in X \times S$ of the following Lagrangian:*

$$\mathcal{L}(\mathbf{x}, \boldsymbol{z}) = J(\mathbf{x}) + \mathcal{B}(\mathbf{x}, \boldsymbol{z}) - \langle \mathcal{G}, \boldsymbol{z} \rangle, \tag{2.28}$$

or equivalently,

find $(\mathbf{x}, \boldsymbol{z}) \in X \times S$ such that,

$$\begin{cases} \mathcal{A}(\mathbf{x}, \mathbf{y}) + \mathcal{B}(\boldsymbol{z}, \mathbf{y}) = \langle \mathcal{H}, \mathbf{y} \rangle, & \forall\ \mathbf{y} \in X, \\ \mathcal{B}(\mathbf{x}, \boldsymbol{\kappa}) = \langle \mathcal{G}, \boldsymbol{\kappa} \rangle, & \forall\ \boldsymbol{\kappa} \in Z. \end{cases} \tag{2.29}$$

The coupled optimality system in saddle-point structure is given by equation (2.29), which is derived by satisfying first order Karush-Kuhn-Tucker optimality conditions for the Lagrangian (2.28). We recall that the optimality system (2.29) can be solved directly for the state, control and adjoint variables through *one-shot approach* [46, 98]. Next, we will give some results for existence and uniqueness of the solution to the saddle-point problem 2.4.

Theorem 2.6 (Brezzi's theorem)**.** *A unique solution to the saddle-point problem 2.4 will exist if the following conditions are satisfied,*

(*i*) *$\mathcal{A} : X \times X \to \mathbb{R}$ is continuous and satisfies,*

$$\exists\ a_0 > 0,\ \textit{such that}\ \inf_{\mathbf{x} \in X_0 \setminus \{0\}} \frac{\mathcal{A}(\mathbf{x}, \mathbf{x})}{\|\mathbf{x}\|_X^2} \geq a_0,$$

where, $X_0 = \{\mathbf{x} \in X\ \textit{such that}\ \mathcal{B}(\mathbf{x}, \boldsymbol{\kappa}) = 0\ \forall\ \boldsymbol{\kappa} \in Z\}$.

(*ii*) *$\mathcal{B} : X \times Z \to \mathbb{R}$ is continuous and satisfies the following inf-sup condition,*

$$\exists\ b_0 > 0,\ \textit{such that}\ \inf_{\boldsymbol{\kappa} \in Z \setminus \{0\}} \sup_{\mathbf{x} \in X \setminus \{0\}} \frac{\mathcal{B}(\mathbf{x}, \boldsymbol{\kappa})}{\|\mathbf{x}\|_X \|\boldsymbol{\kappa}\|_Z} \geq b_0.$$

Proof. To prove Brezzi's theorem, let us make a few assumptions on the bilinear forms defining $\mathcal{A}$ and $\mathcal{B}$. Let us assume that $\mathrm{m} : S \times S \to \mathbb{R}$ and $\mathrm{n} : U \times U \to \mathbb{R}$ are continuous and symmetric, moreover, m is positive and n is coercive, where $S = V \times P$. Furthermore, let us assume that $\mathrm{a} : V \times Z_{\boldsymbol{v}} \to \mathbb{R}$ and $\mathrm{b} : V \times Z_p \to \mathbb{R}$ are continuous such that a is coercive over $V_0 = \{\boldsymbol{v} \in V \text{ such that } \mathrm{b}(q, \boldsymbol{v}) = 0 \ \forall \ q \in Z_P\}$. Finally, let $\mathrm{c} : U \times Z_{\boldsymbol{v}} \to \mathbb{R}$ be symmetric and bounded, representing the action of the control. Then the continuity of $\mathcal{A}$ and $\mathcal{B}$ follows from the continuity of the bilinear operators appearing in their definitions. Next we will prove the coercivity of $\mathcal{A}$ over X_0 and the inf-sup condition for $\mathcal{B}$.

By definition, $\mathcal{A}(\mathbf{x}, \mathbf{x}) = \mathrm{m}(\boldsymbol{s}, \boldsymbol{s}) + \alpha \mathrm{n}(\boldsymbol{u}, \boldsymbol{u})$. Now, owing to coercivity of n for $C_1 > 0$ we can write,

$$\mathcal{A}(\mathbf{x}, \mathbf{x}) \geq \mathrm{m}(\boldsymbol{s}, \boldsymbol{s}) + \alpha C_1 \|\boldsymbol{u}\|^2 = \mathrm{m}(\boldsymbol{s}, \boldsymbol{s}) + \frac{\alpha C_1}{2}\|\boldsymbol{u}\|^2 + \frac{\alpha C_1}{2}\|\boldsymbol{u}\|^2.$$

Now, let us consider $\mathbf{x} = (\boldsymbol{s}, \boldsymbol{u}) \in X_0$, then, $\mathcal{B}(\mathbf{x}, \boldsymbol{\kappa}) = 0, \ \forall \boldsymbol{\kappa} \in Z$. Owing to strong coercivity of a over kernel of b and using Lax-Milgram lemma, from the above equation we get $\|\boldsymbol{u}\|_U \geq C_2 \|\boldsymbol{s}\|_S, \ C_2 > 0$. Furthermore, using the positivity of m, we can write,

$$\mathcal{A}(\mathbf{x}, \mathbf{x}) \geq \frac{\alpha C_1}{2C_2^2}\|\boldsymbol{s}\|_S^2 + \frac{\alpha C_1}{2}\|\boldsymbol{u}\|_U^2.$$

Now, if we consider $a_0 = \frac{\alpha C_1}{2} max\{1, C_2^2\} > 0$, then,

$$\mathcal{A}(\mathbf{x}, \mathbf{x}) \geq a_0 \|\mathbf{x}\|_X^2,$$

or equivalently,

$$\exists \ a_0 > 0, \text{ such that } \inf_{\mathbf{x} \in X_0 \setminus \{0\}} \frac{\mathcal{A}(\mathbf{x}, \mathbf{x})}{\|\mathbf{x}\|_X^2} \geq a_0.$$

Now to prove the inf-sup condition, let us consider $\mathfrak{a}(\boldsymbol{s}, \boldsymbol{z}) = \mathrm{a}(\boldsymbol{v}, \boldsymbol{z}) + \mathrm{b}(p, \boldsymbol{z}), \ \forall \boldsymbol{z} \in Z$. Then,

$$\sup_{\mathbf{x} \in X, \ \mathbf{x} \neq \mathbf{0}} \frac{\mathcal{B}(\mathbf{x}, \boldsymbol{z})}{\|\mathbf{x}\|_X} = \sup_{\mathbf{x} = (\boldsymbol{s}, \boldsymbol{u}) \in X = S \times U, \ \mathbf{x} \neq \mathbf{0}} \frac{\mathfrak{a}(\boldsymbol{s}, \boldsymbol{z}) + \mathrm{c}(\boldsymbol{u}, \boldsymbol{z})}{\left(\|\boldsymbol{s}\|_S^2 + \|\boldsymbol{u}\|_U^2\right)^{\frac{1}{2}}}.$$

Now, thanks to our earlier assumption of equivalence of state and adjoint spaces, that is, $S \equiv Z$, we can consider the supremum at $(\boldsymbol{s}, \boldsymbol{u}) = (\boldsymbol{z}, 0)$. Hence,

$$\sup_{\mathbf{x} \in X, \ \mathbf{x} \neq \mathbf{0}} \frac{\mathcal{B}(\mathbf{x}, \boldsymbol{z})}{\|\mathbf{x}\|_X} \geq_{(\boldsymbol{s}, \boldsymbol{u}) = (\boldsymbol{z}, 0)} \frac{\mathfrak{a}(\boldsymbol{z}, \boldsymbol{z})}{\|\boldsymbol{z}\|_S},$$

and since a is coercive over kernel of b, that is, there exists $b_0 > 0$ such that

$$\inf_{\boldsymbol{v} \in V_0 \setminus \{0\}} \frac{\mathrm{a}(\boldsymbol{z}, \boldsymbol{z})}{\|\boldsymbol{z}\|_S^2} \geq b_0,$$

we can write,

$$\sup_{\mathbf{x} \in X, \ \mathbf{x} \neq \mathbf{0}} \frac{\mathcal{B}(\mathbf{x}, \boldsymbol{z})}{\|\mathbf{x}\|_X} \geq b_0 \|\boldsymbol{z}\|_S = b_0 \|\boldsymbol{z}\|_Z.$$

□

2.4.2 Navier-Stokes constrained optimal flow control problem

Now, in case of steady Navier-Stokes equations modeling fluid flow in $\Omega \subseteq \mathbb{R}^d,\ d \in \{2,3\}$, we write the state constraints in strong form as below:

$$\begin{cases} -\eta \Delta \boldsymbol{v} + (\boldsymbol{v} \cdot \nabla)\, \boldsymbol{v} + \nabla p = \boldsymbol{f}, & \text{in } \Omega, \\ \nabla \cdot \boldsymbol{v} = g, & \text{in } \Omega. \end{cases} \tag{2.30}$$

The boundary conditions in this problem are defined by equations (2.17) and the tracking-type cost functional defined by equation (2.18). Moreover, we consider the Hilbert state and adjoint spaces, $S(\Omega) = V(\Omega) \times P(\Omega) \equiv Z(\Omega) = Z_{\boldsymbol{v}}(\Omega) \times Z_p(\Omega)$ and the control space, $U(\Gamma_o)$, then the state-constraints (2.30) can be written in weak formulation as:

$$\begin{cases} \mathrm{a}(\boldsymbol{v}, \boldsymbol{w}) + \mathrm{b}(p, \boldsymbol{w}) + \mathrm{e}(\boldsymbol{v}, \boldsymbol{v}, \boldsymbol{w}) + \mathrm{c}(\boldsymbol{u}, \boldsymbol{w}) = \langle \boldsymbol{f}, \boldsymbol{w} \rangle, & \forall\ \boldsymbol{w} \in Z_v, \\ \mathrm{b}(q, \boldsymbol{v}) = \langle g, q \rangle, & \forall\ q \in Z_p. \end{cases} \tag{2.31}$$

Here, $\mathrm{e}(\boldsymbol{v}, \boldsymbol{v}, \boldsymbol{w})$ is non-linear convection term, defined as:

$$\mathrm{e}(\boldsymbol{v}, \boldsymbol{v}, \boldsymbol{w}) = \int_{\Omega} (\boldsymbol{v} \cdot \nabla)\, \boldsymbol{v} \cdot \boldsymbol{w}\ d\Omega,$$

and $\mathrm{a} : V \times V \to \mathbb{R}$, $\mathrm{b} : V \times P \to \mathbb{R}$ and $\mathrm{c} : V \times U \to \mathbb{R}$ are given in equations (2.20) and (2.21). The cost functional (2.18) can be reformulated as in equation (2.22) and we define the Lagrangian, $\mathcal{L}(\boldsymbol{s}, \boldsymbol{u}, \boldsymbol{z}) : S \times U \times Z \to \mathbb{R}$, as below:

$$\begin{aligned} \mathcal{L}(\boldsymbol{s}, \boldsymbol{u}, \boldsymbol{z}) = \frac{1}{2}\mathrm{m}(\boldsymbol{v} - \boldsymbol{v}_{obs}, \boldsymbol{v} - \boldsymbol{v}_{obs}) + \frac{\alpha}{2}\mathrm{n}(\boldsymbol{u}, \boldsymbol{u}) + \mathrm{a}(\boldsymbol{v}, \boldsymbol{w})\ +\ \mathrm{e}(\boldsymbol{v}, \boldsymbol{v}, \boldsymbol{w})\ + \\ +\ \mathrm{b}(p, \boldsymbol{w})\ +\ \mathrm{b}(q, \boldsymbol{v})\ +\ \mathrm{c}(\boldsymbol{u}, \boldsymbol{w})\ -\ \langle \boldsymbol{f}, \boldsymbol{w} \rangle -\ \langle g, q \rangle \end{aligned}$$

First order KKT optimality conditions will give rise to the following coupled optimality system:

$$\begin{cases} \mathrm{m}(\boldsymbol{v}, \boldsymbol{\xi_v}) + \mathrm{e}(\boldsymbol{\xi_v}, \boldsymbol{v}, \boldsymbol{w}) + \mathrm{e}(\boldsymbol{v}, \boldsymbol{\xi_v}, \boldsymbol{w}) + \mathrm{a}(\boldsymbol{w}, \boldsymbol{\xi_v}) + \mathrm{b}(q, \boldsymbol{\xi_v}) & = \mathrm{m}(\boldsymbol{v}_{obs}, \boldsymbol{\xi_v}), \\ \mathrm{b}(\boldsymbol{\xi}_p, \boldsymbol{w}) & = 0, \\ \alpha \mathrm{n}(\boldsymbol{u}, \boldsymbol{\xi_u}) +\ \mathrm{c}(\boldsymbol{\xi_u}, \boldsymbol{w}) & = 0, \\ \mathrm{e}(\boldsymbol{v}, \boldsymbol{v}, \boldsymbol{\kappa_w}) + \mathrm{a}(\boldsymbol{v}, \boldsymbol{\kappa_w}) +\ \mathrm{b}(p, \boldsymbol{\kappa_w}) +\ \mathrm{c}(\boldsymbol{u}, \boldsymbol{\kappa_w}) & = \langle \boldsymbol{f}, \boldsymbol{\kappa_w} \rangle, \\ \mathrm{b}(\boldsymbol{\kappa}_q, \boldsymbol{v}) & = \langle g, \boldsymbol{\kappa}_q \rangle, \end{cases} \tag{2.32}$$

for all $(\boldsymbol{\xi} = (\boldsymbol{\xi_v}, \boldsymbol{\xi}_p), \boldsymbol{\xi_u}, \boldsymbol{\kappa} = (\boldsymbol{\kappa_w}, \boldsymbol{\kappa}_q)) \in S \times U \times Z$ such that $\mathrm{e}(\boldsymbol{\xi_v}, \boldsymbol{v}, \boldsymbol{w})$ and $\mathrm{e}(\boldsymbol{v}, \boldsymbol{\xi_v}, \boldsymbol{w})$ are trilinear terms arising in adjoint equations.

Now, to put the problem in a saddle-point framework, we proceed in a similar way as for Stokes constrained problem and consider the bilinear functional $\mathcal{B} : X \times Z \to \mathbb{R}$, defined

by equation (2.26) and the bilinear functional $\mathcal{A} : X \times X \to \mathbb{R}$, defined as, $\mathcal{A}(\mathbf{x}, \mathbf{y}) = \mathrm{m}(\boldsymbol{s}, \mathbf{y}_{\boldsymbol{s}}) + \alpha \mathrm{n}(\boldsymbol{u}, \mathbf{y}_{\boldsymbol{u}})$, $\forall \mathbf{y} = (\mathbf{y}_{\boldsymbol{s}} = (\mathbf{y}_{\boldsymbol{v}}, \mathbf{y}_p), \mathbf{y}_{\boldsymbol{u}}) \in X$. Then, Navier-Stokes constrained optimal flow control problem in saddle-point form reads:

Problem 2.5. *Find the saddle-points* $(\mathbf{x}, \boldsymbol{z}) \in X \times Z$ *of the following Lagrangian:*

$$\mathcal{L}(\mathbf{x}, \boldsymbol{z}) = J(\mathbf{x}) + \mathcal{B}(\mathbf{x}, \boldsymbol{z}) + \mathrm{e}(\boldsymbol{v}, \boldsymbol{v}, \boldsymbol{w}) - \langle \mathcal{G}, \boldsymbol{z} \rangle, \tag{2.33}$$

or equivalently,

Find $(\mathbf{x}, \boldsymbol{z}) \in X \times Z$*, such that,*

$$\begin{cases} \mathcal{A}(\mathbf{x}, \mathbf{y}) + \mathcal{B}(\mathbf{y}, \boldsymbol{z}) + \mathrm{e}(\mathbf{y}_{\boldsymbol{v}}, \boldsymbol{v}, \boldsymbol{w}) + \mathrm{e}(\boldsymbol{v}, \mathbf{y}_{\boldsymbol{v}}, \boldsymbol{w}) = \langle \mathcal{H}, \mathbf{y} \rangle, & \forall\ \mathbf{y} \in X, \\ \mathcal{B}(\mathbf{x}, \boldsymbol{\kappa}) + \mathrm{e}(\boldsymbol{v}, \boldsymbol{v}, \boldsymbol{\kappa}_{\boldsymbol{v}}) = \langle \mathcal{G}, \boldsymbol{\kappa} \rangle, & \forall\ \boldsymbol{\kappa} \in Z. \end{cases} \tag{2.34}$$

The system of equations (2.34) is the non-linear KKT optimality system, arising from satisfying the optimality conditions for the Lagrangian (2.33).

2.5. Numerical approximations

In this section, we will introduce the *discretization step*, or in other words, *Galerkin finite element (FE) approximations* of the optimal flow control problems constrained by Stokes and Navier-Stokes equations, discussed in sections 2.4.1 and 2.4.2 respectively. Let us consider discretization $\mathcal{T}_h$ of the domain Ω with size $0 < h \in \mathbb{R}^+ < \infty$, such that $\mathcal{T}_h = \cup_i \mathcal{S}_i$, where, $\mathcal{S}_i$ corresponds to ith-simplex. Furthermore, let us consider finite-dimensional state, control and adjoint spaces $S_h = V_h \times P_h \subset S$, $U_h \subset U$ and $Z_h \subset Z$. We will denote dimensions of these spaces by $\mathcal{N}$ along with corresponding variable in subscript. Thus,

$$\dim(S_h) = \dim(V_h) + \dim(P_h) = \mathcal{N}_{\boldsymbol{v}} + \mathcal{N}_p, \quad \text{and} \qquad \dim(U_h) = \mathcal{N}_{\boldsymbol{u}}.$$

Furthermore, we keep the assumption $S_h \equiv Z_h$, then, $\dim(Z_h) = \dim(S_h)$ and global dimensions of these finite element spaces will thus be $\mathcal{N} = 2\mathcal{N}_{\boldsymbol{s}} + \mathcal{N}_{\boldsymbol{u}}$. The subscript h indicates that $\mathcal{N} = \mathcal{N}(h)$.

2.5.1 Galerkin FE approximation of Stokes constrained ootimal flow control problem

Consider $X_h = (S_h \times U_h) \subset X$, then discretized form of Stokes constrained optimal flow control problem (2.29) reads:

Problem 2.6. *Find* $(\mathbf{x}_h, \boldsymbol{z}_h) \in X_h \times Z_h$ *such that*

$$\begin{cases} \mathcal{A}(\mathbf{x}_h, \mathbf{y}_h) + \mathcal{B}(\boldsymbol{z}_h, \mathbf{y}_h) = \langle \mathcal{H}, \mathbf{y}_h \rangle, & \forall\ \mathbf{y}_h \in X_h, \\ \mathcal{B}(\mathbf{x}_h, \boldsymbol{\kappa}_h) = \langle \mathcal{G}, \boldsymbol{\kappa}_h \rangle, & \forall\ \boldsymbol{\kappa}_h \in Z_h. \end{cases} \tag{2.35}$$

Let $\boldsymbol{\phi}, \boldsymbol{\psi}, \boldsymbol{\sigma}$ denote the basis functions such that,

$$V_h = \operatorname{span}\left\{\boldsymbol{\phi}_i\right\}_{i=1}^{\mathcal{N}_{\boldsymbol{v}}}, \qquad P_h = \operatorname{span}\left\{\boldsymbol{\psi}_k\right\}_{k=1}^{\mathcal{N}_p}, \qquad U_h = \operatorname{span}\left\{\boldsymbol{\sigma}_l\right\}_{l=1}^{\mathcal{N}_{\boldsymbol{u}}} \tag{2.36}$$

Then, for $1 \leq i \leq \mathcal{N}_{\boldsymbol{v}}$, $1 \leq l \leq \mathcal{N}_{\boldsymbol{u}}$ and $1 \leq k \leq \mathcal{N}_p$, the bilinear forms $\mathcal{A} : X_h \times X_h \to \mathbb{R}$ and $\mathcal{B} : X_h \times Z_h \to \mathbb{R}$ in system (2.35), are defined as:

$$\begin{cases} \mathcal{A}\left(\mathbf{x}_h, \mathbf{y}_h\right) = \sum\limits_{j=1}^{\mathcal{N}_{\boldsymbol{v}}} v_h^j \mathrm{m}\left(\boldsymbol{\phi}_j, \boldsymbol{\phi}_i\right) + \alpha \sum\limits_{j=1}^{\mathcal{N}_{\boldsymbol{u}}} u_h^j \mathrm{n}\left(\boldsymbol{\sigma}_j, \boldsymbol{\sigma}_l\right), \\ \mathcal{B}\left(\boldsymbol{z}_h, \mathbf{y}_h\right) = \sum\limits_{j=1}^{\mathcal{N}_{\boldsymbol{v}}} w_h^j \mathrm{a}\left(\boldsymbol{\phi}_j, \boldsymbol{\phi}_i\right) + \sum\limits_{j=1}^{\mathcal{N}_{\boldsymbol{v}}} w_h^j \mathrm{b}\left(\boldsymbol{\psi}_k, \boldsymbol{\phi}_j\right) + \sum\limits_{j=1}^{\mathcal{N}_{\boldsymbol{v}}} w_h^j \mathrm{c}\left(\boldsymbol{\sigma}_l, \boldsymbol{\phi}_j\right) + \sum\limits_{j=1}^{\mathcal{N}_p} q_h^j \mathrm{b}\left(\boldsymbol{\psi}_j, \boldsymbol{\phi}_i\right), \\ \mathcal{B}\left(\mathbf{x}_h, \boldsymbol{\kappa}_h\right) = \sum\limits_{j=1}^{\mathcal{N}_{\boldsymbol{v}}} v_h^j \mathrm{a}\left(\boldsymbol{\phi}_j, \boldsymbol{\phi}_i\right) + \sum\limits_{j=1}^{\mathcal{N}_p} p_h^j \mathrm{b}\left(\boldsymbol{\psi}_j, \boldsymbol{\phi}_i\right) + \sum\limits_{j=1}^{\mathcal{N}_{\boldsymbol{u}}} u_h^j \mathrm{c}\left(\boldsymbol{\sigma}_j, \boldsymbol{\phi}_i\right) + \sum\limits_{j=1}^{\mathcal{N}_{\boldsymbol{v}}} v_h^j \mathrm{b}\left(\boldsymbol{\psi}_k, \boldsymbol{\phi}_j\right). \end{cases} \tag{2.37}$$

Thus, expanding the optimality system (2.35), we get,

$$\begin{cases} \sum\limits_{j=1}^{\mathcal{N}_{\boldsymbol{v}}} v_h^j \mathrm{m}\left(\boldsymbol{\phi}_j, \boldsymbol{\phi}_i\right) + \sum\limits_{j=1}^{\mathcal{N}_{\boldsymbol{v}}} w_h^j \mathrm{a}\left(\boldsymbol{\phi}_j, \boldsymbol{\phi}_i\right) + \sum\limits_{j=1}^{\mathcal{N}_p} q_h^j \mathrm{b}\left(\boldsymbol{\psi}_j, \boldsymbol{\phi}_i\right) &= \langle \mathcal{H}, \boldsymbol{\phi}_i \rangle, \\ \sum\limits_{j=1}^{\mathcal{N}_{\boldsymbol{v}}} w_h^j \mathrm{b}\left(\boldsymbol{\psi}_k, \boldsymbol{\phi}_j\right) &= 0, \\ \alpha \sum\limits_{j=1}^{\mathcal{N}_{\boldsymbol{u}}} u_h^j \mathrm{n}\left(\boldsymbol{\sigma}_j, \boldsymbol{\sigma}_l\right) + \sum\limits_{j=1}^{\mathcal{N}_{\boldsymbol{v}}} w_h^j \mathrm{c}\left(\boldsymbol{\sigma}_l, \boldsymbol{\phi}_j\right) &= 0, \\ \sum\limits_{j=1}^{\mathcal{N}_{\boldsymbol{v}}} v_h^j \mathrm{a}\left(\boldsymbol{\phi}_j, \boldsymbol{\phi}_i\right) + \sum\limits_{j=1}^{\mathcal{N}_p} p_h^j \mathrm{b}\left(\boldsymbol{\psi}_j, \boldsymbol{\phi}_i\right) + \sum\limits_{j=1}^{\mathcal{N}_{\boldsymbol{u}}} u_h^j \mathrm{c}\left(\boldsymbol{\sigma}_j, \boldsymbol{\phi}_i\right) &= \langle \boldsymbol{f}, \boldsymbol{\phi}_i \rangle, \\ \sum\limits_{j=1}^{\mathcal{N}_{\boldsymbol{v}}} v_h^j \mathrm{b}\left(\boldsymbol{\psi}_k, \boldsymbol{\phi}_j\right) &= \langle g, \boldsymbol{\psi}_k \rangle. \end{cases} \tag{2.38}$$

Let us define the bijections $V_h \leftrightarrow \mathbb{R}^{\mathcal{N}_{\boldsymbol{v}}}$, $P_h \leftrightarrow \mathbb{R}^{\mathcal{N}_p}$ and $U_h \leftrightarrow \mathbb{R}^{\mathcal{N}_{\boldsymbol{u}}}$, such that

$$\mathbf{v} = \left(v_h^1,\ v_h^2,\ \cdots,\ v_h^{\mathcal{N}_{\boldsymbol{v}}}\right)^T \leftrightarrow \boldsymbol{v}_h = \sum_{j=1}^{\mathcal{N}_{\boldsymbol{v}}} v_h^j \boldsymbol{\phi}_j \in V_h,$$

$$\mathbf{w} = \left(w_h^1,\ w_h^2,\ \cdots,\ w_h^{\mathcal{N}_{\boldsymbol{v}}}\right)^T \leftrightarrow \boldsymbol{w}_h = \sum_{j=1}^{\mathcal{N}_{\boldsymbol{v}}} w_h^j \boldsymbol{\phi}_j \in V_h,$$

$$\mathbf{p} = \left(p_h^1,\ p_h^2,\ \cdots,\ p_h^{\mathcal{N}_p}\right)^T \leftrightarrow p_h = \sum_{j=1}^{\mathcal{N}_p} p_h^j \boldsymbol{\psi}_j \in P_h,$$

$$\mathbf{q} = \left(q_h^1,\ q_h^2,\ \cdots,\ q_h^{\mathcal{N}_p}\right)^T \leftrightarrow q_h = \sum_{j=1}^{\mathcal{N}_p} q_h^j \boldsymbol{\psi}_j \in P_h,$$

and

$$\mathbf{u} = \left(u_h^1,\ u_h^2,\ \cdots,\ u_h^{\mathcal{N}_{\boldsymbol{u}}}\right)^T \leftrightarrow \boldsymbol{u}_h = \sum_{j=1}^{\mathcal{N}_{\boldsymbol{u}}} u_h^j \boldsymbol{\sigma}_j \in U_h.$$

Then the system (2.38) can be algebraically written as:

$$\begin{bmatrix} M & 0 & 0 & A & B \\ 0 & 0 & 0 & B^T & 0 \\ 0 & 0 & N & C & 0 \\ A & B^T & C & 0 & 0 \\ B & 0 & 0 & 0 & 0 \end{bmatrix} \begin{bmatrix} \mathbf{v} \\ \mathbf{p} \\ \mathbf{u} \\ \mathbf{w} \\ \mathbf{q} \end{bmatrix} = \begin{bmatrix} \mathbf{h} \\ \mathbf{0} \\ \mathbf{0} \\ \mathbf{f} \\ \mathbf{g} \end{bmatrix}, \tag{2.39}$$

where

$$(M)_{ij} = \mathrm{m}\left(\boldsymbol{\phi}_j, \boldsymbol{\phi}_i\right), \quad (N)_{lj} = \mathrm{n}\left(\boldsymbol{\sigma}_j, \boldsymbol{\sigma}_l\right), \quad (\mathbf{h})_i = \langle \mathcal{H}, \boldsymbol{\phi}_i \rangle, \quad (\mathbf{f})_i = \langle \boldsymbol{f}, \boldsymbol{\phi}_i \rangle, \tag{2.40}$$

$$(A)_{ij} = \mathrm{a}\left(\boldsymbol{\phi}_i, \boldsymbol{\phi}_j\right), \quad (B)_{ik} = \mathrm{b}\left(\boldsymbol{\psi}_k, \boldsymbol{\phi}_i\right), \quad (C)_{il} = \mathrm{c}\left(\boldsymbol{\sigma}_l, \boldsymbol{\phi}_i\right), \quad (\mathbf{g})_k = \langle \boldsymbol{g}, \boldsymbol{\psi}_k \rangle. \tag{2.41}$$

Existence of a unique solution to problem 2.6 will be ensured by satisfying Brezzi's theorem at the numerical level too. The finite dimensional version of Brezzi's theorem is given below:

Theorem 2.7. *A unique solution to the saddle-point problem 2.6 will exist if the following conditions are satisfied,*

(i) $\mathcal{A} : X_h \times X_h \to \mathbb{R}$ *is continuous and satisfies,*

$$\exists\ a_{h_0} > 0,\ \textit{such that} \inf_{\mathbf{x}_h \in X_{h_0} \setminus \{0\}} \frac{\mathcal{A}\left(\mathbf{x}_h, \mathbf{x}_h\right)}{\|\mathbf{x}_h\|_{X_h}^2} \geq a_{h_0},$$

where, $X_{h_0} = \{\mathbf{x}_h \in X_h$ *such that* $\mathcal{B}\left(\mathbf{x}_h, \boldsymbol{\kappa}_h\right) = 0\ \forall\ \boldsymbol{\kappa}_h \in Z_h\}$.

(ii) $\mathcal{B} : X_h \times Z_h \to \mathbb{R}$ *is continuous and satisfies the following inf-sup condition,*

$$\exists\ b_{h_0} > 0,\ \textit{such that} \inf_{\boldsymbol{z}_h \in Z_h \setminus \{0\}} \sup_{\mathbf{x}_h \in X_h \setminus \{0\}} \frac{\mathcal{B}\left(\mathbf{x}_h, \boldsymbol{z}_h\right)}{\|\mathbf{x}_h\|_{X_h} \|\boldsymbol{z}_h\|_{Z_h}} \geq b_{h_0}.$$

Furthermore, to ensure uniqueness of pressure and avoid any corresponding spurious nodes, we need to ensure surjectivity of the divergence operator at the finite element level. In other words, we need to satisfy the discretized form of Ladyzhenskaya-Brezzi-Babška (LBB) inf-sup condition, given in the following equation.

$$\exists\ \gamma_0 > 0,\ \text{such that} \inf_{\kappa_{\boldsymbol{w}} \in Q_v \setminus \{0\}} \sup_{\xi_p \in P \setminus \{0\}} \frac{\mathrm{b}\left(\kappa_{\boldsymbol{w}}, \xi_p\right)}{\|\kappa_{\boldsymbol{w}}\|_{Q_v} \|\xi_p\|_P} \geq \gamma_0 \tag{2.42}$$

The proof for continuity of bilinear forms $\mathcal{A} : X_h \times X_h \to \mathbb{R}$ and $\mathcal{B} : X_h \times Z_h \to \mathbb{R}$, and coercivity of $\mathcal{A} : X_h \times X_h \to \mathbb{R}$ over X_{h_0}, required in theorem 2.7 can be replicated

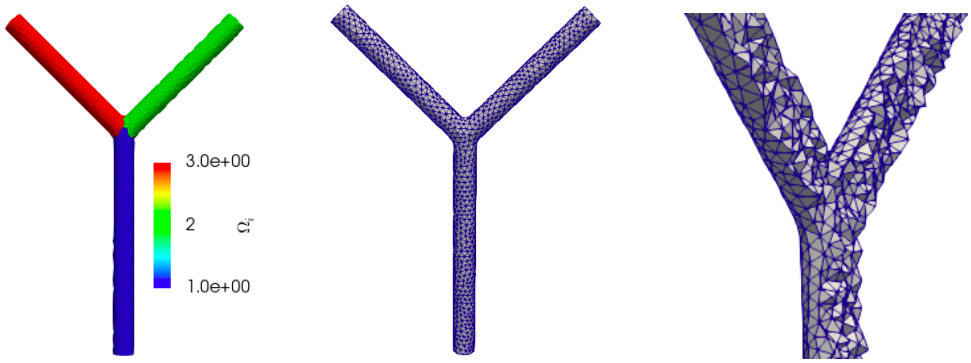

(a). (b). (c).

Figure 2.5.1: (a). Domain (Ω), (b). Triangular mesh on boundary ($\partial\Omega$), (c). Tetrahedral volume mesh, clipped view.

from the proof of the continuous form of Brezzi's theorem (see theorem 2.6). The inf-sup condition in theorem 2.7(ii), also known as Brezzi's inf-sup condition, will be satisfied if $S_h \equiv Z_h$ which is our earlier assumption. Moreover, LBB inf-sup condition will be satisfied for example, for stable finite element spaces such as Taylor-Hood pair $\mathbb{P}2-\mathbb{P}1$ with generic Lagrangian bases elements. In case, one utilizes unstable $\mathbb{P}1-\mathbb{P}1$ pair, the stability of pressure can be ensured through stabilization techniques [8, 9].

2.5.2 Numerical results: Stokes constrained optimal flow control problem

In this section, we will demonstrate the numerical results for the application of Stokes constrained optimal flow control framework. In this test problem, we will deal with a three-dimensional geometry, comprising of three cylinders connected in the shape of alphabet Y. Each cylinder corresponds to a subdomain, denoted by $\Omega_i, i = 1, 2, 3$ and is marked with different color (see figure 2.5.1(a)), thus, $\Omega = \cup_i \Omega_i, i = 1, 2, 3$. We discretize Ω in $\mathcal{T}_h = \cup_i \mathcal{S}_i$, where, $\mathcal{S}_i$ are tetrahedrons (see figure 2.5.1(c)), thus, $\partial\Omega$ comprise of triangular elements (see figure 2.5.1(b)). The flow will enter Ω through the tops of Ω_2 and Ω_3 and will leave through the bottom of Ω_1. Thus, Γ_{in} will denote the openings at the top of Ω_2 and Ω_3, and Γ_o will correspond to the opening at the bottom of Ω_1. The domain Ω can be considered as an idealized model of a blood vessel connected with another vessel, in the shape of Y.

The state constraints, in this case, are modeled by Stokes equations (2.16) and the boundary conditions are defined by equations (2.17). In equations (2.17), $\boldsymbol{v}_{in}$ is the

Poiseuille velocity imposed at inlets Γ_{in} in Dirichlet sense and is defined as below:

$$\boldsymbol{v}_{in} = -\frac{\eta Re}{R_{in}}\left(1 - \frac{r^2}{R_{in}^2}\right)\boldsymbol{n}_{in}, \tag{2.43}$$

where, η is constant viscosity, R_{in} is the maximum radius of the circular inlets, $\boldsymbol{n}_{in}$ corresponds to outward normals to the inlets Γ_{in}, $Re = 300$ is Reynolds number and r is the distance between center of an inlet and corresponding mesh nodes. The control is implemented over the outlet Γ_o, and restriction of control function $\boldsymbol{u}$ over mesh nodes of Γ_o is illustrated in figure 2.5.2(a).

At the continuous level, we consider $H^1(\Omega)$ for velocity such that the Dirichlet boundary conditions are interpreted in the sense of trace operators. Thus,

$$V(\Omega) = \left[H^1_{\Gamma_{in}\cup\Gamma_w}(\Omega)\right]^3 = \left[\boldsymbol{v} \in H^1\left[(\Omega)\right]^3 :\ \boldsymbol{v}|_{\Gamma_{in}} = \boldsymbol{v}_{in} \text{ and } \boldsymbol{v}|_{\Gamma_w} = \boldsymbol{0}\right]. \tag{2.44}$$

Moreover, pressure, p and control $\boldsymbol{u}$ are considered in $P(\Omega) = L^2(\Omega)$ and $U = \left[L^2(\Gamma_o)\right]^3$, respectively. Furthermore, let us denote the axes of the cylinders Ω_i by $\boldsymbol{t}_i$ for $i = 1, 2, 3$. Then, in this test case, we will consider the tracking-type objective functional (2.18), where the goal is to match desired velocity $\boldsymbol{v_o} \in Q(\Omega) = \left[L^2(\Omega)\right]^3$, defined through following parabolic expression:

$$\boldsymbol{v_o} = v_{const}\left(1 - \frac{r^2}{R_i^2}\right)\boldsymbol{t}_i,\ i \in \{1, 2, 3\}. \tag{2.45}$$

Here, R_i corresponds to maximum radius of Ω_i, v_{const} is the magnitude of velocity and r is the distance between the mesh nodes and the points on $\boldsymbol{t}_i$. We consider desired velocity distributed through equation (2.45) across Ω, with magnitude $v_{const} = 400\ mm/s$ (see figure 2.5.2(b)). The optimal flow control problem 2.1 can be stated as:

Problem 2.7. *Find* $(\boldsymbol{v}, p) \in H^1_{\Gamma_{in}\cup\Gamma_w}(\Omega) \times L^2(\Omega)$ *and* $\boldsymbol{u} \in \left[L^2(\Gamma_o)\right]^3$ *such that objective functional* (2.18) *is minimized subject to* $\mathcal{F}(\boldsymbol{v}, p, \boldsymbol{u}) = 0$ *and boundary conditions* (2.17)*, where,* $\mathcal{F}(\boldsymbol{v}, p, \boldsymbol{u}) : S \times U \to S^*,\ S^* = H^{-1}(\Omega) \times L^2(\Omega)$ *denotes the residual of Stokes equations* (2.16)*.*

Moreover, we consider the adjoint variables or Lagrange multipliers $\boldsymbol{z} = (\boldsymbol{w}, q) \in Z \equiv S$. The discretized coupled KKT optimality system can be derived following the algorithm discussed earlier and is given by equations (2.38) or equivalently, by the system (2.39). We have utilized multiphenics [1] to solve this optimality system with Taylor-Hood ($\mathbb{P}2 - \mathbb{P}1$) spaces for state and adjoint velocity and pressure and $\mathbb{P}2$ for control, leading to the total degrees of freedom ($\mathcal{N}$) to be 225248. Initially, the uncontrolled solution, that is, the solution to Stokes equations with homogenuous Neumann outflow conditions is calculated and the uncontrolled Stokes velocity is shown in figure 2.5.3(a). The velocity achieved through implementation of the optimal flow control framework is shown in figure 2.5.3(b)

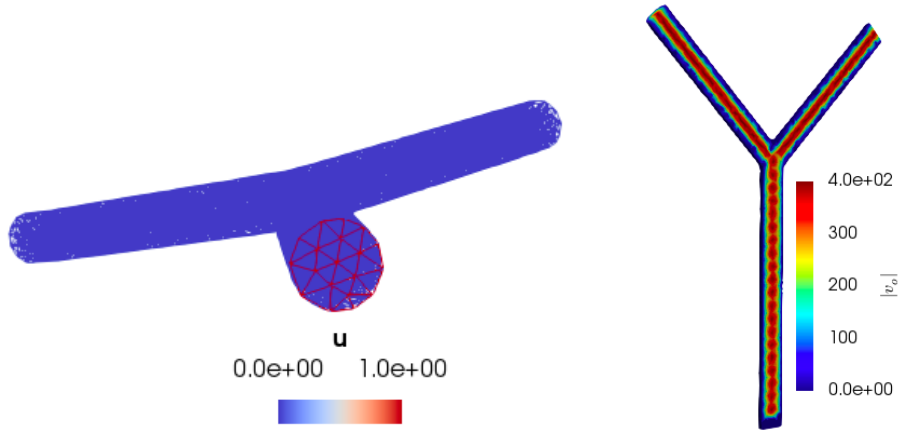

(a). (b).

Figure 2.5.2: (a). $\boldsymbol{u} \in U(\Gamma_o)$, (b). Case I: desired velocity $\boldsymbol{v_o}$ (mm/s).

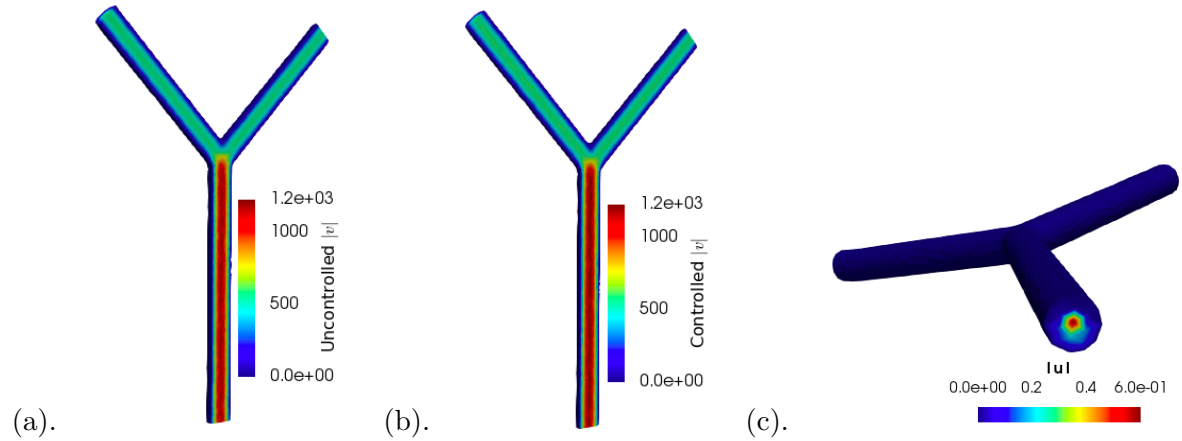

(a). (b). (c).

Figure 2.5.3: (a). Uncontrolled velocity (mm/s), (b). Controlled velocity (mm/s), (c). Boundary control (mm^2/s^2).

and the boundary control attained in this case is illustrated in figure 2.5.3(c). Moreover, we report that it takes 120.7 seconds to develop the controlled solution from the uncontrolled Stokes solution and for computational details, we refer the reader to table 2.1.

2.5.3 Galerkin FE approximation of Navier-Stokes constrained optimal flow control problem

Now, let us turn our attention towards the approximation of Navier-Stokes constrained optimal flow control problem through Galerkin finite element methods. We consider the finite element discretized spaces $X_h \subset X$ and $Z_h \subset Z$ as before, then the nonlinear optimality system (2.34) can be written in discretized form as:

$$\begin{cases} \mathcal{A}\left(\mathbf{x}_h, \mathbf{y}_h\right) + \mathcal{B}\left(\mathbf{y}_h, \boldsymbol{z}_h\right) + \mathrm{e}\left(\mathbf{y}_{\boldsymbol{v}_h}, \boldsymbol{v}_h, \boldsymbol{w}_h\right) + \mathrm{e}\left(\boldsymbol{v}_h, \mathbf{y}_{\boldsymbol{v}_h}, \boldsymbol{w}_h\right) = \langle \mathcal{H}, \mathbf{y}_h \rangle, & \forall\ \mathbf{y}_h \in X_h, \\ \mathcal{B}\left(\mathbf{x}_h, \boldsymbol{\kappa}_h\right) + \mathrm{e}\left(\boldsymbol{v}_h, \boldsymbol{v}_h, \boldsymbol{\kappa}_{\boldsymbol{v}_h}\right) = \langle \mathcal{G}, \boldsymbol{\kappa}_h \rangle, & \forall\ \boldsymbol{\kappa}_h \in Z_h, \end{cases} \tag{2.46}$$

where, $\mathcal{A}\left(\mathbf{x}_h, \mathbf{y}_h\right)$, $\mathcal{B}\left(\mathbf{y}_h, \boldsymbol{z}_h\right)$ and $\mathcal{B}\left(\mathbf{x}_h, \boldsymbol{\kappa}_h\right)$ are defined in equations (2.37), $\mathrm{e}\left(\boldsymbol{v}_h, \boldsymbol{v}_h, \boldsymbol{\kappa}_{\boldsymbol{v}_h}\right)$ is non-linear convection term in state equations, and $\mathrm{e}\left(\mathbf{y}_{\boldsymbol{v}_h}, \boldsymbol{v}_h, \boldsymbol{w}_h\right)$ and $\mathrm{e}\left(\boldsymbol{v}_h, \mathbf{y}_{\boldsymbol{v}_h}, \boldsymbol{w}_h\right)$ are corresponding trilinear adjoint terms.

Considering $V_h = \operatorname{span}\left\{\boldsymbol{\phi}_i\right\}_{i=1}^{\mathcal{N}_{\boldsymbol{v}}}$, $P_h = \operatorname{span}\left\{\boldsymbol{\psi}_k\right\}_{k=1}^{\mathcal{N}_p}$, and $U_h = \operatorname{span}\left\{\boldsymbol{\sigma}_l\right\}_{l=1}^{\mathcal{N}_{\boldsymbol{u}}}$, these non-linear and trilinear terms can be expanded as below:

$$\mathrm{e}\left(\boldsymbol{v}_h, \boldsymbol{v}_h, \boldsymbol{\kappa}_{\boldsymbol{v}_h}\right) = \sum_{j=1}^{\mathcal{N}_{\boldsymbol{v}}} \sum_{k=1}^{\mathcal{N}_{\boldsymbol{v}}} v_h^j v_h^k e\left(\boldsymbol{\phi}_j, \boldsymbol{\phi}_k, \boldsymbol{\phi}_i\right),$$

$$\mathrm{e}\left(\mathbf{y}_{\boldsymbol{v}_h}, \boldsymbol{v}_h, \boldsymbol{w}_h\right) = \sum_{j=1}^{\mathcal{N}_{\boldsymbol{v}}} \sum_{k=1}^{\mathcal{N}_{\boldsymbol{v}}} v_h^j w_h^k e\left(\boldsymbol{\phi}_k, \boldsymbol{\phi}_j, \boldsymbol{\phi}_i\right) \quad \text{and} \quad \mathrm{e}\left(\boldsymbol{v}_h, \mathbf{y}_{\boldsymbol{v}_h}, \boldsymbol{w}_h\right) = \sum_{j=1}^{\mathcal{N}_{\boldsymbol{v}}} \sum_{k=1}^{\mathcal{N}_{\boldsymbol{v}}} w_h^j v_h^k e\left(\boldsymbol{\phi}_k, \boldsymbol{\phi}_j, \boldsymbol{\phi}_i\right).$$

This yields the following expansion of the optimality system (2.46), similar to (2.38).

$$\begin{cases} \sum\limits_{j=1}^{\mathcal{N}_{\boldsymbol{v}}} v_h^j \mathrm{m}\left(\boldsymbol{\phi}_j, \boldsymbol{\phi}_i\right) + \sum\limits_{j=1}^{\mathcal{N}_{\boldsymbol{v}}} w_h^j \mathrm{a}\left(\boldsymbol{\phi}_j, \boldsymbol{\phi}_i\right) + \sum\limits_{j=1}^{\mathcal{N}_{\boldsymbol{v}}} \sum\limits_{k=1}^{\mathcal{N}_{\boldsymbol{v}}} v_h^j w_h^k \mathrm{e}\left(\boldsymbol{\phi}_k, \boldsymbol{\phi}_j, \boldsymbol{\phi}_i\right) + \\ \sum\limits_{j=1}^{\mathcal{N}_{\boldsymbol{v}}} \sum\limits_{k=1}^{\mathcal{N}_{\boldsymbol{v}}} w_h^j v_h^k \mathrm{e}\left(\boldsymbol{\phi}_k, \boldsymbol{\phi}_j, \boldsymbol{\phi}_i\right) + \sum\limits_{j=1}^{\mathcal{N}_p} q_h^j \mathrm{b}\left(\boldsymbol{\psi}_j, \boldsymbol{\phi}_i\right) & = \langle \mathcal{H}, \boldsymbol{\phi}_i \rangle, \\ \sum\limits_{j=1}^{\mathcal{N}_{\boldsymbol{v}}} w_h^j \mathrm{b}\left(\boldsymbol{\psi}_k, \boldsymbol{\phi}_j\right) & = 0, \\ \alpha \sum\limits_{j=1}^{\mathcal{N}_{\boldsymbol{u}}} u_h^j \mathrm{n}\left(\boldsymbol{\sigma}_j, \boldsymbol{\sigma}_l\right) + \sum\limits_{j=1}^{\mathcal{N}_{\boldsymbol{v}}} w_h^j \mathrm{c}\left(\boldsymbol{\sigma}_l, \boldsymbol{\phi}_j\right) & = 0, \\ \sum\limits_{j=1}^{\mathcal{N}_{\boldsymbol{v}}} v_h^j \mathrm{a}\left(\boldsymbol{\phi}_j, \boldsymbol{\phi}_i\right) + \sum\limits_{j=1}^{\mathcal{N}_{\boldsymbol{v}}} \sum\limits_{k=1}^{\mathcal{N}_{\boldsymbol{v}}} v_h^j v_h^k \mathrm{e}\left(\boldsymbol{\phi}_j, \boldsymbol{\phi}_k, \boldsymbol{\phi}_i\right) + \sum\limits_{j=1}^{\mathcal{N}_p} p_h^j \mathrm{b}\left(\boldsymbol{\psi}_j, \boldsymbol{\phi}_i\right) + \sum\limits_{j=1}^{\mathcal{N}_{\boldsymbol{u}}} u_h^j \mathrm{c}\left(\boldsymbol{\sigma}_j, \boldsymbol{\phi}_i\right) & = \langle \boldsymbol{f}, \boldsymbol{\phi}_i \rangle, \\ \sum\limits_{j=1}^{\mathcal{N}_{\boldsymbol{v}}} v_h^j \mathrm{b}\left(\boldsymbol{\psi}_k, \boldsymbol{\phi}_j\right) & = \langle g, \boldsymbol{\psi}_k \rangle. \end{cases} \tag{2.47}$$

Now, let us define the bijections $V_h \leftrightarrow \mathbb{R}^{\mathcal{N}_{\boldsymbol{v}}}$, $P_h \leftrightarrow \mathbb{R}^{\mathcal{N}_p}$ and $U_h \leftrightarrow \mathbb{R}^{\mathcal{N}_{\boldsymbol{u}}}$ in a similar way as before, then we can write the optimal flow control problem in following algebraic form:

Problem 2.8. *Find* $(\mathbf{v}, \mathbf{p}, \mathbf{u}, \mathbf{w}, \mathbf{q})^T \in X_h \times Z_h$*, such that,*[*]

$$\begin{bmatrix} M + \tilde{E}(\mathbf{w}) & 0 & 0 & Aad + E_{ad}(\mathbf{v}) & B_{ad} \\ 0 & 0 & 0 & B_{ad}^T & 0 \\ 0 & 0 & N & C_{ad} & 0 \\ A + E(\mathbf{v}) & B^T & C & 0 & 0 \\ B & 0 & 0 & 0 & 0 \end{bmatrix} \begin{bmatrix} \mathbf{v} \\ \mathbf{p} \\ \mathbf{u} \\ \mathbf{w} \\ \mathbf{q} \end{bmatrix} = \begin{bmatrix} \mathbf{h} \\ \mathbf{0} \\ \mathbf{0} \\ \mathbf{f} \\ \mathbf{g} \end{bmatrix}, \tag{2.48}$$

where

$$(E(\mathbf{v}))_{ij} = \sum_{k=1}^{\mathcal{N}_{\boldsymbol{v}}} v_h^k \, e(\boldsymbol{\phi}_k, \boldsymbol{\phi}_j, \boldsymbol{\phi}_i) \text{ and } \left(\tilde{E}(\mathbf{w})\right)_{ij} = \sum_{k=1}^{\mathcal{N}_{\boldsymbol{v}}} w_h^k \, e(\boldsymbol{\phi}_k, \boldsymbol{\phi}_j, \boldsymbol{\phi}_i)$$

The optimality system (2.48) is non-linear in state and owing to block structure, can be solve in one-shot through iterative numerical schemes, such as Newton method, which we will summarize in the next section.

2.5.4 Newton method

Let us write $\mathcal{K}_h = X_h \times Z_h$ and $\hat{W}_{\mathcal{N}} = (\mathbf{v}, \mathbf{p}, \mathbf{u}, \mathbf{w}, \mathbf{q})^T \in \mathcal{K}_h$. Then, Navier-Stokes constrained optimal flow control problem 2.8 reads:

Problem 2.9. *Find* $\hat{W}_{\mathcal{N}} \in \mathcal{K}_h$*, such that*

$$\mathbb{W}\left(\hat{W}_{\mathcal{N}}\right) = 0, \tag{2.49}$$

which is essentially equivalent to algebraic non-linear optimality system (2.48).

Problem 2.9 can be solved through Newton method. Thus, given an initial guess $\hat{W}_{\mathcal{N}}^0$, we tend to solve the following system at any generic $(k)^{th}$ iteration:

$$d\mathbb{W}\left(\hat{W}_{\mathcal{N}}^{k-1}\right) \delta\hat{W}_{\mathcal{N}} = -\mathbb{W}\left(\hat{W}_{\mathcal{N}}^{k-1}\right), \tag{2.50}$$

where, $\delta\hat{W}_{\mathcal{N}} = \hat{W}_{\mathcal{N}}^k - \hat{W}_{\mathcal{N}}^{k-1}$ is the increment and $d\mathbb{W}\left(\hat{W}_{\mathcal{N}}\right)$ is the Jacobian matrix.

[*]It is to be noted that the owing to $S_h \equiv Z_h$, we can take the adjoint terms, with subscript ad with the same bases functions as for the state terms. Thus, in the discussion henceforth, we will omit the subscript ad, unless the equivalence assumption between the state and adjoint spaces does not hold true.

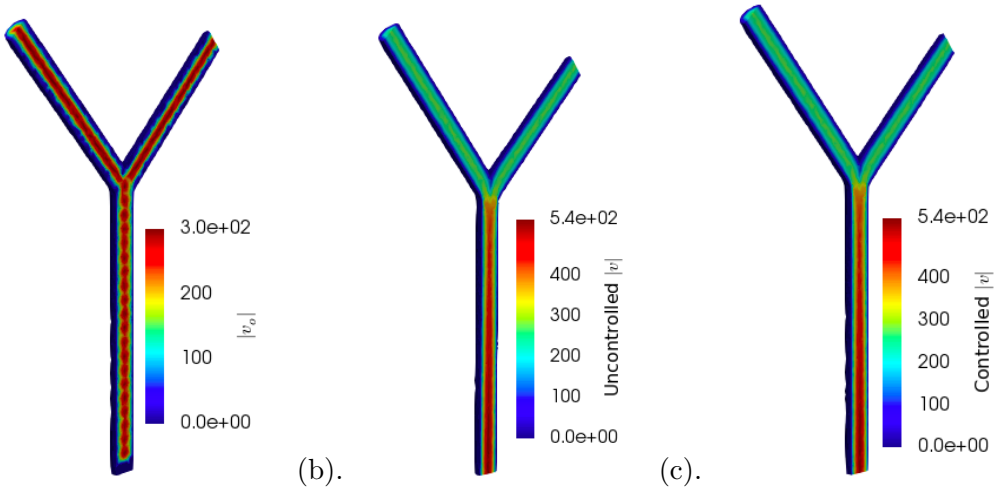

(a). (b). (c).

Figure 2.5.4: (a). Case II: desired velocity $\boldsymbol{v}_o$ (mm/s), (b). Uncontrolled velocity (mm/s), (c). Controlled velocity (mm/s).

2.5.5 Numerical results: Navier-Stokes constrained optimal flow control problem

Next, we will apply the Navier-Stokes constrained optimal flow control framework to the 3-D Y-shaped geometry, used in previous numerical example (see figure 2.5.1(a)). With the state constraints defined by equations (2.30) and the boundary conditions (2.17), we consider the problem to match $\boldsymbol{v_o}$ with $\boldsymbol{v}$ through objective functional (2.18). For the purpose, the flow at inlets is generated by $Re = 140$ and magnitude of the desired velocity is 300 mm/s (see figure 2.5.4(a)). Although chosen arbitrarily, these values fall with in the range used in modeling coronary artery flow in literature [24, 29]. We consider the following solution spaces:

$$V(\Omega) = \left[H^1_{\Gamma_{in}\cup\Gamma_w}(\Omega)\right]^3 := \left\{\boldsymbol{v} \in \left[H^1(\Omega)\right]^3 \mid \boldsymbol{v}|_{\Gamma_{in}} = \boldsymbol{v}_{in} \wedge \boldsymbol{v}|_{\Gamma_w} = \mathbf{0}\right\},$$

$$P(\Omega) = L^2(\Omega), \quad \text{and} \quad U(\Gamma_o) = \left[L^2(\Gamma_o)\right]^3.$$

We solve the optimality system (2.48), equivalently (2.50) in multiphenics [1] and report the uncontrolled and controlled velocities in figures 2.5.4(b) and 2.5.4(c), respectively. Furthermore, in this case, we have utilized $\mathbb{P}2 - \mathbb{P}1$ for state and adjoint velocity and pressure respectively, and $\mathbb{P}^1$ for the control at finite element level, thus, $\mathcal{N} = 152501$. We report the CPU time to be 371.6 seconds to develop the controlled system from the uncontrolled, reaching convergence in 6 Newton iterations (see table 2.1).

	Case I	Case II
Tetrahedral mesh size	15901	–
Degrees of freedom (dof)	225248	152501
Reynolds number	300	140
v_{const}	400 mm/s	300 mm/s
CPU time	120.7 seconds	371.6 seconds

Table 2.1: Computational details for case I: Stokes constrained optimal flow control problem and case II: Navier-Stokes constrained optimal flow control problem, applied to Y-shape geometry

2.6. Applications to patient-specific coronary artery bypass grafts

In this section, we will extend application of the optimal flow control framework to patient-specific cardiovascular geometries, reconstructed from medical images as shown in chapter 1. In these applications, we will consider Newtonian nature of blood, owing to diameter of coronary artery bypass grafts. It is well-known that blood exhibits non-Newtonian rheology, however, the non-Newtonian nature of blood is dominant in smaller vessels with diameter < 1 mm such as capillaries [38]. The coronary artery bypass grafts considered in this work have diameter in the range of 1 mm to 2.2 mm, hence, we can fairly assume that the size of blood particles such as red blood cells, white blood cells and platelets suspended in plasma, is smaller compared to the diameter of corresponding vessel itself. Thus, the viscosity will be considered constant and is low at low shear stress. In such case, Navier-Stokes equations can be considered to model blood flow [76, 41, 61, 38].

In these numerical examples, we will consider three different geometries, shown in figure 2.6.1. We will divide this section in three parts, where in the first subsection, we will consider the optimal flow control problem constrained by Stokes equations with a tracking-type objective functional. Then, in the second subsection we will apply the optimal flow control problem constrained by Navier-Stokes equations to minimize a vorticity-based objective functional in Ω_a (see figure 2.6.1(a)). The third subsection will demonstrate three three sub-cases, dealing with Navier-Stokes constrained optimal flow control problem for velocity-matching objective functional in geometries single and double grafts connections, respectively. The application of optimal flow control framework shall automatically quantify the outflow conditions, needed to minimize the vorticity or match certain desired velocity in patient-specific coronary artery bypass grafts.

2.6.1 Stokes constrained optimal flow control problem: velocity matching

In the first numerical test, we will solve Stokes constrained optimal flow control problem over domain Ω_a (see figure 2.6.1(a)), in which right internal mammary artery (RIMA)

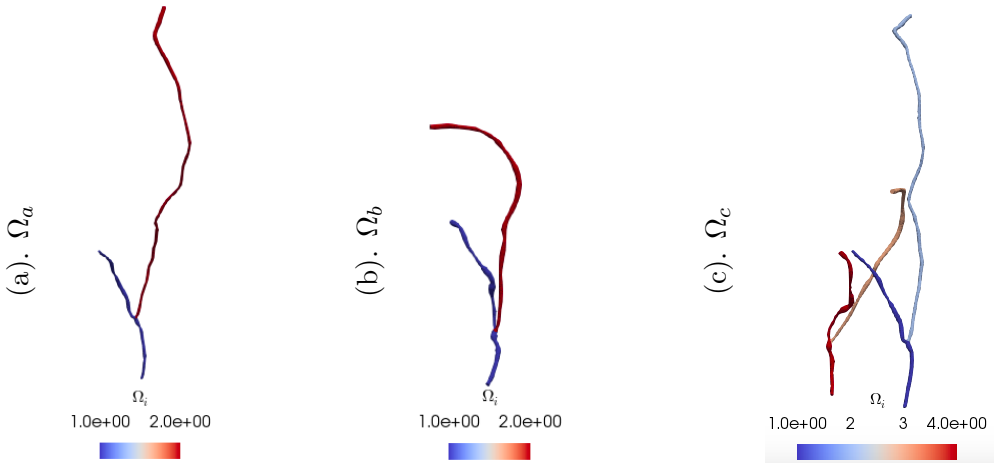

Figure 2.6.1: (a). Single graft connection: between right internal mammary artery (RIMA) (red) and stenosed left anterior descending artery (LAD) (blue). (b). Single graft connection: between saphenuous vein (SV) (red) and stenosed first obtused marginal artery (blue). (c). Two graft connections: between right internal mammary artery (light blue) and stenosed left anterior descending artery (LAD) (dark blue), and between saphenuous vein (SV) (light red) and stenosed first obtused marginal artery (OM1) (dark red).

(red) is grafted to stenosed left anterior descending artery (LAD) (blue). We mark the top openings of RIMA and LAD as the inlets, denoted by Γ_{in} and the bottom opening of LAD as the outlet, denoted by Γ_o. In this case, the boundary conditions are defined by equations (2.17), where $\boldsymbol{v}_{in}$ is Poisuille velocity defined below:

$$\boldsymbol{v}_{in} = -\frac{\eta Re}{R_{in}}\left(1 - \frac{r^2}{R_{in}^2}\right)\boldsymbol{n}_{in}. \tag{2.51}$$

Here, $Re = 80$ is Reynolds number, R_{in} is the maximum radius of an inlet, r is the distance between mesh nodes of the inlet and corresponding center, and $\boldsymbol{n}_{in}$ denotes outward normal to the inlet. The goal of this test case is to match an arbitrary desired velocity with Stokes velocity and we define this desired velocity in Ω_a through following expression:

$$\boldsymbol{v}_o = v_{const}\left(1 - \frac{r^2}{R_i^2}\right)\boldsymbol{t}_{c_i},\ i \in \{1, 2\}, \tag{2.52}$$

where R_i denotes maximum radius of a vessel, $\boldsymbol{t}_{c_i}$ denote the tangents to the points of centerline of a vessel, in the axial direction and r is the distance between mesh nodes and nearest point on the centerline of a vessel. Moreover, we consider $v_{const} = 350\ mm/s$.

The mathematical problem is given by problem 2.3. At the continuous level, we consider

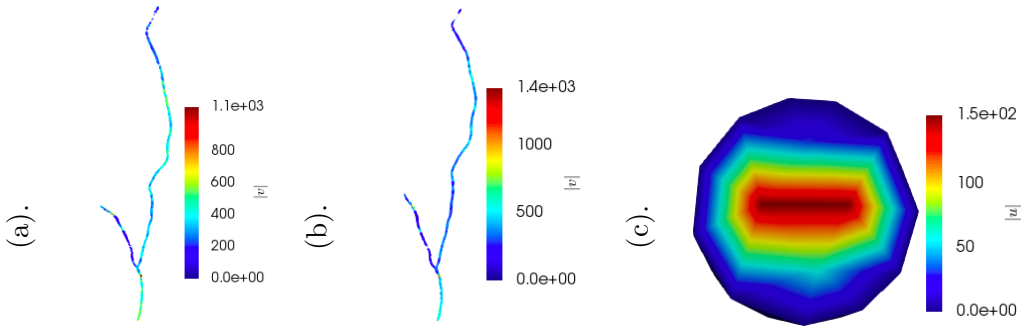

Figure 2.6.2: (a). Uncontrolled state velocity (mm/s), (b). Controlled state velocity (mm/s), (c). Boundary control (mm^2/s^2).

the following Hilbert spaces for velocity, pressure and control respectively:

$$V(\Omega_a) = H^1_{\Gamma_{in}\cup\Gamma_w}(\Omega_a) = \left[\boldsymbol{v} \in \left[H^1(\Omega_a)\right]^3 : \boldsymbol{v}|_{\Gamma_{in}} = \boldsymbol{v_{in}} \text{ and } \boldsymbol{v}|_{\Gamma_w} = \mathbf{0}\right],$$

$$P(\Omega_a) = L^2(\Omega_a), \text{ and } \quad U(\Gamma_o) = \left[L^2(\Gamma_o)\right]^3.$$

We solve the coupled discretized optimality system in multiphenics [1] and report the uncontrolled and controlled state velocities, and control in figures 2.6.2(a), 2.6.2(b) and 2.6.2(c) respectively. In this case, the degrees of freedom are $\mathcal{N} = 639448$ and the CPU time taken is 254 seconds. We remark that at the discretized level, we have solved the problem with $S_h = \mathbb{P}2-\mathbb{P}1 \equiv Z_h$ and therefore, at this level both Brezzi's inf-sup condition and LBB inf-sup condition are satisfied.

2.6.2 Navier-Stokes constrained optimal flow control problem: vorticity minimization

In the second numerical example, we will demonstrate Galerkin finite element approximation of a vorticity minimization problem with Navier-Stokes state constraints, defined over Ω_a (see figure 2.6.1(a)). The purpose of this test case is to illustrate the order of reduction achieved for the objective functional through the proposed one-shot optimal flow control methodology, in patient-specific geometrical models of cardiovascular system. From a clinical perspective, anomalous flow in coronary artery bypass grafts can be induced by high vorticity or dissipation regions. Therefore, when also considering boundary layers in the cardiovascular problem, vorticity minimization can be of interest to propose an optimal graft designs [67].

Thus, we consider the following objective functional, comprising of a vorticity mini-

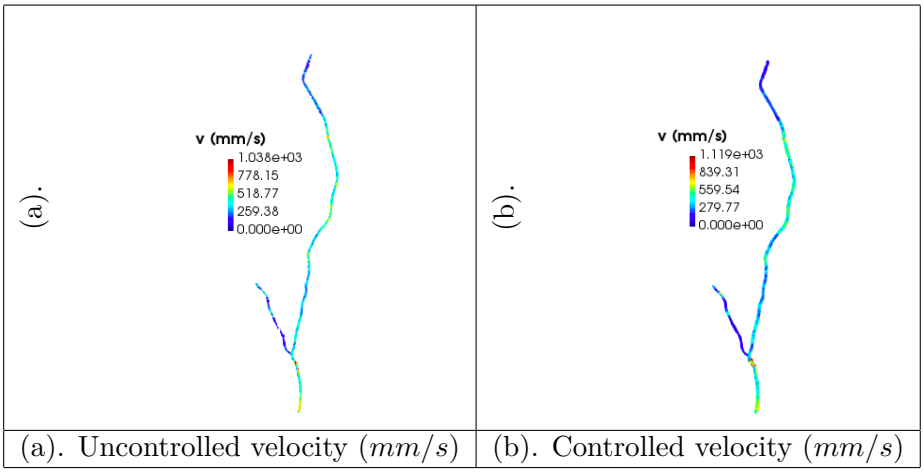

(a). Uncontrolled velocity (mm/s) | (b). Controlled velocity (mm/s)

Figure 2.6.3: State velocity $\boldsymbol{v}$ (mm/s) approximations for vorticity minimization problem.

mization term and a control term,

$$\mathcal{J}(\boldsymbol{v},\boldsymbol{u}) = \frac{1}{2}\int_{\Omega_a} |\nabla\times\boldsymbol{v}|^2 d\Omega + \frac{\alpha}{2}\int_{\Gamma_o} |\boldsymbol{u}|^2 d\Gamma_o, \tag{2.53}$$

and we define the optimal flow control problem as below:

Problem 2.10. *Find* $(\boldsymbol{v},p,\boldsymbol{u}) \in V\times P\times U$ *such that* (2.53) *is minimized subject to equations* (2.30) *and* (2.17).

At the continuous level, we consider the solution spaces defined in the previous section and the inflow velocity defined by equation (2.51). The non-linear discretized optimality system is given by (2.47), where,

$$\mathrm{m}(\boldsymbol{s},(\mathbf{y}_{\boldsymbol{v}},\mathbf{y}_p)) = \frac{1}{2}\int_{\Omega}(\nabla\times\boldsymbol{v})\cdot(\nabla\times\mathbf{y}_{\boldsymbol{v}}), \quad \text{and} \quad \mathrm{m}(\boldsymbol{s}_o,\mathbf{y}_{\boldsymbol{s}}) = 0.$$

Considering $\mathbb{P}2-\mathbb{P}1$ pair for velocity and pressure, and $\mathbb{P}1$ for control, Galerkin finite element method attains $\mathcal{N} = 433195$ degrees of freedom. The uncontrolled objective functional is 287484477.44 and is decreased to 287483300.44. We show the uncontrolled and controlled velocities in figures 2.6.3(a) and 2.6.3(b) respectively. Furthermore, computational time of 1144.87 seconds is taken to solve an uncontrolled problem (that is, for $\boldsymbol{u}=0$) and to develop controlled solution from it by solving system (2.48).

2.6.3 Navier-Stokes constrained optimal flow control problem: velocity matching

In the next numerical examples, we will apply the Navier-Stokes optimal flow control framework with tracking-type objective functional. We will consider three different geometries,

shown in figure 2.6.1. Assume $\boldsymbol{v}_o$ to be physiological data extracted from 4D-flow MRIs [33], then, the idea is to implement the numerical optimal flow control framework to match this data in corresponding patient-specific geometries and automatically quantify required boundary conditions, specifically outflow conditions. For the sake of simplicity, we have relied on Neumann boundary conditions in this work and the numerical tests henceforth are proof of concept of the proposed idea.

Case I(a): single graft connection between RIMA and LAD

In the first case, we consider domain Ω_a (figure 2.6.1(a)) in which graft connection is between right internal mammary artery (RIMA) and stenosed left anterior descending artery (LAD). The saddle-point optimal flow control problem is defined in problem 2.5. We define $\boldsymbol{v}_{in}$ at inlets by equation (2.5), where, $Re = 80$. Furthermore, we consider the same solution spaces at the continuous as before, that is,

$$V(\Omega_a) = H^1_{\Gamma_{in}\cup\Gamma_w}(\Omega_a) = \left[\boldsymbol{v} \in \left[H^1(\Omega_a)\right]^3 : \boldsymbol{v}|_{\Gamma_{in}} = \boldsymbol{v_{in}} \text{ and } \boldsymbol{v}|_{\Gamma_w} = \boldsymbol{0}\right],$$

$$P(\Omega_a) = L^2(\Omega_a), \text{ and } \quad U(\Gamma_o) = \left[L^2(\Gamma_o)\right]^3$$

and with $v_{const} = 350$ in equation (2.52), we consider the observation velocity $\boldsymbol{v}_o \in \left[L^2(\Omega_a)\right]^3$. We solve the full order problem using $\mathbb{P}2-\mathbb{P}1$ for velocity and pressure and $\mathbb{P}2$ for control and attain $\mathcal{N} = 433288$ degrees of freedom. Furthermore, one such simulation requires 1213.3 seconds. The uncontrolled and controlled velocities and control magnitude are shown in figure 2.6.4(case I(a))(a), (case I(a))(b) and (case I(a))(c), respectively. Furthermore, the fractional flow reserve (FFR), that is pressure drop over the stenosis, is measured to be 0.18.

Case I(b): single graft connection between SV and OM1

In the second case, we will apply Navier-Stokes constrained optimal flow control problem to another coronary artery bypass graft geometry. In this case, we label the computational domain by Ω_b and take it to be saphenuous vein grafted to stenosed first obtuse marginal artery (OM1) (figure 2.6.1(b)). Moreover, we consider the velocity $\boldsymbol{v}_{in}$ to be generated by $Re = 50$ at Γ_{in}, through equation (2.51) and observation velocity to be distributed across Ω_b by equation (2.52) with $v_{const} = 350\ mm/s$. The solution spaces in this case remain the same as case I(a), while being considered over Ω_b and we utilize $\mathbb{P}2-\mathbb{P}1-\mathbb{P}2$ for velocity, pressure and control respectively in multiphenics [1] to solve the problem 2.8. In this case, we report Galerkin finite element degrees of freedom ($\mathcal{N}$) to be 280274 and the computational time to be 634 seconds. The uncontrolled and controlled velocities and boundary control are shown in (case I(b))(a), (case I(b))(b) and (case I(b))(c), respectively, of figure 2.6.4. The pressure drop over the stenosis in this case is measured to be 0.26.

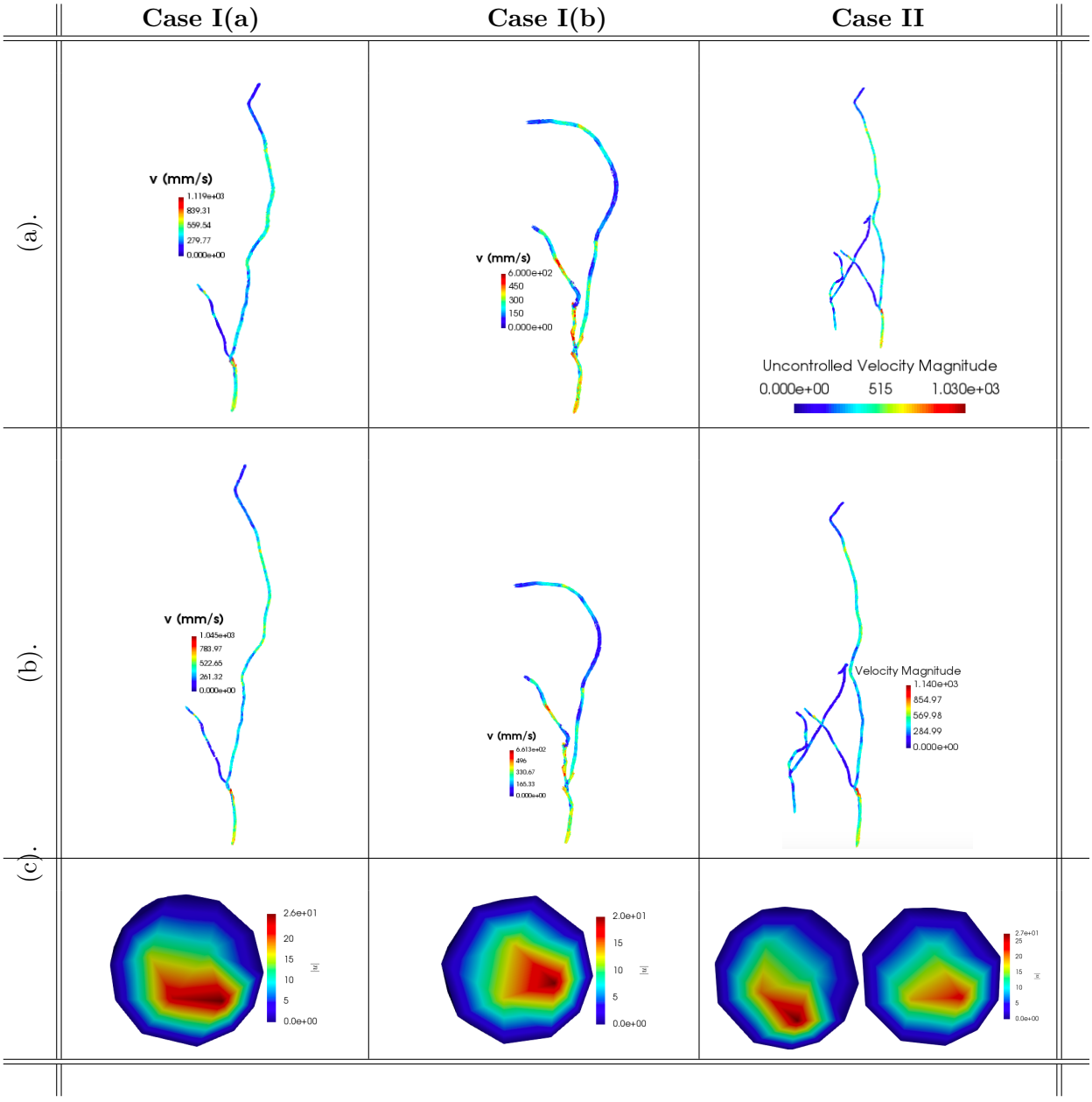

Figure 2.6.4: (a). Uncontrolled velocity (mm/s) (b). Controlled velocity (mm/s). (c). Boundary control (mm^2/s^2).

Case II: two grafts connections

We further apply the reduced order optimal flow control framework to Ω_c (see figure 2.6.1(c)) comprising of two grafts connected to two separate stenosed arteries. It is to be noted that $\Omega_c = \Omega_a \cup \Omega_b$ and mathematical problem is similat as considered for single graft connections, with the number of inlets and outlets doubled. We label the inlets of right internal mammary artery (RIMA) and left anterior descending artery (LAD) as Γ_{in_1} and the inlets of saphenuous vein (SV) and first obtuse marginal artery (OM1) as Γ_{in_2}. Similarly respective outlets are marked as Γ_{o_1} and Γ_{o_2}. In this case, we consider the following boundary conditions:

$$\begin{cases} \boldsymbol{v} = \boldsymbol{v}_{in_1}, & \text{on } \Gamma_{in_1}, \\ \boldsymbol{v} = \boldsymbol{v}_{in_2}, & \text{on } \Gamma_{in_2}, \\ \boldsymbol{v} = \boldsymbol{0}, & \text{on } \Gamma_{w}, \\ -\eta\left(\nabla \boldsymbol{v}\right)\boldsymbol{n} + p\boldsymbol{n} = \boldsymbol{u}, & \text{on } \Gamma_{o_1} \cup \Gamma_{o_2}, \end{cases} \tag{2.54}$$

where,

$$\boldsymbol{v_{in}}_1\left(\boldsymbol{\mu}_1\right) = -\frac{\eta Re_1}{R_{in_1}}\left(1 - \frac{r^2}{R_{in_1}^2}\right)\boldsymbol{n}_{in_1}, \qquad \boldsymbol{v_{in}}_2\left(\boldsymbol{\mu}_2\right) = -\frac{\eta Re_2}{R_{in_2}}\left(1 - \frac{r^2}{R_{in_2}^2}\right)\boldsymbol{n}_{in_2}.$$

Furthermore, we consider $Re_1 = 80$ and $Re_2 = 50$, and the following solution spaces for velocity, pressure and control respectively:

$$V\left(\Omega_c\right) = H^1_{\Gamma_{in_1}\cup\Gamma_{in_2}\cup\Gamma_w}\left(\Omega_c\right) = \left[\boldsymbol{v} \in \left[H^1\left(\Omega_c\right)\right]^3 : \boldsymbol{v}|_{\Gamma_{in_1}} = \boldsymbol{v_{in}}1,\ \boldsymbol{v}|_{\Gamma_{in_2}} = \boldsymbol{v_{in}}2 \text{ and } \boldsymbol{v}|_{\Gamma_w} = \boldsymbol{0}\right],$$

and

$$P\left(\Omega_c\right) = L^2\left(\Omega_c\right), \quad \text{and} \quad U\left(\Gamma_{o_1} \cup \Gamma_{o_2}\right) = \left[L^2\left(\Gamma_{o_1} \cup \Gamma_{o_2}\right)\right]^3.$$

The desired velocity in this case is $\boldsymbol{v}_o \in \left[L^2\left(\Omega_c\right)\right]^3$, with $v_{const} = 350\ mm/s$. In this test problem, we consider $\mathbb{P}2 - \mathbb{P}1$ for state and adjoint velocity and pressure and $\mathbb{P}2$ for control, attaining $\mathcal{N} = 715462$. The CPU time taken to solve this problem in multiphenics is 1848.13 seconds and the uncontrolled and controlled velocities together with control are shown in case II (a), case II (b) and case II (c) in figure 2.6.4. The control in this case is the energy per unit length for both outlets Γ_{o_1} (shown on left side in the figure 2.6.4 (case II(c))) and Γ_{o_2} (shown on right side in the figure 2.6.4 (case II(c))). Moreover, we report the computational details for all three cases with application of Navier-Stokes constrained optimal flow control problem with velocity matching objective in table 2.2. Furthermore, we remark that in these three numerical tests, we have satisfied Brezzi's inf-sup conditon and LBB inf-sup condition at the numerical level by utilizing $S_h = \mathbb{P}2 - \mathbb{P}1 \equiv Z_h$.

	Case I(a)	Case I(b)	Case II
Tetrahedral mesh size	42354	27398	605451
Degrees of freedom (dof)	433288	280274	715462
Reynolds number	80	50	$(80, 50)$
v_{const}	350 mm/s	350 mm/s	350 mm/s
CPU time	1214.3 seconds	634 seconds	1848.13 seconds

Table 2.2: Computational details for case I(a), case I(b) and case II.

Concluding remarks

In this chapter, we have introduced the general optimal flow control problems and the derivative-based optimization algorithms, implemented for their solution. We summarize the chapter as below:

(i) We have seen that the general optimal flow control problems can be put in a coupled system, known as Karush-Kuhn-Tucker optimality system, making the solution appraoch to be more direct and easier.

(ii) The saddle-point derivation of KKT optimality system comprises of two nested saddle-point problems, where one is the primal saddle-point problem and the other comprises its combination with the adjoint and optimality equations. The problem structure arising from this formulation is block form, rendering it easier to view the problem in algebraic structure.

(iii) To ensure the existence of a unique solution to the quadratic optimal flow control problem constrained by Stokes or Navier-Stokes equations, we need to satisfy the assumptions made in Brezzi's theorem and LBB inf-sup condition.

(iv) Our solution approach has been *optimize-then-discretize*, where we tend to first cast the problem in KKT optimality system and then solve it using Galerkin finite element methods. We have shown some preliminary results in this regard and we remark that the accuracy of such methods rely on the degrees of freedom and hence on the discretization size h. The finite element degrees of freedom can be very large for larger mesh sizes, as has been shown in sections 2.5.2, 2.5.5 and 2.6. Hence, the computational cost can be relatively higher, as we have shown that using stable finite element spaces, we need to spend at least $\mathcal{O}\left(10^2\right)$ seconds of CPU time. This computational time can be considered unbearable when dealing with parametrized problems, where simulations are performed in repetitive environment.

(v) Lastly, we remark that in the last section, we have applied the optimal flow control framework to patient-specific coronary artery bypass grafts and have verifiably shown

that through this framework, we can minimize the difference between physiological measurements and numerical measurements and can quantify the outflow boundary conditions needed for this purpose.

Extracting from (iv) and (v), we remark that in patient-specific computational hemodynamics modeling, one has to consider many-query scenarios, which are modeled by some parameters and in such cases, the simulations are needed to be carried out in a repetitive environment. Such real-life applications require sufficiently fine mesh size, as has been shown in section 2.6, thus the computational cost of $\mathcal{O}\left(10^2\right)$ might be acceptable for one simulation but it is very high for the repeated simulations. Therefore, implementation of the high-order numerical methods such as Galerkin finite element methods only is not sufficient in real-life applications and inevitably, one needs to construct numerical methods that can lower the computational cost while retaining the accuracy of high-order numerical methods. We will focus on this part in the next chapter.

Chapter 3

Reduced order methods for parametrized optimal flow control problems

***

In this chapter, we will combine the numerical pipeline for optimal flow control problems constrained by Stokes and Navier-Stokes equations, discussed in chapter 2, with reduced order methods in parametrized settings. The framework will be constructed with applications in patient-specific computational hemodynamics modeling in mind, with the aim to match clinical measurements through numerical simulations and automated quantification of outflow boundary conditions for the purpose. Such real-life applications require to take into consideration different scenarios, modeled by tuning some parameters, for example, one can study the effect on blood flow pattern corresponding to different viscosity or inlet flow velocity scenarios, or different flow rates or pressure drop, etc. by tuning the Reynolds number or one can also consider different shape parameters, such as angle of the bypass grafts leading to different grafts designs. Some work in the latter direction can be found in [3, 4, 90, 18, 17].

Numerical methods approximate the solutions to such problems with reliable accuracy, as we have shown in chapter 2, section 2.6, however, the computational cost of these methods depends upon the discretization size, which needs to be sufficiently large to achieve

accurate solution in real-life applications, specifically in cardiovascular applications. In parametrized settings, the computations are performed in repetitive environment, hence the computational cost is usually very large. Thus, the goal of this chapter is to combine the parametrized numerical framework with projection-based reduced order methods that cast the high-order numerical solution manifold onto a low-dimensional manifold, where one can explore the solution for different tunings of the parameters, in an inexpensive and reliable manner.

This chapter is arranged in the following order: in the first section we will introduce the parametrized version of Stokes constrained optimal flow control problems and will further show the construction of reduced order framework, based upon proper orthogonal decomposition (POD) and Galerkin projection. The second section will demonstrate preliminary numerical results for the application of the reduced order framework on the idealized Y-shaped geometry. The reduced order framework will then be extended to parametrized Navier-Stokes constrained optimal flow control problems in the third section and finally we will demonstrate some corresponding preliminary numerical results. In the next chapter, we will show application of the reduced order frameworks for both Stokes and Navier-Stokes constrained optimal flow control problems in patient-specific cardiovascular modeling.

3.1. Parametrized Stokes constrained optimal flow control problem

In the first section, we will introduce the parametrized version of optimal flow control problems constrained by Stokes equations, discussed in chapter 2, section 2.4.1. For details, we refer the reader to aforementioned section and here, we will give a general summary of the problem. For the purpose, let us consider a $d-$vector of parameters and denote it by $\mathcal{D} \subset \mathbb{R}^d, d \in \mathbb{N}$, such that the physical and/or geometrical parameters $\boldsymbol{\mu} \in \mathcal{D}$. Furthermore, we consider a domain $\Omega \subset \mathbb{R}^3$, with Lipschitz boundary $\partial\Omega = \Gamma_{in} \cup \Gamma_w \cup \Gamma_o$, where Γ_{in} denotes the inlet boundary, Γ_w represents the lateral walls and Γ_o stands for outlets. We remark that in general Ω can be parametrized, that is, $\Omega = \Omega(\boldsymbol{\mu})$ (see for example, [8, 19, 81, 82, 88, 49, 99]), however, for simplicity sake, specifically in applications to patient-specific cardiovascular geometries, we are considering fixed Ω. Then, the parametrized Stokes constrained optimal flow control problem reads:

Problem 3.1. *Given $\boldsymbol{\mu} \in \mathcal{D}$, find $(\boldsymbol{s}(\boldsymbol{\mu}), \boldsymbol{u}(\boldsymbol{\mu})) \in S \times U$ such that*

$$\mathcal{J}(\boldsymbol{s}, \boldsymbol{u}; \boldsymbol{\mu}) = \frac{1}{2}\|\boldsymbol{s}(\boldsymbol{\mu}) - \boldsymbol{s}_o\|^2_{Q(\Omega)} + \frac{\alpha}{2}\|\boldsymbol{u}(\boldsymbol{\mu})\|^2_{U(\Gamma_o)}, \tag{3.1}$$

is minimized subject to,

$$\begin{cases} -\eta\Delta\boldsymbol{v}\left(\boldsymbol{\mu}\right)+\nabla p\left(\boldsymbol{\mu}\right)=\boldsymbol{f}\left(\boldsymbol{\mu}\right), & \text{in } \Omega, \\ \nabla\cdot\boldsymbol{v}\left(\boldsymbol{\mu}\right)=g\left(\boldsymbol{\mu}\right), & \text{in } \Omega, \\ \boldsymbol{v}\left(\boldsymbol{\mu}\right)=\boldsymbol{v}_{in}\left(\boldsymbol{\mu}\right), & \text{on } \Gamma_{in}, \\ \boldsymbol{v}\left(\boldsymbol{\mu}\right)=\mathbf{0}, & \text{on } \Gamma_{w}, \\ -\eta\left(\nabla\boldsymbol{v}\left(\boldsymbol{\mu}\right)\right)\boldsymbol{n}+p\left(\boldsymbol{\mu}\right)\boldsymbol{n}=\boldsymbol{u}\left(\boldsymbol{\mu}\right), & \text{on } \Gamma_{o}. \end{cases} \tag{3.2}$$

Here, $\boldsymbol{s}=(\boldsymbol{v},p)$ denotes state variables, that are velocity and pressure, and $\boldsymbol{u}$ denotes the control variables. Moreover, the state and control spaces are denoted by $S\left(\Omega\right)=V\left(\Omega\right)\times P\left(\Omega\right)$ and $U\left(\Gamma_o\right)$ respectively, $\boldsymbol{f}$ are the body forces, $\nabla\cdot\boldsymbol{v}$ is the divergence operator, $\eta>0$ is the kinematic viscosity and $\boldsymbol{s}_o\in Q\supseteq S$ is the state desired to be observed or presumably known state data, desired to be matched. Moreover, $\mathcal{J}$ is the tracking-type objective functional.
Now, the parametrized state equations (3.2) can be written in weak form as below:

$$\begin{cases} \mathrm{a}\left(\boldsymbol{v}\left(\boldsymbol{\mu}\right),\boldsymbol{w};\boldsymbol{\mu}\right)+\mathrm{b}\left(p\left(\boldsymbol{\mu}\right),\boldsymbol{w};\boldsymbol{\mu}\right)+\mathrm{c}\left(\boldsymbol{u}\left(\boldsymbol{\mu}\right),\boldsymbol{w};\boldsymbol{\mu}\right)=\left\langle\boldsymbol{f}\left(\boldsymbol{\mu}\right),\boldsymbol{w}\right\rangle, & \forall\ \boldsymbol{w}\in V, \\ \mathrm{b}\left(q,\boldsymbol{v}\left(\boldsymbol{\mu}\right);\boldsymbol{\mu}\right)=\left\langle g\left(\boldsymbol{\mu}\right),q\right\rangle, & \forall\ q\in P, \end{cases} \tag{3.3}$$

where,

$$\mathrm{a}\left(\boldsymbol{v},\boldsymbol{w};\boldsymbol{\mu}\right):=\eta\int_{\Omega}\nabla\boldsymbol{v}\cdot\nabla\boldsymbol{w}\ d\Omega,\qquad \mathrm{b}\left(q,\boldsymbol{v};\boldsymbol{\mu}\right):=-\int_{\Omega}q\left(\nabla\cdot\boldsymbol{v}\right)\ d\Omega, \tag{3.4}$$

and

$$\mathrm{c}\left(\boldsymbol{u},\boldsymbol{w};\boldsymbol{\mu}\right):=-\int_{\Gamma_o}\boldsymbol{u}\cdot\boldsymbol{w}\ d\Gamma_o. \tag{3.5}$$

We consider the adjoint spaces $Z=Z_{\boldsymbol{v}}\times Z_p$ such that $\boldsymbol{z}=(\boldsymbol{w},q)\in Z$ are the adjoint variables and $S\equiv Z$. Then, taking $X=S\times U$, the parametrized version of the saddle point problem 2.4 can be written as:

Problem 3.2. *Given $\boldsymbol{\mu}\in\mathcal{D}$, find $\left(\mathbf{x}\left(\boldsymbol{\mu}\right),\boldsymbol{z}\left(\boldsymbol{\mu}\right)\right)\in X\times S$ such that,*

$$\begin{cases} \mathcal{A}\left(\mathbf{x}\left(\boldsymbol{\mu}\right),\mathbf{y};\boldsymbol{\mu}\right)+\mathcal{B}\left(\boldsymbol{z}\left(\boldsymbol{\mu}\right),\mathbf{y};\boldsymbol{\mu}\right)=\left\langle\mathcal{H}\left(\boldsymbol{\mu}\right),\mathbf{y}\right\rangle, & \forall\ \mathbf{y}\in X, \\ \mathcal{B}\left(\mathbf{x}\left(\boldsymbol{\mu}\right),\boldsymbol{\kappa};\boldsymbol{\mu}\right)=\left\langle\mathcal{G}\left(\boldsymbol{\mu}\right),\boldsymbol{\kappa}\right\rangle, & \forall\ \boldsymbol{\kappa}\in Z, \end{cases} \tag{3.6}$$

where, for all $\mathbf{y}=\left(\mathbf{y}_{\boldsymbol{s}}=\left(\mathbf{y}_{\boldsymbol{v}},\mathbf{y}_p\right),\mathbf{y}_{\boldsymbol{u}}\right)\in X$ and for all $\boldsymbol{\kappa}=\left(\boldsymbol{\kappa}_{\boldsymbol{w}},\boldsymbol{\kappa}_q\right)\in Z$,

$$\begin{cases} \mathcal{A}\left(\mathbf{x},\mathbf{y};\boldsymbol{\mu}\right)=\mathrm{m}\left(\boldsymbol{s},\mathbf{y}_{\boldsymbol{s}};\boldsymbol{\mu}\right)+\alpha\mathrm{n}\left(\boldsymbol{u},\mathbf{y}_{\boldsymbol{u}};\boldsymbol{\mu}\right), \\ \mathcal{B}\left(\boldsymbol{z},\mathbf{y};\boldsymbol{\mu}\right)=\mathrm{a}\left(\mathbf{y}_{\boldsymbol{v}},\boldsymbol{w};\boldsymbol{\mu}\right)+\mathrm{b}\left(\mathbf{y}_p,\boldsymbol{w};\boldsymbol{\mu}\right)+\mathrm{c}\left(\mathbf{y}_{\boldsymbol{u}},\boldsymbol{w};\boldsymbol{\mu}\right)+\mathrm{b}\left(q,\mathbf{y}_{\boldsymbol{v}};\boldsymbol{\mu}\right), \\ \mathcal{B}\left(\mathbf{x},\boldsymbol{\kappa};\boldsymbol{\mu}\right)=\mathrm{a}\left(\boldsymbol{v},\boldsymbol{\kappa}_{\boldsymbol{w}};\boldsymbol{\mu}\right)+\mathrm{b}\left(p,\boldsymbol{\kappa}_{\boldsymbol{w}};\boldsymbol{\mu}\right)+\mathrm{c}\left(\boldsymbol{u},\boldsymbol{\kappa}_{\boldsymbol{w}};\boldsymbol{\mu}\right)+\mathrm{b}\left(\boldsymbol{\kappa}_q,\boldsymbol{v};\boldsymbol{\mu}\right), \end{cases}$$

and

$$\left\langle\mathcal{H}\left(\boldsymbol{\mu}\right),\mathbf{y}\right\rangle=\mathrm{m}\left(\boldsymbol{s}_o\left(\boldsymbol{\mu}\right),\mathbf{y}_{\boldsymbol{s}}\right),\quad \left\langle\mathcal{G}\left(\boldsymbol{\mu}\right),\boldsymbol{\kappa}\right\rangle=\left\langle\boldsymbol{f}\left(\boldsymbol{\mu}\right)+g\left(\boldsymbol{\mu}\right),\boldsymbol{\kappa}\right\rangle.$$

Here, $\mathrm{m} : V \times V \to \mathbb{R}$ and $\mathrm{n} : U \times U \to \mathbb{R}$ are the bilinear forms associated to objective functional (3.1) and are defined as:

$$\mathrm{m}\left(\boldsymbol{s}\left(\boldsymbol{\mu}\right) - \boldsymbol{s}_o, \mathbf{y}_{\boldsymbol{s}} - \boldsymbol{s}_o; \boldsymbol{\mu}\right) := \left(\boldsymbol{s}\left(\boldsymbol{\mu}\right) - \boldsymbol{s}_o, \mathbf{y}_{\boldsymbol{s}} - \boldsymbol{s}_o\right)_{V(\Omega)} \text{ and } \mathrm{n}\left(\boldsymbol{u}\left(\boldsymbol{\mu}\right), \mathbf{y}_{\boldsymbol{u}}; \boldsymbol{\mu}\right) := \left(\boldsymbol{u}\left(\boldsymbol{\mu}\right), \mathbf{y}_{\boldsymbol{u}}\right)_{U(\Gamma_o)}$$

Furthermore, we recall that a unique solution to the saddle-point problem 3.2 will exist if following assumptions of Brezzi's theorem hold true:

Theorem 3.1 (Brezzi's theorem)**.** *A unique solution to the saddle-point problem 3.2 will exist if the following conditions are satisfied,*

(i) $\mathcal{A} : X \times X \to \mathbb{R}$ *is continuous and satisfies,*

$$\exists\ a_0 > 0,\ \textit{such that} \inf_{\mathbf{x}\setminus\{0\}\in X_0} \frac{\mathcal{A}\left(\mathbf{x}, \mathbf{x}; \boldsymbol{\mu}\right)}{\|\mathbf{x}\|_X^2} \geq a_0,\ \forall\ \boldsymbol{\mu} \in \mathcal{D},$$

where, $X_0 = \{\mathbf{x} \in X\ \textit{such that}\ \mathcal{B}\left(\mathbf{x}, \boldsymbol{\kappa}; \boldsymbol{\mu}\right) = 0\ \forall\ \boldsymbol{\kappa} \in Z\}$.

(ii) $\mathcal{B} : X \times Z \to \mathbb{R}$ *is continuous and satisfies the following inf-sup condition,*

$$\exists\ b_0 > 0,\ \textit{such that} \inf_{\boldsymbol{z}\setminus\{0\}\in Z} \sup_{\mathbf{x}\setminus\{0\}\in X} \frac{\mathcal{B}\left(\mathbf{x}, \boldsymbol{z}; \boldsymbol{\mu}\right)}{\|\mathbf{x}\|_X \|\boldsymbol{z}\|_Z} \geq b_0,\ \forall\ \boldsymbol{\mu} \in \mathcal{D}.$$

The theorem can be proven in a very similar way as before, (see the proof of therorem 2.6 in section 2.4.1 for details), specifically the inf-sup condition will be satisfied if $S \equiv Z$.

Truth approximations

We will summarize the parametrized version of Galerkin finite element approximations of Stokes constrained optimal flow control problems, discussed in chapter 2, section 2.5.1. These numerical approximations of the continuous problem will serve as building blocks in the construction of reduced order spaces, discussed in next section, where we will refer to these solutions as *truth* solutions or high-fidelity solutions. Let us consider the discretization $\mathcal{T}_h,\ 0 < h \in \mathbb{R}^+ < \infty$ of Ω and the corresponding finite element spaces $X_h = (V_h \times P_h \times U_h) \subset X$ and $Z_h \subset Z$ such that $S_h = (V_h \times P_h) \equiv Z_h$, then the discrete counter part of the problem 3.2 reads:

Problem 3.3. *Given* $\boldsymbol{\mu} \in \mathcal{D}$*, find* $\left(\mathbf{x}_h\left(\boldsymbol{\mu}\right), \boldsymbol{z}_h\left(\boldsymbol{\mu}\right)\right) \in X_h \times Z_h$ *such that,*

$$\begin{cases} \mathcal{A}\left(\mathbf{x}_h\left(\boldsymbol{\mu}\right), \mathbf{y}_h; \boldsymbol{\mu}\right) + \mathcal{B}\left(\boldsymbol{z}_h\left(\boldsymbol{\mu}\right), \mathbf{y}_h; \boldsymbol{\mu}\right) = \left\langle \mathcal{H}\left(\boldsymbol{\mu}\right), \mathbf{y}_h \right\rangle, & \forall\ \mathbf{y}_h \in X_h, \\ \mathcal{B}\left(\mathbf{x}_h\left(\boldsymbol{\mu}\right), \boldsymbol{\kappa}_h; \boldsymbol{\mu}\right) = \left\langle \mathcal{G}\left(\boldsymbol{\mu}\right), \boldsymbol{\kappa}_h \right\rangle, & \forall\ \boldsymbol{\kappa}_h \in Z_h, \end{cases} \tag{3.7}$$

where, for all $\mathbf{y}_h = \left(\mathbf{y}_{\boldsymbol{s}_h} = \left(\mathbf{y}_{\boldsymbol{v}_h}, \mathbf{y}_{p_h}\right), \mathbf{y}_{\boldsymbol{u}_h}\right) \in X_h$ *and for all* $\boldsymbol{\kappa}_h = \left(\boldsymbol{\kappa}_{\boldsymbol{w}_h}, \boldsymbol{\kappa}_{q_h}\right) \in Z_h$*,*

$$\begin{cases} \mathcal{A}\left(\mathbf{x}_h, \mathbf{y}_h; \boldsymbol{\mu}\right) = \mathrm{m}\left(\boldsymbol{s}_h, \mathbf{y}_{\boldsymbol{s}_h}; \boldsymbol{\mu}\right) + \alpha \mathrm{n}\left(\boldsymbol{u}_{\boldsymbol{h}}, \mathbf{y}_{\boldsymbol{u}_h}; \boldsymbol{\mu}\right), \\ \mathcal{B}\left(\boldsymbol{z}_h, \mathbf{y}_h; \boldsymbol{\mu}\right) = \mathrm{a}\left(\mathbf{y}_{\boldsymbol{v}_h}, \boldsymbol{w}_h; \boldsymbol{\mu}\right) + \mathrm{b}\left(\mathbf{y}_{p_h}, \boldsymbol{w}_h; \boldsymbol{\mu}\right) + \mathrm{c}\left(\mathbf{y}_{\boldsymbol{u}_h}, \boldsymbol{w}_h; \boldsymbol{\mu}\right) + \mathrm{b}\left(q_h, \mathbf{y}_{\boldsymbol{v}_h}; \boldsymbol{\mu}\right), \\ \mathcal{B}\left(\mathbf{x}_h, \boldsymbol{\kappa}_h; \boldsymbol{\mu}\right) = \mathrm{a}\left(\boldsymbol{v}_{\boldsymbol{h}}, \boldsymbol{\kappa}_{\boldsymbol{w}_h}; \boldsymbol{\mu}\right) + \mathrm{b}\left(p_h, \boldsymbol{\kappa}_{\boldsymbol{w}_h}; \boldsymbol{\mu}\right) + \mathrm{c}\left(\boldsymbol{u}_h, \boldsymbol{\kappa}_{\boldsymbol{w}_h}; \boldsymbol{\mu}\right) + \mathrm{b}\left(\boldsymbol{\kappa}_{q_h}, \boldsymbol{v}_h; \boldsymbol{\mu}\right). \end{cases}$$

With

$$\boldsymbol{v}_h = \sum_{j=1}^{\mathcal{N}_{\boldsymbol{v}}} v_h^j \boldsymbol{\phi}_j \in V_h, \quad p_h = \sum_{j=1}^{\mathcal{N}_p} p_h^j \psi_j \in P_h, \qquad \boldsymbol{u}_h = \sum_{j=1}^{\mathcal{N}_{\boldsymbol{u}}} u_h^j \boldsymbol{\sigma}_j \in U_h,$$

$$\boldsymbol{w}_h = \sum_{j=1}^{\mathcal{N}_{\boldsymbol{v}}} w_h^j \boldsymbol{\phi}_j \in V_h, \quad \text{and} \quad q_h = \sum_{j=1}^{\mathcal{N}_p} q_h^j \psi_j \in P_h,$$

we write the algebraic form of the optimality system given in equations (3.7) as below:

$$\begin{bmatrix} M(\boldsymbol{\mu}) & 0 & 0 & A(\boldsymbol{\mu}) & B(\boldsymbol{\mu}) \\ 0 & 0 & 0 & B^T(\boldsymbol{\mu}) & 0 \\ 0 & 0 & N(\boldsymbol{\mu}) & C(\boldsymbol{\mu}) & 0 \\ A(\boldsymbol{\mu}) & B^T(\boldsymbol{\mu}) & C(\boldsymbol{\mu}) & 0 & 0 \\ B(\boldsymbol{\mu}) & 0 & 0 & 0 & 0 \end{bmatrix} \begin{bmatrix} \mathbf{v}(\boldsymbol{\mu}) \\ \mathbf{p}(\boldsymbol{\mu}) \\ \mathbf{u}(\boldsymbol{\mu}) \\ \mathbf{w}(\boldsymbol{\mu}) \\ \mathbf{q}(\boldsymbol{\mu}) \end{bmatrix} = \begin{bmatrix} \mathbf{h}(\boldsymbol{\mu}) \\ \mathbf{0} \\ \mathbf{0} \\ \mathbf{f}(\boldsymbol{\mu}) \\ \mathbf{g}(\boldsymbol{\mu}) \end{bmatrix}, \tag{3.8}$$

where, for a given $\boldsymbol{\mu}$, $(\mathbf{v}(\boldsymbol{\mu}), \mathbf{p}(\boldsymbol{\mu}), \mathbf{u}(\boldsymbol{\mu}), \mathbf{w}(\boldsymbol{\mu}), \mathbf{q}(\boldsymbol{\mu}))^T$ is the vector of finite element coefficients and $M(\boldsymbol{\mu}), A(\boldsymbol{\mu}) \in \mathbb{R}^{\mathcal{N}_{\boldsymbol{v}} \times \mathcal{N}_{\boldsymbol{v}}}$, $N(\boldsymbol{\mu}) \in \mathbb{R}^{\mathcal{N}_{\boldsymbol{u}} \times \mathcal{N}_{\boldsymbol{u}}}$, $B(\boldsymbol{\mu}) \in \mathbb{R}^{\mathcal{N}_{\boldsymbol{v}} \times \mathcal{N}_p}$ and $C(\boldsymbol{\mu}) \in \mathbb{R}^{\mathcal{N}_{\boldsymbol{u}} \times \mathcal{N}_{\boldsymbol{v}}}$ are the mass matrices associated to discretized versions of operators $\mathrm{m}(\cdot,\cdot;\boldsymbol{\mu})$, $\mathrm{a}(\cdot,\cdot;\boldsymbol{\mu})$, $\mathrm{n}(\cdot,\cdot;\boldsymbol{\mu})$, $\mathrm{b}(\cdot,\cdot;\boldsymbol{\mu})$ and $\mathrm{c}(\cdot,\cdot;\boldsymbol{\mu})$ respectively and are defined by equations (2.40) and (2.41). We reiterate that the system (3.8) can be directly implemented in finite elements based programming libraries, such as FEniCS and multiphenics.

Some preliminary numerical results for an idealized Y-shaped geometry are shown in chapter 2, section 2.5.2 and further application of this framework to patient-specific coronary artery bypass grafts has been shown in chapter 2, section 2.6. These results show that a single simulation using Galerkin finite element methods attains $\mathcal{O}(10^5)$ degrees of freedom and requires the computational time of $\mathcal{O}(10^2)$ to $\mathcal{O}(10^3)$ seconds. Thus, in parametrized settings if we tend to implement only high-order numerical methods, we will need to spend at least $\mathcal{O}(10^2)$ seconds for each different value of $\boldsymbol{\mu}$.

3.2. Reduced order methods for parametrized Stokes optimal flow control problems

In this section, we will present a reduced order framework to approximate the solution to discrete version of problem 3.2, for different tunings of parameters $\boldsymbol{\mu}$, in a time-efficient and reliable manner. The computational efficiency of reduced order methods arises from two factors, (i). the reduced dimensional solution manifold, and (ii). decomposition of the procedure into expensive and inexpensive phases, where only latter is needed in repetitive computing environment. Thus, the goal of this section is to construct a low dimensional solution manifold $\mathcal{M}_{\mathrm{N}} = \{\boldsymbol{\delta}_{\mathrm{N}}(\boldsymbol{\mu}),\ \boldsymbol{\delta} = \boldsymbol{v}, p, \boldsymbol{u}, \boldsymbol{w}, q,\ \boldsymbol{\mu} \in \mathcal{D}\}$ for the optimality system (3.7), from the high dimensional solution manifold $\mathcal{M}_h = \{\boldsymbol{\delta}_h(\boldsymbol{\mu}),\ \boldsymbol{\delta} = \boldsymbol{v}, p, \boldsymbol{u}, \boldsymbol{w}, q,\ \boldsymbol{\mu} \in \mathcal{D}\}$. Then, for different values of $\boldsymbol{\mu}$, one only needs to perform the Galerkin projection of $\boldsymbol{\delta}_h$ on $\mathcal{M}_{\mathrm{N}}$ to yield $\boldsymbol{\delta}_{\mathrm{N}} \approx \boldsymbol{\delta}_h$ and this can be done in the inexpensive phase.

In literature, one can rely on atleast two methods to construct the reduced order spaces, namely *greedy algorithm* [49, 88] and *proper orthogonal decomposition(POD)–Galerkin* [19, 49, 65, 79]. The former requires apriori knowledge of error estimators to construct nested reduced order spaces while the latter can be seen as a singular value decomposition algorithm, which constructs the reduced basis by capturing energy of full order solutions. In this work, we will utilize the latter and will construct the reduced order solution spaces from the information captured by *snapshots*, that are high order solutions to the *truth* problem 3.3. Both techniques have been utilized in the optimal flow control problems [16, 35, 60, 82, 81, 99] and in computational cardiovascular modeling [14, 17, 18].

3.2.1 Proper orthogonal decomposition (POD)–Galerkin approximations

Let us consider a finitely sampled subset Λ of the parameter set $\mathcal{D}$ as the training set. Then, to construct the reduced order spaces, we first collect the *snapshots* by solving the *truth* problem 3.3 for all $\boldsymbol{\mu} \in \Lambda$ through Galerkin finite element methods. Let us write the snapshot matrices as below:

$$\left.\begin{aligned} \mathfrak{X}_{\boldsymbol{v}} &= \left[\boldsymbol{v}_h\left(\boldsymbol{\mu}^1\right)\ \boldsymbol{v}_h\left(\boldsymbol{\mu}^2\right)\ \cdots\ \boldsymbol{v}_h\left(\boldsymbol{\mu}^{|\Lambda|}\right)\right], \\ \mathfrak{X}_{\boldsymbol{w}} &= \left[\boldsymbol{w}_h\left(\boldsymbol{\mu}^1\right)\ \boldsymbol{w}_h\left(\boldsymbol{\mu}^2\right)\ \cdots\ \boldsymbol{w}_h\left(\boldsymbol{\mu}^{|\Lambda|}\right)\right], \end{aligned}\right\} \quad 1 \le h \le \mathcal{N}_{\boldsymbol{v}},$$

$$\left.\begin{aligned} \mathfrak{X}_{p} &= \left[p_h\left(\boldsymbol{\mu}^1\right)\ p_h\left(\boldsymbol{\mu}^2\right)\ \cdots p_h\left(\boldsymbol{\mu}^{|\Lambda|}\right)\right], \\ \mathfrak{X}_{q} &= \left[q_h\left(\boldsymbol{\mu}^1\right)\ q_h\left(\boldsymbol{\mu}^2\right)\ \cdots q_h\left(\boldsymbol{\mu}^{|\Lambda|}\right)\right], \end{aligned}\right\} \quad 1 \le h \le \mathcal{N}_{p},$$

and

$$\mathfrak{X}_{\boldsymbol{u}} = \left[\boldsymbol{u}_h\left(\boldsymbol{\mu}^1\right)\ \boldsymbol{u}_h\left(\boldsymbol{\mu}^2\right)\ \cdots \boldsymbol{u}_h\left(\boldsymbol{\mu}^{|\Lambda|}\right)\right], \qquad 1 \le h \le \mathcal{N}_{\boldsymbol{u}}.$$

Then, to construct the POD basis, we solve the following eigenvalue problems:

$$\mathbb{A}^{\boldsymbol{\delta}}\boldsymbol{\rho}_{\mathrm{i}}^{\boldsymbol{\delta}} = \lambda_{\mathrm{i}}^{\boldsymbol{\delta}}\boldsymbol{\rho}_{\mathrm{i}}^{\boldsymbol{\delta}}, \qquad \mathrm{i} = 1, \ldots, |\Lambda|, \tag{3.9}$$

for the correlation matrices $\mathbb{A}^{\boldsymbol{\delta}} = \frac{1}{|\Lambda|}\mathfrak{X}_{\boldsymbol{\delta}}^T\mathfrak{X}_{\boldsymbol{\delta}}$ for $\boldsymbol{\delta} = \boldsymbol{v}, p, \boldsymbol{u}, \boldsymbol{w}, q$ such that the eigenvalues are arranged in the descending order. We keep $n = 1, \ldots, \mathrm{N}_{max} \ll |\Lambda|$ eigenvalue-eigenvector pairs $(\lambda^n, \boldsymbol{\rho}^n)$, for which the relative energy of eigenvalues is greater than certain prescribed tolerance,

$$\frac{\sum_{j=1}^{\mathrm{N}_{max}} \lambda_j^{\boldsymbol{\delta}}}{\sum_{j=1}^{|\Lambda|} \lambda_j^{\boldsymbol{\delta}}} > 1 - \epsilon_{tol},\ 0 < \epsilon_{tol} \ll 1,\ \boldsymbol{\delta} = \boldsymbol{v}, p, \boldsymbol{w}, \boldsymbol{u}, q. \tag{3.10}$$

We remark that if the eigenvalues are arranged in decreasing order, then the first $n = 1, \cdots, \mathrm{N}_{max}$ eigenvalues will satisfy the relation (3.10). Orthonormal POD bases are constructed from the retained n eigenvectors and are defined as below:

$$\begin{cases} \tilde{\boldsymbol{\phi}}_n^{\boldsymbol{v}} = \frac{1}{\sqrt{\lambda_n^{\boldsymbol{v}}}} \mathfrak{X}_{\boldsymbol{v}} \boldsymbol{\rho}_n^{\boldsymbol{v}}, \qquad \tilde{\psi}_n^p = \frac{1}{\sqrt{\lambda_n^p}} \mathfrak{X}_p \boldsymbol{\rho}_n^p, \\ \tilde{\boldsymbol{\sigma}}_n^{\boldsymbol{u}} = \frac{1}{\sqrt{\lambda_n^{\boldsymbol{u}}}} \mathfrak{X}_{\boldsymbol{u}} \boldsymbol{\rho}_n^{\boldsymbol{u}}, \\ \tilde{\boldsymbol{\zeta}}_n^{\boldsymbol{w}} = \frac{1}{\sqrt{\lambda_n^{\boldsymbol{w}}}} \mathfrak{X}_{\boldsymbol{w}} \boldsymbol{\rho}_n^{\boldsymbol{w}}, \qquad \tilde{\zeta}_n^q = \frac{1}{\sqrt{\lambda_n^q}} \mathfrak{X}_q \boldsymbol{\rho}_n^q. \end{cases} \tag{3.11}$$

The reduced order spaces are generated by the POD bases, and we will denote them with subscript N. Thus, if $S_{\mathrm{N}} = V_{\mathrm{N}} \times P_{\mathrm{N}}$ corresponds to reduced order state spaces, U_{N} denotes the reduced order control space and $Z_{\mathrm{N}} = Z_{\boldsymbol{v}_{\mathrm{N}}} \times Z_{p_{\mathrm{N}}}$ are the reduced order adjoint spaces, then, with $X_{\mathrm{N}} = S_{\mathrm{N}} \times U_{\mathrm{N}}$, the reduced order parametrized Stokes constrained optimal flow control problem reads:

Problem 3.4. *Given $\boldsymbol{\mu} \in \mathcal{D}$, find $(\mathbf{x}_{\mathrm{N}}(\boldsymbol{\mu}), \boldsymbol{z}_{\mathrm{N}}(\boldsymbol{\mu})) \in X_{\mathrm{N}} \times S_{\mathrm{N}}$ such that,*

$$\begin{cases} \mathcal{A}(\mathbf{x}_{\mathrm{N}}(\boldsymbol{\mu}), \mathbf{y}_{\mathrm{N}}; \boldsymbol{\mu}) + \mathcal{B}(\boldsymbol{z}_{\mathrm{N}}(\boldsymbol{\mu}), \mathbf{y}_{\mathrm{N}}; \boldsymbol{\mu}) = \langle \mathcal{H}(\boldsymbol{\mu}), \mathbf{y}_{\mathrm{N}} \rangle, & \forall\ \mathbf{y}_{\mathrm{N}} \in X_{\mathrm{N}}, \\ \mathcal{B}(\mathbf{x}_{\mathrm{N}}(\boldsymbol{\mu}), \boldsymbol{\kappa}_{\mathrm{N}}; \boldsymbol{\mu}) = \langle \mathcal{G}(\boldsymbol{\mu}), \boldsymbol{\kappa}_{\mathrm{N}} \rangle, & \forall\ \boldsymbol{\kappa}_{\mathrm{N}} \in Z_{\mathrm{N}}, \end{cases} \tag{3.12}$$

It is to be noted that up until now, the dimensions of the reduced order spaces are N_{max} each, thus total dimensions of the reduced order problem 3.4 are $\mathrm{N} = \mathrm{N}_{\boldsymbol{v}} + \mathrm{N}_p + \mathrm{N}_{\boldsymbol{u}} + \mathrm{N}_{\boldsymbol{w}} + \mathrm{N}_q = 5\mathrm{N}_{max}$.

Next, to consider algebraic structure of the problem 3.4, we consider the following bijections in a similar way as for Galerkin finite element variables (see chapter 2, section 2.5.1) :

$$\mathbf{v}_{\mathrm{N}} = \left(v_{\mathrm{N}}^1,\ v_{\mathrm{N}}^2,\ \cdots,\ v_{\mathrm{N}}^{\mathrm{N}_{max}}\right)^T \leftrightarrow \boldsymbol{v}_{\mathrm{N}} = \sum_{j=1}^{\mathrm{N}_{max}} v_{\mathrm{N}}^j \tilde{\boldsymbol{\phi}}_j^{\boldsymbol{v}} \in V_{\mathrm{N}},$$

$$\mathbf{w}_{\mathrm{N}} = \left(w_{\mathrm{N}}^1,\ w_{\mathrm{N}}^2,\ \cdots,\ w_{\mathrm{N}}^{\mathrm{N}_{max}}\right)^T \leftrightarrow \boldsymbol{w}_{\mathrm{N}} = \sum_{j=1}^{\mathrm{N}_{max}} w_{\mathrm{N}}^j \tilde{\boldsymbol{\zeta}}_j^{\boldsymbol{w}} \in Z_{\boldsymbol{v}_{\mathrm{N}}},$$

$$\mathbf{p}_{\mathrm{N}} = \left(p_{\mathrm{N}}^1,\ p_{\mathrm{N}}^2,\ \cdots,\ p_{\mathrm{N}}^{\mathrm{N}_{max}}\right)^T \leftrightarrow p_{\mathrm{N}} = \sum_{j=1}^{\mathrm{N}_{max}} p_{\mathrm{N}}^j \tilde{\psi}_j^p \in P_{\mathrm{N}},$$

$$\mathbf{q}_{\mathrm{N}} = \left(q_{\mathrm{N}}^1,\ q_{\mathrm{N}}^2,\ \cdots,\ q_{\mathrm{N}}^{\mathrm{N}_{max}}\right)^T \leftrightarrow q_{\mathrm{N}} = \sum_{j=1}^{\mathrm{N}_{max}} q_{\mathrm{N}}^j \tilde{\zeta}_j^q \in Z_{p_{\mathrm{N}}},$$

and

$$\mathbf{u}_{\mathrm{N}} = \left(u_{\mathrm{N}}^{1},\ u_{\mathrm{N}}^{2},\ \cdots,\ u_{\mathrm{N}}^{\mathrm{N}_{max}}\right)^{T} \leftrightarrow \boldsymbol{u}_{\mathrm{N}} = \sum_{j=1}^{\mathrm{N}_{max}} u_{\mathrm{N}}^{j} \tilde{\boldsymbol{\sigma}}_{j}^{\boldsymbol{u}} \in U_{\mathrm{N}},$$

Furthermore, with the reduced bases matrices, defined as below:

$$\mathfrak{Y}_{\boldsymbol{v}} = \left[\tilde{\boldsymbol{\phi}}_{1}^{\boldsymbol{v}}\ \tilde{\boldsymbol{\phi}}_{2}^{\boldsymbol{v}}\ \cdots\ \tilde{\boldsymbol{\phi}}_{\mathrm{N}_{max}}^{\boldsymbol{v}}\right]^{T}, \quad \mathfrak{Y}_{p} = \left[\tilde{\psi}_{1}^{p}\ \tilde{\psi}_{2}^{p}\ \cdots\ \tilde{\psi}_{\mathrm{N}_{max}}^{p}\right]^{T}, \quad \mathfrak{Y}_{\boldsymbol{u}} = \left[\tilde{\boldsymbol{\sigma}}_{1}^{\boldsymbol{u}}\ \tilde{\boldsymbol{\sigma}}_{2}^{\boldsymbol{u}}\ \cdots\ \tilde{\boldsymbol{\sigma}}_{\mathrm{N}_{max}}^{\boldsymbol{u}}\right]^{T},$$

$$\mathfrak{Y}_{\boldsymbol{w}} = \left[\tilde{\boldsymbol{\zeta}}_{1}^{\boldsymbol{w}}\ \tilde{\boldsymbol{\zeta}}_{2}^{\boldsymbol{w}}\ \cdots\ \tilde{\boldsymbol{\zeta}}_{\mathrm{N}_{max}}^{\boldsymbol{w}}\right]^{T} \qquad \text{and} \qquad \mathfrak{Y}_{q} = \left[\tilde{\zeta}_{1}^{q}\ \tilde{\zeta}_{2}^{q}\ \cdots\ \tilde{\zeta}_{\mathrm{N}_{max}}^{q}\right]^{T},$$

the reduced order coefficients are calculated through Galerkin projection, such that,

$$\mathbf{v}\left(\boldsymbol{\mu}\right) \approx \mathfrak{Y}_{\boldsymbol{v}} \mathbf{v}_{\mathrm{N}}\left(\boldsymbol{\mu}\right), \quad \mathbf{p}\left(\boldsymbol{\mu}\right) \approx \mathfrak{Y}_{p} \mathbf{p}_{\mathrm{N}}\left(\boldsymbol{\mu}\right), \quad \mathbf{u}\left(\boldsymbol{\mu}\right) \approx \mathfrak{Y}_{\boldsymbol{u}} \mathbf{u}_{\mathrm{N}}\left(\boldsymbol{\mu}\right),$$

$$\mathbf{w}\left(\boldsymbol{\mu}\right) \approx \mathfrak{Y}_{\boldsymbol{w}} \mathbf{w}_{\mathrm{N}}\left(\boldsymbol{\mu}\right), \quad \text{and} \quad \mathbf{q}\left(\boldsymbol{\mu}\right) \approx \mathfrak{Y}_{q} \mathbf{q}_{\mathrm{N}}\left(\boldsymbol{\mu}\right).$$

Now, we can write the algebraic form of the parametrized reduced order problem , similar to the discretized algebraic system (3.8), as below:

$$\begin{bmatrix} M_{\mathrm{N}}\left(\boldsymbol{\mu}\right) & 0 & 0 & A_{\mathrm{N}}\left(\boldsymbol{\mu}\right) & B_{\mathrm{N}}\left(\boldsymbol{\mu}\right) \\ 0 & 0 & 0 & B_{\mathrm{N}}^{T}\left(\boldsymbol{\mu}\right) & 0 \\ 0 & 0 & N_{\mathrm{N}}\left(\boldsymbol{\mu}\right) & C_{\mathrm{N}}\left(\boldsymbol{\mu}\right) & 0 \\ A_{\mathrm{N}}\left(\boldsymbol{\mu}\right) & B_{\mathrm{N}}^{T}\left(\boldsymbol{\mu}\right) & C_{\mathrm{N}}\left(\boldsymbol{\mu}\right) & 0 & 0 \\ B_{\mathrm{N}}\left(\boldsymbol{\mu}\right) & 0 & 0 & 0 & 0 \end{bmatrix} \begin{bmatrix} \mathbf{v}_{\mathrm{N}}\left(\boldsymbol{\mu}\right) \\ \mathbf{p}_{\mathrm{N}}\left(\boldsymbol{\mu}\right) \\ \mathbf{u}_{\mathrm{N}}\left(\boldsymbol{\mu}\right) \\ \mathbf{w}_{\mathrm{N}}\left(\boldsymbol{\mu}\right) \\ \mathbf{q}_{\mathrm{N}}\left(\boldsymbol{\mu}\right) \end{bmatrix} = \begin{bmatrix} \mathbf{h}_{\mathrm{N}}\left(\boldsymbol{\mu}\right) \\ \mathbf{0} \\ \mathbf{0} \\ \mathbf{f}_{\mathrm{N}}\left(\boldsymbol{\mu}\right) \\ \mathbf{g}_{\mathrm{N}}\left(\boldsymbol{\mu}\right) \end{bmatrix}. \tag{3.13}$$

Here, the entries of the left hand side matrix are the reduced order mass matrices, defined below:

$$M_{\mathrm{N}}\left(\boldsymbol{\mu}\right) = \mathfrak{Y}_{\boldsymbol{v}}^{T} M\left(\boldsymbol{\mu}\right) \mathfrak{Y}_{\boldsymbol{v}} \in \mathbb{R}^{\mathrm{N}_{\boldsymbol{v}} \times \mathrm{N}_{\boldsymbol{v}}}, \quad N_{\mathrm{N}}\left(\boldsymbol{\mu}\right) = \mathfrak{Y}_{\boldsymbol{u}}^{T} N\left(\boldsymbol{\mu}\right) \mathfrak{Y}_{\boldsymbol{u}} \in \mathbb{R}^{\mathrm{N}_{\boldsymbol{u}} \times \mathrm{N}_{\boldsymbol{u}}},$$

$$A_{\mathrm{N}}\left(\boldsymbol{\mu}\right) = \mathfrak{Y}_{\boldsymbol{w}}^{T} A\left(\boldsymbol{\mu}\right) \mathfrak{Y}_{\boldsymbol{v}} \in \mathbb{R}^{\mathrm{N}_{\boldsymbol{v}} \times \mathrm{N}_{\boldsymbol{w}}}, \quad B_{\mathrm{N}}\left(\boldsymbol{\mu}\right) = \mathfrak{Y}_{q}^{T} B\left(\boldsymbol{\mu}\right) \mathfrak{Y}_{\boldsymbol{v}} \in \mathbb{R}^{\mathrm{N}_{\boldsymbol{v}} \times \mathrm{N}_{q}},$$

and $C_{\mathrm{N}}\left(\boldsymbol{\mu}\right) = \mathfrak{Y}_{\boldsymbol{w}}^{T} C\left(\boldsymbol{\mu}\right) \mathfrak{Y}_{\boldsymbol{u}} \in \mathbb{R}^{\mathrm{N}_{\boldsymbol{w}} \times \mathrm{N}_{\boldsymbol{u}}}$. Moreover,

$$\mathbf{h}_{\mathrm{N}}\left(\boldsymbol{\mu}\right) = \mathfrak{Y}_{\boldsymbol{v}}^{T} \mathbf{h}\left(\boldsymbol{\mu}\right), \quad \mathbf{f}_{\mathrm{N}}\left(\boldsymbol{\mu}\right) = \mathfrak{Y}_{\boldsymbol{w}}^{T} \mathbf{f}\left(\boldsymbol{\mu}\right) \quad \text{and} \quad \mathbf{g}_{\mathrm{N}}\left(\boldsymbol{\mu}\right) = \mathfrak{Y}_{q}^{T} \mathbf{g}\left(\boldsymbol{\mu}\right).$$

3.2.2 Aggregation of spaces and supremizers enrichment

We recall that to ensure the existence of a unique solution to problem 3.4, we need to satisfy Brezzi's theorem 3.1 at the reduced order level. However, since we are utilizing the saddle-point problem at *snapshots* level too, therefore, we need to satisfy the assumptions of Brezzi's theorem both at *truth* level and reduced order level. Thus, for all $\boldsymbol{\mu} \in \Lambda$, at the *truth* level we need to satisfy the assumptions of theorem 2.7, given in chapter 2, section 2.5.1 and at the reduced order level, the following theorem shall be satisfied:

Theorem 3.2. *A unique solution to the saddle-point problem 3.4 will exist if the following conditions are satisfied,*

(i) $\mathcal{A} : X_{\mathrm{N}} \times X_{\mathrm{N}} \to \mathbb{R}$ *is continuous and satisfies,*

$$\exists\ a_{\mathrm{N}_0} > 0,\ \textit{such that} \inf_{\mathbf{x}_{\mathrm{N}} \setminus \{0\} \in X_{\mathrm{N}_0}} \frac{\mathcal{A}\left(\mathbf{x}_{\mathrm{N}}, \mathbf{x}_{\mathrm{N}}; \boldsymbol{\mu}\right)}{\|\mathbf{x}_{\mathrm{N}}\|^2_{X_{\mathrm{N}}}} \geq a_{\mathrm{N}_0}, \forall\ \boldsymbol{\mu} \in \mathcal{D}$$

where, $X_{\mathrm{N}_0} = \{\mathbf{x}_{\mathrm{N}} \in X_{\mathrm{N}}$ *such that* $\mathcal{B}\left(\mathbf{x}_{\mathrm{N}}, \boldsymbol{\kappa}_{\mathrm{N}}; \boldsymbol{\mu}\right) = 0\ \forall\ \boldsymbol{\kappa}_{\mathrm{N}} \in Z_{\mathrm{N}}\}$.

(ii) $\mathcal{B} : X_{\mathrm{N}} \times Z_{\mathrm{N}} \to \mathbb{R}$ *is continuous and satisfies the following inf-sup condition,*

$$\exists\ b_{\mathrm{N}_0} > 0,\ \textit{such that} \inf_{\boldsymbol{z}_{\mathrm{N}} \setminus \{0\} \in Z_{\mathrm{N}}} \sup_{\mathbf{x}_{\mathrm{N}} \setminus \{0\} \in X_{\mathrm{N}}} \frac{\mathcal{B}\left(\mathbf{x}_{\mathrm{N}}, \boldsymbol{z}_{\mathrm{N}}; \boldsymbol{\mu}\right)}{\|\mathbf{x}_{\mathrm{N}}\|_{X_{\mathrm{N}}} \|\boldsymbol{z}_{\mathrm{N}}\|_{Z_{\mathrm{N}}}} \geq b_{\mathrm{N}_0},\ \forall\ \boldsymbol{\mu} \in \mathcal{D}.$$

We know that the continuity of $\mathcal{A}$ and $\mathcal{B}$, and the coercivity of $\mathcal{A}$ over kernel of $\mathcal{B}$ will be satisfied for the finite element discretized spaces, $X_h \subset X$ and $Z_h \subset Z$, as they hold true for the continuous spaces X and Z (see the proof of theorem 2.6). Furthermore, we recall that the continuous inf-sup condition for $\mathcal{B}$ is satisfied if the equivalence assumption between state and adjoint spaces holds true. Since we are choosing the finite element spaces such that $S \supseteq S_h \equiv Z_h \subseteq Z$, we claim that the discretized inf-sup condition will be satisfied at the *truth* level.

Now, at the reduced order level, we can prove the continuity and coercivity of $\mathcal{A}$ over kernek of $\mathcal{B}$ and continuity of $\mathcal{B}$ in a similar way as has been done for the continuous and finite element cases, and we remark that to ensure the stability of optimal solution $(\mathbf{x}_{\mathrm{N}}, \boldsymbol{z}_{\mathrm{N}})$, we need to also satisfy the inf-sup condition for $\mathcal{B}$. However, the required crucial assumption of equivalent state and adjoint spaces is not trivially guaranteed by the way reduced order spaces are constructed and in this case, the inf-sup condition will not hold true. In this case, we can strongly consider the equivalence between S_{N} and Z_{N} through aggregation of spaces, that is, we consider the following reduced order state and adjoint spaces:

$$S_{\mathrm{N}} = \left\{\tilde{\boldsymbol{\phi}}^{\boldsymbol{v}}_n, \tilde{\psi}^{p}_n, \tilde{\boldsymbol{\zeta}}^{\boldsymbol{w}}_n, \tilde{\zeta}^{q}_n,\ n = 1,\ \cdots,\ \mathrm{N}_{max}\right\} \equiv Z_{\mathrm{N}}.$$

Furthermore, as already discussed in chapter 2, section 2.5.1, to avoid appearance of spurious pressure modes, we need to satisfy the LBB inf-sup condition, in other words, we need to ensure that the dimensions of velocity spaces are larger than the pressure spaces. At truth level, we ensure this by utilizing stable Taylor-Hood spaces $\mathbb{P}2-\mathbb{P}1$, however, the condition does not necessarily hold true for the reduced order spaces resulting from truth approximations. We give the LBB inf-sup condition at the reduced order level as below:

$$\exists\ \gamma_{\mathrm{N}_0} > 0,\ \text{such that} \inf_{\boldsymbol{\kappa}_{\boldsymbol{w}_{\mathrm{N}}} \setminus \{0\} \in Z_{\boldsymbol{v}_{\mathrm{N}}}} \sup_{\xi_{p_{\mathrm{N}}} \setminus \{0\} \in P_{\mathrm{N}}} \frac{b\left(\kappa_{\boldsymbol{w}_{\mathrm{N}}}, \xi_{p_{\mathrm{N}}}; \boldsymbol{\mu}\right)}{\|\kappa_{\boldsymbol{w}_{\mathrm{N}}}\|_{Z_{\boldsymbol{v}_{\mathrm{N}}}} \|\xi_{p\mathrm{N}}\|_{P_{\mathrm{N}}}} \geq \gamma_{\mathrm{N}_0},\ \forall\ \boldsymbol{\mu} \in \mathcal{D}. \quad (3.14)$$

To satisfy the condition (3.14), we enrich the velocity spaces with the solutions of divergence equation [19, 49, 94], that is, we define the supremizers operator $\mathcal{T}^{\mathrm{i}}_{\boldsymbol{v}_h} : Z_{p_h} \to V_h$ and $\mathcal{T}^{\mathrm{i}}_{\boldsymbol{w}_h} : P_h \to Z_{\boldsymbol{v}_h}$ defined as:

$$\left(\mathcal{T}^{\mathrm{i}}_{\boldsymbol{v}_h} q_h, \boldsymbol{v}_h\right) = \mathrm{b}\left(q_h, \boldsymbol{v}_h; \boldsymbol{\mu}^{\mathrm{i}}\right), \ \mathrm{i} = 1, \ \cdots, \ |\Lambda|, \tag{3.15}$$

and

$$\left(\mathcal{T}^{\mathrm{i}}_{\boldsymbol{w}_h} p_h, \boldsymbol{w}_h\right) = \mathrm{b}\left(p_h, \boldsymbol{w}_h; \boldsymbol{\mu}^{\mathrm{i}}\right), \ \mathrm{i} = 1, \ \cdots, \ |\Lambda|. \tag{3.16}$$

Then, performing POD on the supremizers, we retain N_{max} supremizer modes $\hat{\phi}^{\boldsymbol{v}}_n$, $\hat{\psi}^{\boldsymbol{w}}_n$ for state velocity and adjoint velocity respectively. The supremizers enriched and aggregated state and adjoint spaces are thus given as:

$$S_{\mathrm{N}} = (V_{\mathrm{N}} \oplus \mathcal{T}^{\boldsymbol{v}}_{\mathrm{N}}) \times P_{\mathrm{N}} \times (Z_{\boldsymbol{v}_{\mathrm{N}}} \oplus \mathcal{T}^{\boldsymbol{w}}_{\mathrm{N}}) \times Z_{p_{\mathrm{N}}} \equiv Z_{\mathrm{N}} \tag{3.17}$$

We remark that after supremizers enrichment the dimensions of state and adjoint velocity spaces are increased by 2 times, thus,

$$\dim\left(V_{\mathrm{N}}\right) = 2\mathrm{N}_{max} = \dim\left(Z_{\boldsymbol{v}_{\mathrm{N}}}\right), \dim\left(P_{\mathrm{N}}\right) = \mathrm{N}_{max} = \dim\left(Z_{p_{\mathrm{N}}}\right), \dim\left(U_{\mathrm{N}}\right) = \mathrm{N}_{max}.$$

Moreover, after the aggregation of spaces, the dimensions of state and adjoint reduced order spaces is given as:

$$\dim\left(S_{\mathrm{N}}\right) = \dim\left(V_{\mathrm{N}}\right) + \dim\left(Z_{\boldsymbol{v}_{\mathrm{N}}}\right) + \dim\left(P_{\mathrm{N}}\right) + \dim\left(Z_{p_{\mathrm{N}}}\right) = \dim\left(Z_{\mathrm{N}}\right),$$

thus,

$$N = \dim\left(S_{\mathrm{N}}\right) + \dim\left(Z_{\mathrm{N}}\right) + \dim\left(U_{\mathrm{N}}\right) = 13\mathrm{N}_{max}.$$

We remark that $13\mathrm{N}_{max} \ll \mathcal{N}$, while attaining almost same accuracy as Galerkin finite element methods, as will be shown by the numerical results in the next section.

3.2.3 Offline-online phase decomposition

Next, we will discuss the decomposition of computational procedure into two phases, namely, offline phase and online phase. The phase decomposition relies on the crucial assumption of affine decomposition, that is, we assume the each operator can be componentwise divided into parameter-dependent and parameter-independent parts. Thus, we assume,

$$M\left(\boldsymbol{\mu}\right) = \sum_{q=1}^{Q_{\mathrm{m}}} \theta^q_M\left(\boldsymbol{\mu}\right) M^q, \quad N^q\left(\boldsymbol{\mu}\right) = \sum_{q=1}^{Q_{\mathrm{n}}} \theta^q_N\left(\boldsymbol{\mu}\right) N^q, \quad A\left(\boldsymbol{\mu}\right) = \sum_{q=1}^{Q_{\mathrm{a}}} \theta^q_A\left(\boldsymbol{\mu}\right) A^q,$$

$$B\left(\boldsymbol{\mu}\right) = \sum_{q=1}^{Q_{\mathrm{b}}} \theta^q_B\left(\boldsymbol{\mu}\right) B^q, \quad C\left(\boldsymbol{\mu}\right) = \sum_{q=1}^{Q_{\mathrm{c}}} \theta^q_C\left(\boldsymbol{\mu}\right) C^q, \quad \mathbf{h}\left(\boldsymbol{\mu}\right) = \sum_{q=1}^{Q_{\boldsymbol{h}}} \theta^q_h\left(\boldsymbol{\mu}\right) \mathbf{h}^q,$$

$$\mathbf{f}(\boldsymbol{\mu}) = \sum_{q=1}^{Q_{\boldsymbol{f}}} \theta_f^q(\boldsymbol{\mu})\,\mathbf{f}^q \quad \text{and} \quad \mathbf{g}(\boldsymbol{\mu}) = \sum_{q=1}^{Q_{\boldsymbol{g}}} \theta_g^q(\boldsymbol{\mu})\,\mathbf{g}^q,$$

for the algebraic optimality system (3.8). Then the computational procedure will be performed in two stages, the $\boldsymbol{\mu}$-independent phase and $\boldsymbol{\mu}$-dependent phase. The former phase, also known as the offline phase, comprises of performing POD and construction of reduced order spaces. In this stage the $\boldsymbol{\mu}$-independent matrices, shown above, are assembled and stored. Thus, the computational cost of offline phase depends upon the *truth* dimensions, that is the cost relies on $\mathcal{O}(\mathcal{N})$ times $|\Lambda|$. The second stage, that is the online stage comprises of calling the stored theta-independent matrices for a given parameter $\boldsymbol{\mu}$, assembling reduced order terms, solving the reduced order problem 3.4, including evaluation of reduced order coefficients through Galerkin projection. Since this phase is performed for a single parameter value, thus, the computational cost of this phase depends only on the dimensions of reduced order problem, that is, $\mathcal{O}(\mathrm{N})$ and is therefore, very low.

3.3. Test cases: parametrized Stokes constrained optimal flow control problem

In this section, we will apply the reduced order framework for Stokes constrained optimal flow control problem to the test problem given in chapter 2, section 2.5.2. Thus, the computational domain is the Y-shape geometry shown in figure 2.5.1(a), with boundary mesh elements and volume mesh elements shown in figures 2.5.1(b) and 2.5.1(c) respectively. We will consider physical parametrization, that is Reynolds number, to study the flow pattern corresponding to different inlet flow velocities. Thus, $\boldsymbol{\mu} = Re \in \mathcal{D} = [100, 300]$ defining the velocity at the inlets through the following expression:

$$\boldsymbol{v}_{in} = -\frac{\eta\boldsymbol{\mu}}{R_{in}}\left(1 - \frac{r^2}{R_{in}^2}\right)\boldsymbol{n}_{in}, \tag{3.18}$$

where, η is constant viscosity, R_{in} is the maximum radius of inlets, $\boldsymbol{n}_{in}$ corresponds to outward normals to the inlets Γ_{in} and r is the distance between center of an inlet and corresponding mesh nodes.

Moreover, we consider the tracking-type objective functional with desired velocity $\boldsymbol{v}_o$ distributed across Ω through equation (2.45) with $v_{const} = 400\ mm/s$. Thus, the parametrized optimal flow control problem can be expressed by problem definition 3.1, with the objective to match $\boldsymbol{v}_o$ with $\boldsymbol{v}(\boldsymbol{\mu})$, given $\boldsymbol{\mu} \in \mathcal{D}$.

We randomly sample a training set Λ of 100 parameter values and solve the truth problem 3.3 for all $\boldsymbol{\mu} \in \Lambda$. As shown in chapter 2, section 2.5.2, for a single parameter value, for example, for $\mu = 300$, the Galerkin finite element problem yields $\mathcal{N} = 225248$ degrees of freedom and takes 120.7 seconds, thus for different values of $\boldsymbol{\mu}$, with Galerkin finite element approximations only, we will need to spend 120.7 seconds for each simulation. However, with POD–Galerkin, we consider $\mathrm{N}_{max} = 10$ and therefore 79 reduced bases

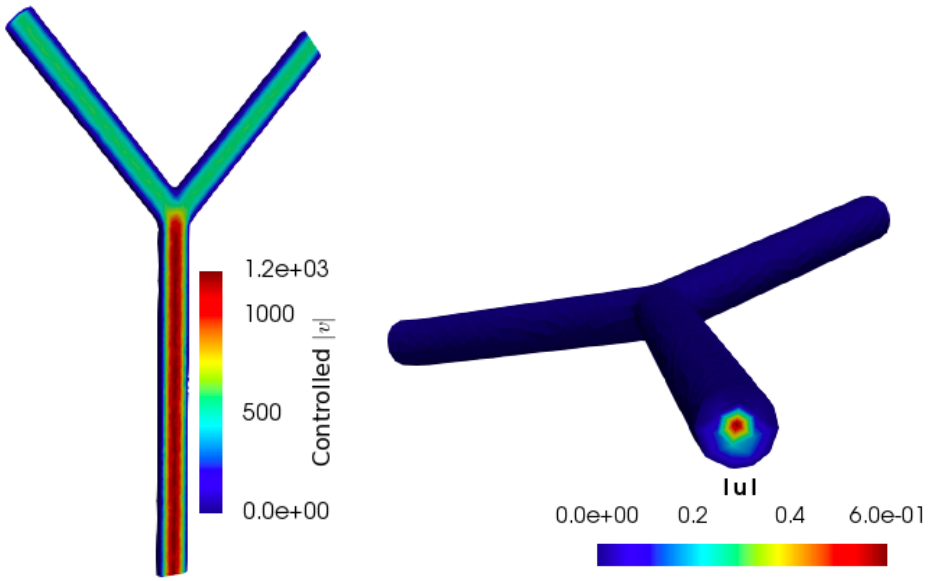

(a). (b).

Figure 3.3.1: Stokes constrained optimal control problem: (a). state velocity (mm/s). (b). boundary control magnitude (mm^2/s^2).

and the solution in the reduced order spaces generated by these bases can be calculated in only 5.3 seconds. In this case, we report the state velocity and boundary control in figures 3.3.1(a) and 3.3.1(b) respectively. Furthermore, in this a maximum speedup of $\mathcal{O}\left(10^4\right)$ is achieved by POD–Galerkin for both the approximated solution variables and the objective functional (see figure 3.3.2(b)). The computational details in this case are shown in table 3.3.2(a) which shows that the offline phase takes $\mathcal{O}\left(10^3\right)$ seconds which is expensive, however, once this phase is finished, we only need to pay the computational cost of $\mathcal{O}\left(10^0\right)$ seconds instead of $\mathcal{O}\left(10^2\right)$ seconds required by full-order simulations.

3.4. Parametrized Navier-Stokes constrained optimal flow control problem

In this section, we will extend the reduced order framework introduced for Stokes constrained optimal flow control problems in section 3.1 to parametrized version of the Navier-Stokes constrained optimal flow control problems, discussed in chapter 2, section 2.4.2. Thus, first let us write the parametrized version of problem 2.5. For the purpose, we consider physical parameters $\boldsymbol{\mu} \in \mathcal{D} \subset \mathbb{R}^d, d \in \mathbb{N}$, computational domain $\Omega \subset \mathbb{R}^3$ with Lipschitz boundary $\partial\Omega = \Gamma_{in} \cup \Gamma_w \cup \Gamma_o$, then the continuous version of parametrized Navier-Stokes constrained optimal flow control problem is given as:

Mesh size	15901
$\mathcal{D}$	$[100, 300]$
$\lvert\Lambda\rvert$	100
Offline phase	3002.42 seconds
Online phase	5.3 seconds

Table 3.1: (a).

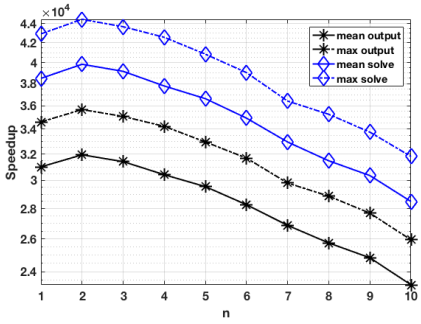

(b).

Figure 3.3.2: (a). Table demonstrating computational performance of POD–Galerkin for Stokes constrained optimal control problem in Y-shaped geometry. (b). Mean and maximum speedups for solution and objective functional achieved by POD–Galerkin for Stokes constrained optimal control problem in Y-shaped geometry.

Problem 3.5. *Given $\boldsymbol{\mu} \in \mathcal{D}$, find $(\boldsymbol{s}(\boldsymbol{\mu}), \boldsymbol{u}(\boldsymbol{\mu})) \in S \times U$ such that the objective functional* (3.1) *is minimized subject to,*

$$\begin{cases} -\eta \Delta \boldsymbol{v}(\boldsymbol{\mu}) + (\boldsymbol{v}(\boldsymbol{\mu}) \cdot \nabla) \boldsymbol{v}(\boldsymbol{\mu}) + \nabla p(\boldsymbol{\mu}) = \boldsymbol{f}(\boldsymbol{\mu}), & \text{in } \Omega, \\ \nabla \cdot \boldsymbol{v}(\boldsymbol{\mu}) = g(\boldsymbol{\mu}), & \text{in } \Omega, \\ \boldsymbol{v}(\boldsymbol{\mu}) = \boldsymbol{v}_{in}(\boldsymbol{\mu}), & \text{on } \Gamma_{in}, \\ \boldsymbol{v}(\boldsymbol{\mu}) = \boldsymbol{0}, & \text{on } \Gamma_{w}, \\ -\eta (\nabla \boldsymbol{v}(\boldsymbol{\mu})) \boldsymbol{n} + p(\boldsymbol{\mu}) \boldsymbol{n} = \boldsymbol{u}(\boldsymbol{\mu}), & \text{on } \Gamma_{o}, \end{cases} \tag{3.19}$$

where $\boldsymbol{s} = (\boldsymbol{v}, p) \in S(\Omega) = V(\Omega) \times P(\Omega)$ denotes state variables and $\boldsymbol{u} \in U(\Gamma_o)$ denotes the control variables. Moreover, $\boldsymbol{f}$ are the body forces, $\eta > 0$ is the kinematic viscosity, $g = 0$ will lead to incompressible fluids and $(\boldsymbol{v}(\boldsymbol{\mu}) \cdot \nabla) \boldsymbol{v}(\boldsymbol{\mu})$ is the convection term. We recall that with the adjoint variables or Lagrange multipliers $\boldsymbol{z} = (\boldsymbol{w}, q) \in Z(\Omega) = Z_{\boldsymbol{v}}(\Omega) \times Z_p(\Omega)$ and $X = S \times U$, the problem 3.5 can be cast in the following saddle-point form:

Problem 3.6. *Given $\boldsymbol{\mu} \in \mathcal{D}$, find $(\mathbf{x}(\boldsymbol{\mu}), \boldsymbol{z}(\boldsymbol{\mu})) \in X \times Z$, such that,*

$$\begin{cases} \mathcal{A}(\mathbf{x}(\boldsymbol{\mu}), \mathbf{y}; \boldsymbol{\mu}) + \mathcal{B}(\mathbf{y}, \boldsymbol{z}(\boldsymbol{\mu}); \boldsymbol{\mu}) + \mathrm{e}(\mathbf{y}_{\boldsymbol{v}}, \boldsymbol{v}(\boldsymbol{\mu}), \boldsymbol{w}(\boldsymbol{\mu}); \boldsymbol{\mu}) + \mathrm{e}(\boldsymbol{v}(\boldsymbol{\mu}), \mathbf{y}_{\boldsymbol{v}}, \boldsymbol{w}(\boldsymbol{\mu}); \boldsymbol{\mu}) = \langle \mathcal{H}(\boldsymbol{\mu}), \mathbf{y} \rangle, & \forall\, \mathbf{y} \in X, \\ \mathcal{B}(\mathbf{x}(\boldsymbol{\mu}), \boldsymbol{\kappa}; \boldsymbol{\mu}) + \mathrm{e}(\boldsymbol{v}(\boldsymbol{\mu}), \boldsymbol{v}(\boldsymbol{\mu}), \boldsymbol{\kappa}_{\boldsymbol{v}}; \boldsymbol{\mu}) = \langle \mathcal{G}(\boldsymbol{\mu}), \boldsymbol{\kappa} \rangle, & \forall\, \boldsymbol{\kappa} \in Z, \end{cases} \tag{3.20}$$

where $\mathcal{A} : X \times X \to \mathbb{R}$ and $\mathcal{B} : X \times Z \to \mathbb{R}$ are defined in problem 3.2 and

$$\mathrm{e}(\boldsymbol{v}, \boldsymbol{v}, \boldsymbol{\kappa}_{\boldsymbol{v}}; \boldsymbol{\mu}) = \int_{\Omega} (\boldsymbol{v} \cdot \nabla) \boldsymbol{v} \cdot \boldsymbol{\kappa}_{\boldsymbol{v}} d\Omega, \quad \mathrm{e}(\mathbf{y}_{\boldsymbol{v}}, \boldsymbol{v}, \boldsymbol{w}; \boldsymbol{\mu}) = \int_{\Omega} (\mathbf{y}_{\boldsymbol{v}} \cdot \nabla) \boldsymbol{v} \cdot \boldsymbol{w} d\Omega,$$

and

$$\mathrm{e}(\boldsymbol{v}, \mathbf{y}_{\boldsymbol{v}}, \boldsymbol{w}; \boldsymbol{\mu}) = \int_{\Omega} (\boldsymbol{v} \cdot \nabla) \mathbf{y}_{\boldsymbol{v}} \cdot \boldsymbol{w} d\Omega.$$

Truth approximations

We consider the finite element spaces $X_h \subset X$ and $Z_h \subset Z$, such that $X_h = S_h = (V_h \times P_h) \times U_h$ and $Z_h \equiv S_h$, then we can write the discretized version of the parametrized Navier-Stokes constrained optimal flow control problem 3.6 as below:

Problem 3.7. *Given $\boldsymbol{\mu} \in \mathcal{D}$, find $(\mathbf{x}_h(\boldsymbol{\mu}), \boldsymbol{z}_h(\boldsymbol{\mu})) \in X_h \times Z_h$, such that,*

$$\begin{cases} \mathcal{A}(\mathbf{x}_h(\boldsymbol{\mu}), \mathbf{y}_h; \boldsymbol{\mu}) + \mathcal{B}(\mathbf{y}_h, \boldsymbol{z}_h(\boldsymbol{\mu}); \boldsymbol{\mu}) + \mathrm{e}(\mathbf{y}_{\boldsymbol{v}_h}, \boldsymbol{v}_h(\boldsymbol{\mu}), \boldsymbol{w}_h(\boldsymbol{\mu}); \boldsymbol{\mu}) + \mathrm{e}_h(\boldsymbol{v}_h(\boldsymbol{\mu}), \mathbf{y}_{\boldsymbol{v}_h}, \boldsymbol{w}_h(\boldsymbol{\mu}); \boldsymbol{\mu}) = \langle \mathcal{H}(\boldsymbol{\mu}), \mathbf{y}_h \rangle, & \forall\, \mathbf{y}_h \in X_h, \\ \mathcal{B}(\mathbf{x}_h(\boldsymbol{\mu}), \boldsymbol{\kappa}_h; \boldsymbol{\mu}) + \mathrm{e}(\boldsymbol{v}_h(\boldsymbol{\mu}), \boldsymbol{v}_h(\boldsymbol{\mu}), \boldsymbol{\kappa}_{\boldsymbol{v}_h}; \boldsymbol{\mu}) = \langle \mathcal{G}(\boldsymbol{\mu}), \boldsymbol{\kappa}_h \rangle, & \forall\, \boldsymbol{\kappa}_h \in Z_h. \end{cases} \tag{3.21}$$

where $\mathcal{A} : X_h \times X_h \to \mathbb{R}$ and $\mathcal{B} : X_h \times Z_h \to \mathbb{R}$ are defined in problem 3.3.

We denote the dimensions of finite element spaces with $\mathcal{N}_{\boldsymbol{\delta}}$ for $\boldsymbol{\delta} = \boldsymbol{v}, p, \boldsymbol{u}, \boldsymbol{w}, q$, then with the bijections $V_h \leftrightarrow \mathbb{R}^{\mathcal{N}_{\boldsymbol{v}}}$, $P_h \leftrightarrow \mathbb{R}^{\mathcal{N}_p}$ and $U_h \leftrightarrow \mathbb{R}^{\mathcal{N}_{\boldsymbol{u}}}$, we can give the algebraic form of problem 3.7 as below:

Problem 3.8. *Given $\boldsymbol{\mu} \in \mathcal{D}$, find $(\mathbf{v}(\boldsymbol{\mu}), \mathbf{p}(\boldsymbol{\mu}), \mathbf{u}(\boldsymbol{\mu}), \mathbf{w}(\boldsymbol{\mu}), \mathbf{q}(\boldsymbol{\mu}))^T \in X_h \times Z_h$, such that,*

$$\begin{bmatrix} M(\boldsymbol{\mu}) + \tilde{E}(\mathbf{w}(\boldsymbol{\mu}); \boldsymbol{\mu}) & 0 & 0 & A(\boldsymbol{\mu}) + E(\mathbf{v}(\boldsymbol{\mu}); \boldsymbol{\mu}) & B(\boldsymbol{\mu}) \\ 0 & 0 & 0 & B^T(\boldsymbol{\mu}) & 0 \\ 0 & 0 & N(\boldsymbol{\mu}) & C(\boldsymbol{\mu}) & 0 \\ A(\boldsymbol{\mu}) + E(\mathbf{v}(\boldsymbol{\mu}); \boldsymbol{\mu}) & B^T(\boldsymbol{\mu}) & C(\boldsymbol{\mu}) & 0 & 0 \\ B(\boldsymbol{\mu}) & 0 & 0 & 0 & 0 \end{bmatrix} \begin{bmatrix} \mathbf{v}(\boldsymbol{\mu}) \\ \mathbf{p}(\boldsymbol{\mu}) \\ \mathbf{u}(\boldsymbol{\mu}) \\ \mathbf{w}(\boldsymbol{\mu}) \\ \mathbf{q}(\boldsymbol{\mu}) \end{bmatrix} = \begin{bmatrix} \mathbf{h}(\boldsymbol{\mu}) \\ \mathbf{0} \\ \mathbf{0} \\ \mathbf{f}(\boldsymbol{\mu}) \\ \mathbf{g}(\boldsymbol{\mu}) \end{bmatrix}. \tag{3.22}$$

Here, for $1 \leq i, j \leq \mathcal{N}_{\boldsymbol{v}}$,

$$(E(\mathbf{v}(\boldsymbol{\mu}); \boldsymbol{\mu}))_{ij} = \sum_{k=1}^{\mathcal{N}_{\boldsymbol{v}}} v_h^k(\boldsymbol{\mu})\ e(\boldsymbol{\phi}_k, \boldsymbol{\phi}_j, \boldsymbol{\phi}_i; \boldsymbol{\mu}) \text{ and } \left(\tilde{E}(\mathbf{w}(\boldsymbol{\mu}); \boldsymbol{\mu})\right)_{ij} = \sum_{k=1}^{\mathcal{N}_{\boldsymbol{v}}} w_h^k(\boldsymbol{\mu})\ e(\boldsymbol{\phi}_k, \boldsymbol{\phi}_j, \boldsymbol{\phi}_i; \boldsymbol{\mu}),$$

and furthermore, for $1 \leq k \leq \mathcal{N}_p$ and $1 \leq l, r \leq \mathcal{N}_{\boldsymbol{u}}$,

$$(A(\boldsymbol{\mu}))_{ij} = \mathrm{a}(\boldsymbol{\phi}_i, \boldsymbol{\phi}_j; \boldsymbol{\mu}), \quad (B(\boldsymbol{\mu}))_{ik} = \mathrm{b}(\boldsymbol{\psi}_k, \boldsymbol{\phi}_i; \boldsymbol{\mu}), \quad (C(\boldsymbol{\mu}))_{il} = \mathrm{c}(\boldsymbol{\sigma}_l, \boldsymbol{\phi}_i; \boldsymbol{\mu}),$$

$$(M(\boldsymbol{\mu}))_{ij} = \mathrm{m}(\boldsymbol{\phi}_i, \boldsymbol{\phi}_j; \boldsymbol{\mu}), \qquad (N(\boldsymbol{\mu}))_{lr} = \mathrm{n}(\boldsymbol{\sigma}_r, \boldsymbol{\sigma}_l; \boldsymbol{\mu}),$$

$$\mathbf{h}(\boldsymbol{\mu})_i = \langle \boldsymbol{h}(\boldsymbol{\mu}), \boldsymbol{\phi}_i \rangle, \quad \mathbf{f}(\boldsymbol{\mu})_i = \langle \boldsymbol{f}(\boldsymbol{\mu}), \boldsymbol{\phi}_i \rangle, \text{ and } \mathbf{g}(\boldsymbol{\mu})_k = \langle g(\boldsymbol{\mu}), \boldsymbol{\psi}_k \rangle.$$

We recall that the optimality system (3.22) is nonlinear and can be solved through iterative numerical schemes such as Newton method (see chapter 2, section 2.5.4).

3.5. Reduced order methods for parametrized Navier-Stokes optimal flow control problems

Next, we will extend the reduced order framework, constructed with POD–Galerkin to parametrized Navier-Stokes constrained optimal flow control problem, discussed in section 3.4. For the purpose, let us reiterate that we will built the reduced order spaces from *snapshots* that will be the Galerkin finite element solutions to the truth problem 3.7. Furthermore, we also reiterate that the goal of constructing such framework is to explore solution in low-dimensional spaces while retaining the reliability of high-order solution spaces and decoupling of the computational procedure in two separate phases, where the one with low computational cost is repeatedly performed for different tunings of $\boldsymbol{\mu}$.

In this case, the algorithm is similar to what has been discussed in section 3.2.1. Thus, for all parameter values $\boldsymbol{\mu}^{\mathrm{i}}$ in a finitely sampled subset of parameters $\Lambda \subset \mathcal{D}$, we collect the truth solutions, or snapshots by solving the optimality system 3.22 with Newton method. The snapshot matrices can be written as:

$$\mathfrak{X}_{\boldsymbol{\delta}} = \left[\boldsymbol{\delta}_h^1\left(\boldsymbol{\mu}^1\right)\ \boldsymbol{\delta}_h^2\left(\boldsymbol{\mu}^2\right)\ \cdots\ \boldsymbol{\delta}_h^{|\Lambda|}\left(\boldsymbol{\mu}^{|\Lambda|}\right)\right],\ \text{for } \boldsymbol{\delta} = \boldsymbol{v}, p, \boldsymbol{u}, \boldsymbol{w}, q,\ \text{and } 1 \leq h \leq \mathcal{N}_{\boldsymbol{\delta}}.$$

Then, by solving $\mathrm{i} = 1, \ldots, |\Lambda|$ eigenvalues problems, defined by (3.9), where $\mathbb{A}^{\boldsymbol{\delta}} = \frac{1}{|\Lambda|}\mathfrak{X}_{\boldsymbol{\delta}}^T\mathfrak{X}_{\boldsymbol{\delta}} \in \mathbb{R}^{|\Lambda|\times|\Lambda|}$ are the correlation matrices, we keep first N_{max} eigenvectors, corresponding to largest eigenvalues. Orthonormal POD bases are constructed from the retained eigenvectors and are defined by equations (3.11). Thus, the reduced order spaces are defined as below:

state spaces := $S_{\mathrm{N}} = V_{\mathrm{N}} \times P_{\mathrm{N}}$, such that

$$V_{\mathrm{N}} = \left\{\tilde{\boldsymbol{\phi}}_n^{\boldsymbol{v}},\ n = 1,\ \cdots,\ \mathrm{N}_{max}\right\},\ P_{\mathrm{N}} = \left\{\tilde{\boldsymbol{\psi}}_n^{p},\ n = 1,\ \cdots,\ \mathrm{N}_{max}\right\},$$

adjoint spaces := $Z_{\mathrm{N}} = Z_{\boldsymbol{v}_{\mathrm{N}}} \times Z_{p_{\mathrm{N}}}$, such that

$$Z_{\boldsymbol{v}_{\mathrm{N}}} = \left\{\tilde{\boldsymbol{\zeta}}_n^{\boldsymbol{w}},\ n = 1,\ \cdots,\ \mathrm{N}_{max}\right\},\ Z_{p_{\mathrm{N}}} = \left\{\tilde{\boldsymbol{\zeta}}_n^{a},\ n = 1,\ \cdots,\ \mathrm{N}_{max}\right\},$$

and control space := $U_{\mathrm{N}} = \{\tilde{\boldsymbol{\sigma}}_n^{\boldsymbol{u}},\ n = 1,\ \cdots,\ \mathrm{N}_{max}\}$. Considering $X_{\mathrm{N}} = S_{\mathrm{N}} \times U_{\mathrm{N}}$, the reduced order parametrized Navier-Stokes constrained optimal flow control problem can be defined as:

Problem 3.9. *Given $\boldsymbol{\mu} \in \mathcal{D}$, find $(\mathbf{x}_{\mathrm{N}}(\boldsymbol{\mu}), \boldsymbol{z}_{\mathrm{N}}(\boldsymbol{\mu})) \in X_{\mathrm{N}} \times Z_{\mathrm{N}}$, such that,*

$$\begin{cases} \mathcal{A}(\mathbf{x}_{\mathrm{N}}(\boldsymbol{\mu}), \mathbf{y}_{\mathrm{N}}; \boldsymbol{\mu}) + \mathcal{B}(\mathbf{y}_{\mathrm{N}}, \boldsymbol{z}_{\mathrm{N}}(\boldsymbol{\mu}); \boldsymbol{\mu}) + \mathrm{e}(\mathbf{y}_{\boldsymbol{v}_{\mathrm{N}}}, \boldsymbol{v}_{\mathrm{N}}(\boldsymbol{\mu}), \boldsymbol{w}_{\mathrm{N}}(\boldsymbol{\mu}); \boldsymbol{\mu}) + \mathrm{e}(\boldsymbol{v}_{\mathrm{N}}(\boldsymbol{\mu}), \mathbf{y}_{\boldsymbol{v}_{\mathrm{N}}}, \boldsymbol{w}_{\mathrm{N}}(\boldsymbol{\mu}); \boldsymbol{\mu}) = \langle \mathcal{H}(\boldsymbol{\mu}), \mathbf{y}_{\mathrm{N}} \rangle, & \forall\ \mathbf{y}_{\mathrm{N}} \in X_{\mathrm{N}}, \\ \mathcal{B}(\mathbf{x}_{\mathrm{N}}(\boldsymbol{\mu}), \boldsymbol{\kappa}_{\mathrm{N}}; \boldsymbol{\mu}) + \mathrm{e}(\boldsymbol{v}_{\mathrm{N}}(\boldsymbol{\mu}), \boldsymbol{v}_{\mathrm{N}}(\boldsymbol{\mu}), \boldsymbol{\kappa}_{\boldsymbol{v}_{\mathrm{N}}}; \boldsymbol{\mu}) = \langle \mathcal{G}(\boldsymbol{\mu}), \boldsymbol{\kappa}_{\mathrm{N}} \rangle, & \forall\ \boldsymbol{\kappa}_{\mathrm{N}} \in Z_{\mathrm{N}}, \end{cases} \tag{3.23}$$

where, $\mathbf{x}_{\mathrm{N}} = (\boldsymbol{v}_{\mathrm{N}}, p_{\mathrm{N}}, \boldsymbol{u}_{\mathrm{N}}) \in X_{\mathrm{N}}$ and $\boldsymbol{z}_{\mathrm{N}} = (\boldsymbol{w}_{\mathrm{N}}, q_{\mathrm{N}}) \in Z$, such that,

$$\boldsymbol{v}_{\mathrm{N}}(\boldsymbol{\mu}) = \sum_{n=1}^{\mathrm{N}_{max}} v_{\mathrm{N}}^{n}(\boldsymbol{\mu})\, \tilde{\phi}_{n}^{\boldsymbol{v}} \in V_{\mathrm{N}},\ p_{\mathrm{N}}(\boldsymbol{\mu}) = \sum_{n=1}^{\mathrm{N}_{max}} p_{\mathrm{N}}^{n}(\boldsymbol{\mu})\, \tilde{\psi}_{n}^{p} \in P_{\mathrm{N}},$$

$$\boldsymbol{w}_{\mathrm{N}}(\boldsymbol{\mu}) = \sum_{n=1}^{\mathrm{N}_{max}} w_{\mathrm{N}}^{n}(\boldsymbol{\mu})\, \tilde{\zeta}_{n}^{\boldsymbol{w}} \in Z_{\boldsymbol{v}_{\mathrm{N}}},\ q_{\mathrm{N}}(\boldsymbol{\mu}) = \sum_{n=1}^{\mathrm{N}_{max}} q_{\mathrm{N}}^{n}(\boldsymbol{\mu})\, \tilde{\zeta}_{n}^{q} \in Z_{p_{\mathrm{N}}},$$

and $\boldsymbol{u}_{\mathrm{N}}(\boldsymbol{\mu}) = \sum_{n=1}^{\mathrm{N}_{max}} u_{\mathrm{N}}^{n}(\boldsymbol{\mu})\, \tilde{\sigma}_{n}^{\boldsymbol{u}} \in U_{\mathrm{N}}$.

Then, for $\mathfrak{Y} = diag(\mathfrak{Y}_{\boldsymbol{v}}, \mathfrak{Y}_{p}, \mathfrak{Y}_{\boldsymbol{u}}, \mathfrak{Y}_{\boldsymbol{w}}, \mathfrak{Y}_{q})$ and $\mathbf{0} = (\mathbf{0}, \mathbf{0}, \mathbf{0}, \mathbf{0}, \mathbf{0})^{T}$, the the optimality system (3.23) can be written in the following algebraic form :

$$\mathfrak{Y}^{T}\mathbb{W} = \mathbf{0}, \tag{3.24}$$

where,

$$\mathbb{W} = \begin{bmatrix} \left(M(\boldsymbol{\mu}) + \tilde{E}\left(\mathfrak{Y}_{\boldsymbol{w}}\boldsymbol{w}_{\mathrm{N}}(\boldsymbol{\mu});\boldsymbol{\mu}\right)\right)\mathfrak{Y}_{\boldsymbol{v}}\boldsymbol{v}_{\mathrm{N}}(\boldsymbol{\mu}) + \left(A_{ad}(\boldsymbol{\mu}) + E_{ad}\left(\mathfrak{Y}_{\boldsymbol{v}}\mathbf{v}_{\mathrm{N}}(\boldsymbol{\mu});\boldsymbol{\mu}\right)\right)\mathfrak{Y}_{\boldsymbol{w}}\boldsymbol{w}_{\mathrm{N}}(\boldsymbol{\mu}) + B_{ad}^{T}(\boldsymbol{\mu})\,\mathfrak{Y}_{q}\mathbf{q}_{\mathrm{N}}(\boldsymbol{\mu}) - \mathbf{h}(\boldsymbol{\mu}) \\ B_{ad}(\boldsymbol{\mu})\,\mathfrak{Y}_{\boldsymbol{w}}\mathbf{w}_{\mathrm{N}}(\boldsymbol{\mu}) \\ N(\boldsymbol{\mu})\,\mathfrak{Y}_{\boldsymbol{u}}\mathbf{u}_{\mathrm{N}}(\boldsymbol{\mu}) + C(\boldsymbol{\mu})\,\mathfrak{Y}_{\boldsymbol{w}}\mathbf{w}_{\mathrm{N}}(\boldsymbol{\mu}) \\ \left(A(\boldsymbol{\mu}) + E\left(\mathfrak{Y}_{\boldsymbol{v}}\mathbf{v}_{\mathrm{N}}(\boldsymbol{\mu});\boldsymbol{\mu}\right)\right)\mathfrak{Y}_{\boldsymbol{v}}\boldsymbol{v}_{\mathrm{N}}(\boldsymbol{\mu}) + B^{T}(\boldsymbol{\mu})\,\mathfrak{Y}_{p}\mathbf{p}_{\mathrm{N}} + C(\boldsymbol{\mu})\,\mathfrak{Y}_{\boldsymbol{u}}\mathbf{u}_{\mathrm{N}}(\boldsymbol{\mu})(\boldsymbol{\mu}) - \mathbf{f}(\boldsymbol{\mu}) \\ B(\boldsymbol{\mu})\,\mathfrak{Y}_{\boldsymbol{v}}\mathbf{v}_{\mathrm{N}}(\boldsymbol{\mu}) - \mathbf{g}(\boldsymbol{\mu}) \end{bmatrix}$$

Thus, the reduced order mass matrices can be defined as:

$$\begin{aligned} M_{\mathrm{N}}(\boldsymbol{\mu}) &= \mathfrak{Y}_{\boldsymbol{v}}^{T}M(\boldsymbol{\mu})\,\mathfrak{Y}_{\boldsymbol{v}}, \quad N_{\mathrm{N}}(\boldsymbol{\mu}) = \mathfrak{Y}_{\boldsymbol{u}}^{T}N(\boldsymbol{\mu})\,\mathfrak{Y}_{\boldsymbol{u}}, \quad A_{\mathrm{N}}(\boldsymbol{\mu}) = \mathfrak{Y}_{\boldsymbol{w}}^{T}A(\boldsymbol{\mu})\,\mathfrak{Y}_{\boldsymbol{v}}, \\ A_{ad_{\mathrm{N}}}(\boldsymbol{\mu}) &= \mathfrak{Y}_{\boldsymbol{v}}^{T}A_{ad}(\boldsymbol{\mu})\,\mathfrak{Y}_{\boldsymbol{w}}, \quad B_{\mathrm{N}} = \mathfrak{Y}_{q}^{T}B(\boldsymbol{\mu})\,\mathfrak{Y}_{\boldsymbol{v}}, \quad B_{ad_{\mathrm{N}}} = \mathfrak{Y}_{p}^{T}B_{ad}(\boldsymbol{\mu})\,\mathfrak{Y}_{\boldsymbol{w}}, \\ E_{\mathrm{N}}(\cdot,\ \cdot;\boldsymbol{\mu}) &= \mathfrak{Y}_{\boldsymbol{w}}^{T}E(\cdot,\ \cdot;\boldsymbol{\mu})\,\mathfrak{Y}_{\boldsymbol{v}}, \quad E_{ad_{\mathrm{N}}}(\cdot,\ \cdot;\boldsymbol{\mu}) = \mathfrak{Y}_{\boldsymbol{v}}^{T}E_{ad}(\cdot,\ \cdot;\boldsymbol{\mu})\,\mathfrak{Y}_{\boldsymbol{w}}, \end{aligned}$$

and

$$\tilde{E}_{\mathrm{N}}(\cdot,\ \cdot;\boldsymbol{\mu}) = \mathfrak{Y}_{\boldsymbol{v}}^{T}\tilde{E}(\cdot,\ \cdot;\boldsymbol{\mu})\,\mathfrak{Y}_{\boldsymbol{v}}.$$

For $\hat{W}_{\mathrm{N}} = (\mathbf{v}_{\mathrm{N}}(\boldsymbol{\mu}), \mathbf{p}_{\mathrm{N}}(\boldsymbol{\mu}), \mathbf{u}_{\mathrm{N}}(\boldsymbol{\mu}), \mathbf{w}_{\mathrm{N}}(\boldsymbol{\mu}), \mathbf{q}_{\mathrm{N}}(\boldsymbol{\mu}))^{T}$, the non-linear optimality system (3.24) can be solved using Newton method. Thus, at any generic $k-th$ iteration we solve:

$$d\mathbb{W}\left(\hat{W}_{\mathrm{N}}^{k-1}\right)\delta\hat{W}_{\mathrm{N}} = -\mathbb{W}\left(\hat{W}_{\mathrm{N}}^{k-1}\right), \tag{3.25}$$

where, $\mathbb{W}\left(\hat{W}_{\mathrm{N}}\right)$ is the residual based optimality system (3.24), $d\mathbb{W}\left(\hat{W}_{\mathrm{N}}\right)$ is the Jacobian matrix and $\delta\hat{W}_{\mathrm{N}} = \hat{W}_{\mathrm{N}}^{k} - \hat{W}_{\mathrm{N}}^{k-1}$ is the increment at corresponding generic iteration.

Supremizer enrichment and aggregation of spaces

To ensure uniqueness of pressure, we proceed in a similar way as in the case of Stokes constrained optimal flow control problem. Thus, we consider the supremizers operators $\mathcal{T}^{\mathrm{i}}_{\boldsymbol{v}_h} : Z_{p_h} \to V_h$ and $\mathcal{T}^{\mathrm{i}}_{\boldsymbol{w}_h} : P_h \to Z_{\boldsymbol{v}_h}$, defined by equations (3.15) and (3.16) respectively. Then, if we take

$$\mathcal{T}^{\boldsymbol{v}}_{\mathrm{N}} = \left\{\hat{\boldsymbol{\phi}}^{\boldsymbol{v}}_n,\ n = 1,\ \cdots,\ \mathrm{N}_{max}\right\}, \quad \mathcal{T}^{\boldsymbol{w}}_{\mathrm{N}} = \left\{\hat{\boldsymbol{\zeta}}^{\boldsymbol{w}}_n,\ n = 1,\ \cdots,\ \mathrm{N}_{max}\right\}$$

to be the spaces of POD modes for $\mathcal{T}^{\mathrm{i}}_{\boldsymbol{v}_h}$ and $\mathcal{T}^{\mathrm{i}}_{\boldsymbol{w}_h}$ respectively, then the supremizer enriched state and adjoint velocity spaces can be defined as:

$$V_{\mathrm{N}} \oplus \mathcal{T}^{\boldsymbol{v}}_{\mathrm{N}} = span\left\{\tilde{\boldsymbol{\phi}}^{\boldsymbol{v}}_n, \hat{\boldsymbol{\phi}}^{\boldsymbol{v}}_n,\ n = 1,\ \cdots,\ \mathrm{N}_{max}\right\},$$

$$Z_{\boldsymbol{v}_{\mathrm{N}}} \oplus \mathcal{T}^{\boldsymbol{w}}_{\mathrm{N}} = span\left\{\tilde{\boldsymbol{\zeta}}^{\boldsymbol{w}}_n, \hat{\boldsymbol{\zeta}}^{\boldsymbol{w}}_n,\ n = 1,\ \cdots,\ \mathrm{N}_{max}\right\}.$$

Furthermore, to satisfy Brezzi's theorem at reduced order level, we need to ensure $S_{\mathrm{N}} \equiv Z_{\mathrm{N}}$. Considering aggregation of spaces, we can define the supremizer enriched and aggregated reduced order spaces as:

$$S_{\mathrm{N}} = (V_{\mathrm{N}} \oplus \mathcal{T}^{\boldsymbol{v}}_{\mathrm{N}}) \times P_{\mathrm{N}} \times (Z_{\boldsymbol{v}_{\mathrm{N}}} \oplus \mathcal{T}^{\boldsymbol{w}}_{\mathrm{N}}) \times Z_{p_{\mathrm{N}}} \equiv Z_{\mathrm{N}},$$

such that the total dimensions of the reduced order spaces are $\mathrm{N} = 13\mathrm{N}_{max} \ll \mathcal{N}$.

Offline-online phase decomposition

We recall that to decouple the reduced order framework into two phases, an expensive and an inexpensive one, we need to make a crucial assumption, namely, affine decomposition. However, in comparison to Stokes constrained optimal flow control problem, in addition to the bilinear functionals, $\mathcal{A}$ and $\mathcal{B}$, we are dealing with the non-linear and trilinear terms, that are given in components form with Einstein summation on the indices i and j, as below:

$$\mathrm{e}\left(\boldsymbol{v}, \boldsymbol{v}, \boldsymbol{\kappa}_{\boldsymbol{w}}; \boldsymbol{\mu}\right) = \int_{\Omega} v_i\left(\boldsymbol{\mu}\right) \frac{\partial v_j\left(\boldsymbol{\mu}\right)}{\partial x_i} \kappa_{w_j}\ d\Omega, \quad \mathrm{e}\left(\mathbf{y}_{\boldsymbol{v}}, \boldsymbol{v}, \boldsymbol{w}; \boldsymbol{\mu}\right) = \int_{\Omega} y_{v_i} \frac{\partial v_j\left(\boldsymbol{\mu}\right)}{\partial x_i} w_j\left(\boldsymbol{\mu}\right)\ d\Omega,$$

$$\mathrm{e}\left(\boldsymbol{v}, \mathbf{y}_{\boldsymbol{v}}, \boldsymbol{w}; \boldsymbol{\mu}\right) = \int_{\Omega} v_i\left(\boldsymbol{\mu}\right) \frac{\partial y_{v_j}}{\partial x_i} w_j\left(\boldsymbol{\mu}\right)\ d\Omega.$$

It is evident that components of the above terms cannot be divided into parameters times the parameter-independent terms, thus the affine decomposition assumption does not hold true in this case. In such a case, one can opt for empirical interpolation methods to approximate the parameter dependent terms. Another option, which we have opted for

in this work, is to store the non-linear and trilinear terms in third order tensors, which can be assembled from scratch at each iteration. In this way, the rest of the problem still obeys affine assumption and therefore, the computational procedure can be performed in two separate phases with the exception of reassembling the non-linear and trilinear terms from scratch.

3.6. Test cases: parametrized Navier-Stokes constrained optimal flow control problem

Next, we will construct the reduced order spaces for Navier-Stokes constrained optimal flow control problem, applied to Y-shape geometry shown in chapter 2, figure 2.5.1(a). The mesh elements at the boundaries and inside Ω are shown in figures 2.5.1(b) and 2.5.1(c) respectively. We will consider physical parametrization, that is Reynolds number, to study the flow pattern for different inlet flow velocities. Thus, $\boldsymbol{\mu} = Re \in \mathcal{D} = [100, 300]$ defining the velocity at the inlets through the following expression:

$$\boldsymbol{v}_{in} = -\frac{\eta \boldsymbol{\mu}}{R_{in}} \left(1 - \frac{r^2}{R_{in}^2}\right) \boldsymbol{n}_{in}, \tag{3.26}$$

where, η is constant viscosity, R_{in} is the maximum radius of inlets, $\boldsymbol{n}_{in}$ corresponds to outward normals to the inlets Γ_{in} and r is the distance between center of an inlet and corresponding mesh nodes. The problem reads:

Problem 3.10. Given $\boldsymbol{\mu} \in \mathcal{D}$, find $(\boldsymbol{v}, p, \boldsymbol{u})$ such that the following objective functional is minimized

$$\mathcal{J}(\boldsymbol{v}, \boldsymbol{u}; \boldsymbol{\mu}) = \frac{1}{2} |\, \boldsymbol{v}(\boldsymbol{\mu}) - \boldsymbol{v}_o\|^2_{L^2(\Omega)} + \frac{\alpha}{2} \|\boldsymbol{u}(\boldsymbol{\mu})\|^2_U \tag{3.27}$$

subject to the constraints (3.19).

Here, $\boldsymbol{v}_o$ is desired velocity, distributed across Ω through equation (2.45) with $v_{const} = mm/s$. At the continuous level, we consider the following spaces at continuous level:

$$V(\Omega) = \left[H^1_\Gamma(\Omega)\right]^3 := \left\{ \boldsymbol{v} \in \left[H^1(\Omega)\right]^3 \mid \boldsymbol{v}|_{\Gamma_{in}} = \boldsymbol{v}_{in} \wedge \boldsymbol{v}|_{\Gamma_w} = \boldsymbol{0} \right\},$$

$$P(\Omega) = L^2(\Omega), \qquad U(\Gamma_o) = \left[L^2(\Gamma_o)\right]^3.$$

We sample a training set Λ of 100 parameter values, and snapshots are collected by solving discretized problem 3.7 for $\boldsymbol{\mu} \in \Lambda$. Results for a single value of parameter, for example, $\mu = 140$ are shown in chapter 2, section 2.5.5. As discussed, the Galerkin finite element problem has dimensions $\mathcal{N} = 152501$ for each parameter, and takes computational time of 371.6 seconds. The offline phase starts with snapshots collection, where, the Galerkin finite element problem is solved 100 times. In figure 3.6.1, we show the eigenvalues in a decreasing

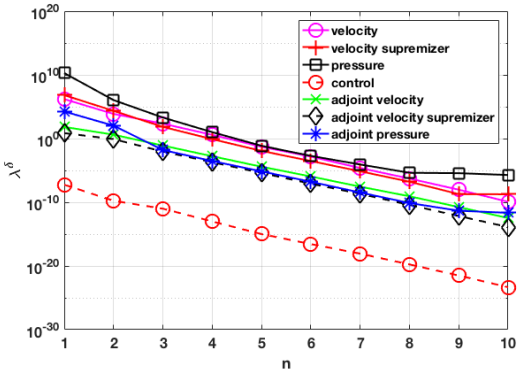

Figure 3.6.1: Eigenvalues reduction for Navier-Stokes constrained optimal flow control problem

order on a logarithmic scale for N_{max} modes. It can be seen that for $\mathrm{N}_{max} = 10 \ll |\Lambda|$ POD modes, the energy captured by the arranged eigenvalues for state velocity is decreased from $\mathcal{O}\left(10^{11}\right)$ to approximately $\mathcal{O}\left(10^{-5}\right)$. Thus, 10 eigenvalues successfully capture 99.9 % energy of the snapshots.

Thus, the reduced order spaces are generated from corresponding eigenvectors and the total dimension of reduced order problem is $\mathrm{N} = 13\mathrm{N}_{max} = 130 + 1$, where an additional basis is for the lifting for non-homogenuous Dirichlet conditions at the inlets. Furthermore in figure 3.6.2, we report the controlled velocity and the control achieved by the reduced order problem, where the former is attained using 41 reduced bases and the latter is attained using 10 reduced bases, in comparison to $\mathcal{N} = \mathcal{O}\left(10^5\right)$. It can be seen that from the figures 3.6.2(a) and 3.6.2(b), that the solution approximated by using reduced order spaces is almost the same as the Galerkin finite element solution, thus, we can claim that our reduced order framework retains the reliability of the high order methods.

We also verify this claim through the error plots shown in figures 3.6.3(a) and 3.6.3(b). Figure 3.6.3(a) shows the plot of error calculated for each solution variable using the following norms, on a logarithmic scale:

$$\mathcal{E}_{\boldsymbol{s}} = \|\boldsymbol{s}_h\left(\boldsymbol{\mu}\right) - \boldsymbol{s}_{\mathrm{N}}\left(\boldsymbol{\mu}\right)\|_{S(\Omega)}, \quad \mathcal{E}_{\boldsymbol{z}} = \|\boldsymbol{z}_h\left(\boldsymbol{\mu}\right) - \boldsymbol{z}_{\mathrm{N}}\left(\boldsymbol{\mu}\right)\|_{Z(\Omega)}, \quad \mathcal{E}_{\boldsymbol{u}} = \|\boldsymbol{u}_h\left(\boldsymbol{\mu}\right) - \boldsymbol{u}_{\mathrm{N}}\left(\boldsymbol{\mu}\right)\|_{U(\Gamma_o)}, \tag{3.28}$$

and the figure 3.6.3(b) shows the total average and relative errors and their attained max-

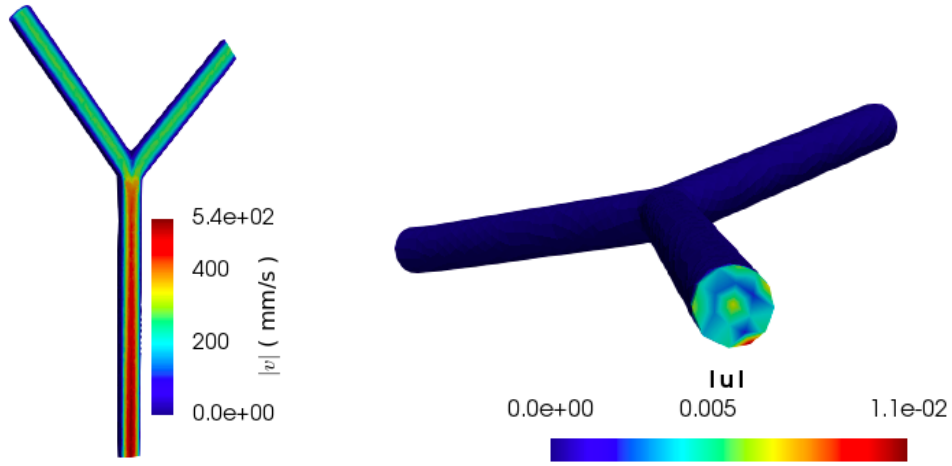

(a). (b).

Figure 3.6.2: (a). Controlled velocity achieved by POD–Galerkin for $\mu = 140$. (b). Control magnitude achieved by POD–Galerkin for $\mu = 140$.

ima on the logarithmic scale, calculated through the following expression:

$$\mathcal{E}_{\boldsymbol{s}_{rel}} = \frac{\mathcal{E}_{\boldsymbol{s}}}{\|\boldsymbol{s}_h\|_{S(\Omega)}},\ \mathcal{E}_{\boldsymbol{z}_{rel}} = \frac{\mathcal{E}_{\boldsymbol{z}}}{\|\boldsymbol{z}_h\|_{Z(\Omega)}},\ \mathcal{E}_{\boldsymbol{u}_{rel}} = \frac{\mathcal{E}_{\boldsymbol{u}}}{\|\boldsymbol{u}_h\|_{U(\Gamma_o)}}, \tag{3.29}$$

$$\mathcal{E}_T = \left(\mathcal{E}_{\boldsymbol{s}}^2 + \mathcal{E}_{\boldsymbol{z}}^2 + \mathcal{E}_{\boldsymbol{u}}^2\right)^{1/2}, \tag{3.30}$$

$$\mathcal{E}_{T_{rel}} = \frac{\mathcal{E}_T}{\left(\|\boldsymbol{s}_h\|_{S(\Omega)}^2 + \|\boldsymbol{u}_h\|_{U(\Gamma_o)}^2 + \|\boldsymbol{z}_h\|_{Z(\Omega)}^2\right)^{1/2}}, \tag{3.31}$$

It is evident from the plots that through reduced order framework, using 10 POD modes for each solution variable and the supremizers and correspondingly attaining 131 reduced basis, we get the errors in velocity and pressure approximations to be reduced from $\mathcal{O}\left(10^1\right)$ to about $\mathcal{O}\left(10^{-6}\right)$ and from $\mathcal{O}\left(10^3\right)$ to about $\mathcal{O}\left(10^{-5}\right)$ respectively. Furthermore, the maximum relative error for the solution variables is $\mathcal{O}\left(10^{-1}\right)$ and is decreased to $\mathcal{O}\left(10^{-7}\right)$ as the POD modes are increased from $n = 1$ to $n = \mathrm{N}_{max}$.

Furthermore, we calculate the difference between Galerkin finite element and POD–Galerkin approximations of objective functional $\mathcal{J}$ as below:

$$\mathcal{E}_{\mathcal{J}} = |\mathcal{J}\left(\mathbf{x}_h; \boldsymbol{\mu}\right) - \mathcal{J}\left(\mathbf{x}_{\mathrm{N}}; \boldsymbol{\mu}\right)|, \tag{3.32}$$

and report it in figure 3.6.4 for 6 POD modes as afterwards the objective functional approximated by both Galerkin finite element and POD–Galerkin methods is exactly the same.

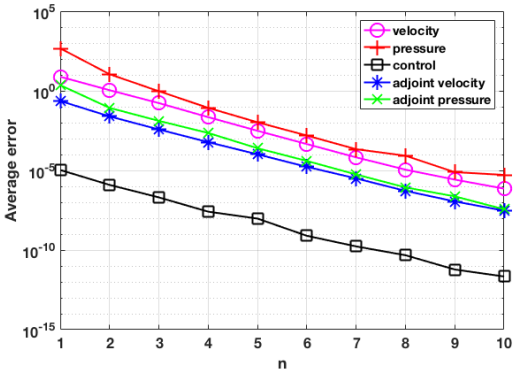

(a).

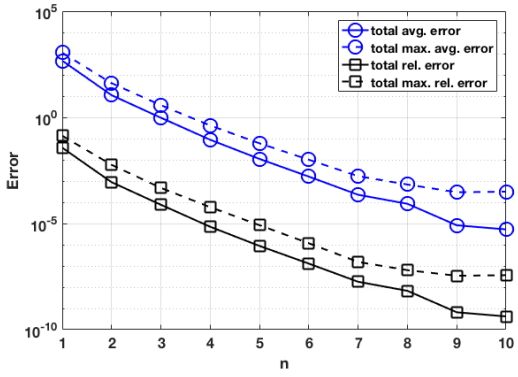

(b).

Figure 3.6.3: (a). Average error between FE and POD–Galerkin approx. of $\boldsymbol{\delta} = \boldsymbol{v}, p, \boldsymbol{u}, \boldsymbol{w}, q$. (b). Absolute average error and absolute relative error between Galerkin FE and POD–Galerkin approximations.

Mesh size	15901
$\mathcal{D}$	$[60, 140]$
$\lvert\Lambda\rvert$	100
No. of reduced bases N	131
Offline phase	6714 seconds
Online phase	33 seconds

(a).

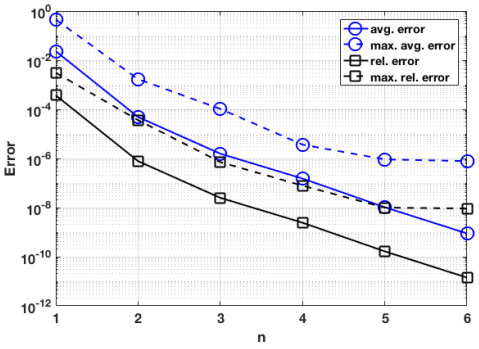

(b).

Figure 3.6.4: (a). Table demonstrating computational performance of POD–Galerkin for Navier-Stokes constrained optimal control problem. (b). Error between FE and POD–Galerkin reduction of $\mathcal{J}$ for Navier-Stokes constrained optimal control problem.

Concluding remarks

In this chapter, we have introduced the parametrized version of optimal flow control problem constrained by Stokes equations and Navier-Stokes equations. Then, we have reconstructed a reduced order framework based upon POD–Galerkin and we make a few remarks on the framework, as below:

(*i*) Our solution approach has been *optimize-discretize-reduce*, thus the reduced order framework constructed in this chapter takes in the full order solutions, that are *snapshots*, as the building blocks.

(*ii*) The nested saddle-point structure of the optimal flow control problem and hence, the resulting block structure of the algebraically defined optimality system are preserved in the reduced order problem.

(*iii*) We remark that to attain a unique and stable reduced order solution, one has to satisfy both LBB inf-sup condition and Brezzi's inf-sup condition at the reduced order level. However, to ensure that the construction of reduced order spaces is correct and is done without any pollutant, we have to satisfy the aforementioned conditions at the snapshots level too.

(*iv*) We have shown the numerical results in for Stokes and Navier-Stokes constrained optimal flow control problems in sections 3.3 and 3.6, respectively. It is to be noted that these numerical results show reduction in the dimensions of the spaces from $\mathcal{O}\left(10^4\right)$ to $\mathcal{O}\left(10^2\right)$ and reduction in the computational time of atleast $\mathcal{O}\left(10^1\right)$ seconds.

(*v*) Lastly, we remark that the numerical results show the offline phase to be computationally expensive, however, it is justifiable since the computational cost of this phase depends upon cardinality of sampled training set, the cost of high order solutions and in case of Navier-Stokes state constraints, it also depends upon the cost of reassembly of the non-linear and trilinear operators from scratch and also upon the cost of iterative numerical methods for non-linear PDEs-dependent problems.

We reiterate the offline phase, although being costly, needs to carried out only once and thanks to the reduced order spaces, for tuning different parameters we only need to repeat the online phase with computational cost much lower than both the offline phase and the high order methods. In the next chapter, we will extend the application of this framework to cardiovascular problems discussed in chapter 2.

Chapter 4

Applications of reduced order parametrized optimal flow control problems to patient-specific coronary artery bypass grafts

***

In this chapter we will extend application of the reduced order model for parameterized optimal flow control problems, constructed in chapter 3, to the cardiovascular problems introduced in chapter 2. The aim of this chapter is to address the challenge of high computational cost arising from implementation of full order methods only in parametrized settings, in patient-specific hemodynamics modeling. In the discussion henceforth, we will first recall the clinical case, introduced in chapter 1 and afterwards, we will re-solve the numerical optimal flow control problem, shown in chapter 2 section 2.6, in the reduced order framework for different parameter-dependent scenarios. Furthermore, we will make the comparisons between the implementation of high order and reduced order methods, regarding the computational cost and we will show that in the implementation of the proposed reduced order optimal flow control framework, we retain the accuracy of high order numerical methods.

4.1. Clinical case: an overview; aims and objectives

In this section, we will recall the clinical case of triple coronary artery bypass graft surgery performed in Sunnybrook Health Sciences Centre, Toronto, Canada. *Triple* in the previous sentence is indicative of the surgery been performed to restore blood supply to the cardiac muscle from three different stenosed arteries that include left anterior descending artery

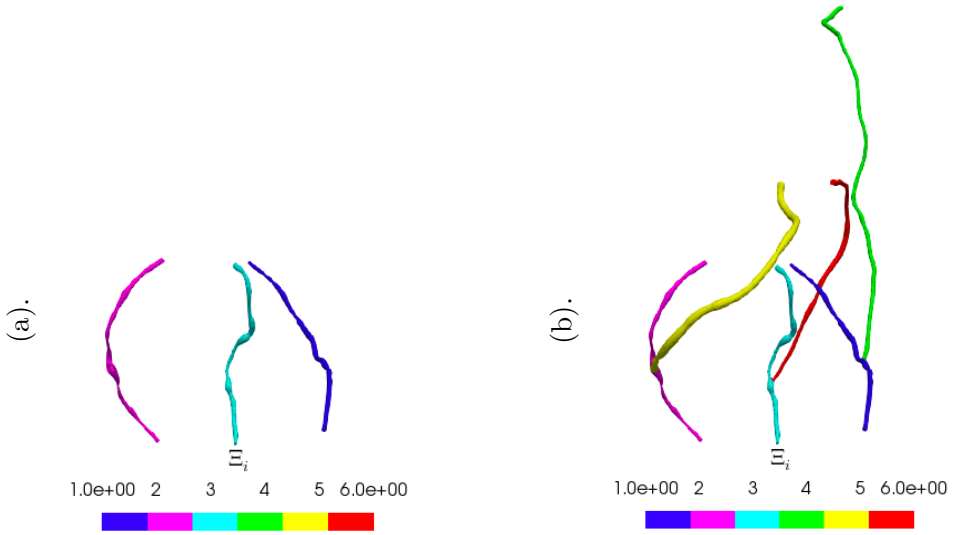

Figure 4.1.1: (a). Stenosed coronary arteries: left anterior descending artery (LAD) (dark blue, Ξ_1), first obtuse marginal artery (OM1) (light blue, Ξ_3) and posterior descending artery (PDA) (magenta, Ξ_2). (b). Grafted vessels: right internal mammary artery (RIMA) (green, Ξ_4) grafted to LAD, saphenuous vein (SV) (red, Ξ_6) grafted to OM1 and saphenuous vein (SV) (yellow, Ξ_5) grafted to PDA.

(LAD), first obtuse marginal artery (OM1) and posterior descending artery (PDA), shown in figure 4.1.1(a), marked with different colors and symbols $\Xi_i,\ i = 1, 2, 3$. Consequently, the surgeon has made three graft connections using right internal mammary artery (RIMA) and saphenuous vein (SV) to the blocked arteries separately. We mark these newly connected vessels with $\Xi_i,\ i = 4, 5, 6$ as shown in figure 4.1.1(b) and we remark that the geometries in figure 4.1.1 are reconstructed from the CT-scan for corresponding case, following the algorithm discussed in chapter 1.

From a mathematical point of view, presumably if in-vivo physiological measurements are made using modern imaging techniques, such as 4D flow cardiovascular magnetic resonance imaging technique, then it can be of interest to match these physiological measurements through computational hemodynamics models in corresponding patient-specific cardiovascular geometries. However, as discussed earlier, the accuracy of the numerical models relies on the quantification of boundary conditions. Although surrogate models are extensively being used to approximate the boundary conditions [85, 86, 101], they are usually complicated and require manual tuning of parameters until results with user-desired accuracy are attained [96, 95, 89]. Therefore, in this work we have been interested in implementation of such a framework in computational hemodynamics modeling that can tune the boundary conditions required to match patient-specific physiological data, in an

automated manner. In chapter 2, we have shown construction of such a framework and its applications to patient-specific coronary artery bypass grafts. For the sake of simplicity, we have relied on Neumann boundary conditions.

Furthermore, another challenge in the numerical modeling of hemodynamics in patient-specific cardiovascular volumes is the high computational cost, arising from sufficiently fine mesh size; a requirement for stability and accuracy of the numerical techniques, and from required repeated computations in parametrized settings. To deal with this issue, we have shown a reduced order framework based upon POD–Galerkin in chapter 3 and have verified the reduction in computational cost through its applications to idealized geometries. Moreover, we have shown that these methods retain the accuracy offered by high order numerical methods in simple 2-dimensional and 3-dimensional idealized geometrical cases.

In the discussion henceforth, we will consider different inflow velocity scenarios generated by tuning Reynolds number and will try to match the desired velocity with the resulting reduced order simulation velocity in patient-specific coronary artery bypass grafts. The control in this case is imposed to automatically tune the required outflow conditions. Furthermore, we will study this problem in three different geometries, comprising of single graft connections and double graft connections. We remark that these geometries are sub-geometries of the $\cup_i \Xi_i,\ i = 1,\ \cdots,\ 6$ (see figure 4.1.1(b)), reconstructed from the case of triple coronary artery bypass graft surgery.

4.2. Stokes constrained optimal flow control: single graft connection

In the first numerical test, we consider the single graft connection, between right internal mammary artery (RIMA) and left anterior descending artery (LAD) and label it by Ω_a (see figure 2.6.1(a)). Moreover, we will solve the Stokes constrained optimal flow control problem, demonstrated in chapter 2 section 2.6.1, with POD–Galerkin and we will illustrate the speedup achieved by the reduced order framework. The continuous problem definition is given in problem 3.1.

Furthermore, we consider v_{const}, magnitude of the desired velocity to be 350 mm/s and $\boldsymbol{v}_o$ to be distributed across Ω_a through expression (2.52). The parametrization is considered the velocity profile at the inlets Γ_{in} of Ω_a, defined by the following expression:

$$\boldsymbol{v_{in}}(\boldsymbol{\mu}) = -\frac{\eta \boldsymbol{\mu}}{R_{in}} \left(1 - \frac{r^2}{R_{in}^2}\right) \boldsymbol{n}_{in}, \quad \boldsymbol{\mu} \in \mathcal{D}. \tag{4.1}$$

Here the parameter $\boldsymbol{\mu} \in \mathcal{D}$ is considered to be physical, and more specifically to be Reynolds number, that is, $\boldsymbol{\mu} = Re \in \mathcal{D} = [70, 80]$. Thus, this test case will match Stokes velocity $\boldsymbol{v}$ with the desired velocity $\boldsymbol{v}_o$ for different dfferent inflow velocities $\boldsymbol{v_{in}}$ generated by tuning of Re. Moreover, control is the flux or the energy per unit length at the outlets Γ_o.

The velocity, pressure and control solution spaces at the continuous level are given below:

$$V(\Omega_a) = H^1_{\Gamma_{in} \cup \Gamma_w}(\Omega_a) = \left[\boldsymbol{v} \in \left[H^1(\Omega_a)\right]^3 : \boldsymbol{v}|_{\Gamma_{in}} = \boldsymbol{v_{in}} \text{ and } \boldsymbol{v}|_{\Gamma_w} = \boldsymbol{0}\right],$$

Mesh size	42354
$\mathcal{D}$	$[70, 80]$
$\lvert\Lambda\rvert$	100
Offline phase	4191.32 seconds
Online phase	6.4 seconds

Table 4.1: (a).

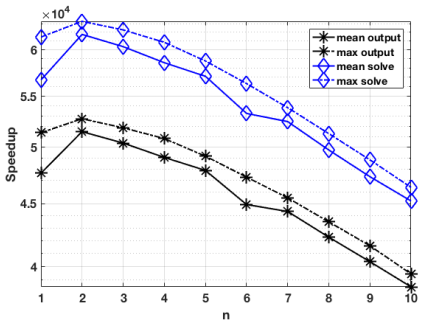

(b).

Figure 4.2.1: (a). Table demonstrating computational performance of POD–Galerkin for Stokes constrained optimal control problem. (b). Mean and maximum speedups for solution and objective functiona— achieved by POD–Galerkin for Stokes constrained optimal control problem.

$$P(\Omega_a) = L^2(\Omega_a), \text{ and } \quad U(\Gamma_o) = \left[L^2(\Gamma_o)\right]^3.$$

In the implementation of POD–Galerkin, we randomly sample $\boldsymbol{\Lambda} \subset \mathcal{D}$ such that $\boldsymbol{\Lambda}$ contains 100 parameter values. The offline phase consists of snapshots construction for these parameter values by solving *truth problem*, that is the system (3.8), through Galerkin finite element method. At this level, stable $\mathbb{P}2 - \mathbb{P}1$ pair for state and adjoint velocity and pressure and $\mathbb{P}2$ for control are used. We remark that with the use of equivalent state and adjoint spaces and the Taylor-Hood pair for velocity and pressure, we guarantee the satisfaction of Brezzi's inf-sup condition and LBB inf-sup condition. The offline phase ends with the construction of reduced order bases using $\mathrm{N}_{max} = 10$ POD modes and takes 4191.32 seconds (see table 4.2.1(a)).

We remark that at the reduced order level, to satisfy Brezzi's inf-sup condition and LBB inf-sup condition, we take the supremizers enriched and aggregated state and adjoint spaces. The online phase comprises of solving the reduced order problem (3.13) for different values of $\boldsymbol{\mu}$ chosen from $\mathcal{D}$ and takes only 6.4 seconds each time.

We illustrate average and maximum speedups attained in this case through figure 4.2.1(b). An average speedup of $\mathcal{O}(10^4)$ is achieved for both, the output objective functional $\mathcal{J}$ and solution variables $\boldsymbol{\delta} = \boldsymbol{v}, p, \boldsymbol{u}, \boldsymbol{w}, q$, as n goes from 1 to N_{max}, with the maximum speedups falling in the same range. Furthermore, in this case, we report the relative error for POD–Galerkin approximations of state velocity, state pressure and control to be $\mathcal{O}(10^{-5})$, $\mathcal{O}(10^{-7})$ and $\mathcal{O}(10^{-2})$ respectively.

4.3. Navier-Stokes constrained optimal flow control problem

In this section, we will solve the numerical experiments dealing with Navier-Stokes constrained optimal flow control, shown in chapter 2 section 2.6.3, through POD–Galerkin. We will deal with the three different geometries shown in figure 2.6.1 and we will divide these numerical tests into three sub-cases accordingly. Furthermore, in all these numerical tests we will match Navier-Stokes velocity with the desired velocity with magnitude $v_{const} = 350\ mm/s$, defined by the following equation:

$$\boldsymbol{v_o} = v_{const}\left(1 - \frac{r^2}{R_i^2}\right)\boldsymbol{t}_{c_i},\ i \in \{1, 2\}, \tag{4.2}$$

where R_i denotes maximum radius of a vessel, $\boldsymbol{t}_{c_i}$ denote the tangents to the points of centerline of a vessel, in the axial direction and r is the distance between mesh nodes and nearest point on the centerline of a vessel. Moreover, in these numerical tests the error plots will be shown on the logarithmic scale and will be calculated through the expressions given below.

Average error for the variables $\boldsymbol{\delta} = \boldsymbol{s} = (\boldsymbol{v}, p), \boldsymbol{u}, \boldsymbol{z} = (\boldsymbol{w}, q)$ is defined as:

$$\mathcal{E}_{\boldsymbol{s}} = \|\boldsymbol{s}_h(\boldsymbol{\mu}) - \boldsymbol{s}_{\mathrm{N}}(\boldsymbol{\mu})\|_{S(\Omega)}, \quad \mathcal{E}_{\boldsymbol{z}} = \|\boldsymbol{z}_h(\boldsymbol{\mu}) - \boldsymbol{z}_{\mathrm{N}}(\boldsymbol{\mu})\|_{Z(\Omega)}, \quad \mathcal{E}_{\boldsymbol{u}} = \|\boldsymbol{u}_h(\boldsymbol{\mu}) - \boldsymbol{u}_{\mathrm{N}}(\boldsymbol{\mu})\|_{U(\Gamma_o)}, \tag{4.3}$$

absolute average error and absolute relative error for the variables are calculated by the following equations:

$$\mathcal{E}_{\boldsymbol{s}_{rel}} = \frac{\mathcal{E}_{\boldsymbol{s}}}{\|\boldsymbol{s}_h\|_{S(\Omega)}},\ \mathcal{E}_{\boldsymbol{z}_{rel}} = \frac{\mathcal{E}_{\boldsymbol{z}}}{\|\boldsymbol{z}_h\|_{Z(\Omega)}},\ \mathcal{E}_{\boldsymbol{u}_{rel}} = \frac{\mathcal{E}_{\boldsymbol{u}}}{\|\boldsymbol{u}_h\|_{U(\Gamma_o)}}, \tag{4.4}$$

$$\mathcal{E}_T = \left(\mathcal{E}_{\boldsymbol{s}}^2 + \mathcal{E}_{\boldsymbol{z}}^2 + \mathcal{E}_{\boldsymbol{u}}^2\right)^{1/2}, \tag{4.5}$$

$$\mathcal{E}_{T_{rel}} = \frac{\mathcal{E}_T}{\left(\|\boldsymbol{s}_h\|_{S(\Omega)}^2 + \|\boldsymbol{u}_h\|_{U(\Gamma_o)}^2 + \|\boldsymbol{z}_h\|_{Z(\Omega)}^2\right)^{1/2}}, \tag{4.6}$$

and difference between the output for $\mathcal{J}$ achieved by Galerkin finite element method and POD–Galerkin method is defined as:

$$\mathcal{E}_{\mathcal{J}} = |\mathcal{J}(\mathbf{x}_h; \boldsymbol{\mu}) - \mathcal{J}(\mathbf{x}_{\mathrm{N}}; \boldsymbol{\mu})|. \tag{4.7}$$

4.3.1 Case I(a): single graft connection

In the first example, we will consider the graft connection between right internal mammary artery (RIMA) and left anterior descending artery (LAD). The geometry is extracted from the triple coronary artery bypass grafts surgery case and it is shown in figure 2.6.1(a). We

label the geometry with Ω_a and consider the inlets of both RIMA and LAD as Γ_{in} such that the blood flow is in the downstream direction. Moreover, we consider the physical parametrization, $\boldsymbol{\mu} = Re|_{\Gamma_{in}} \in \mathcal{D} = [70, 80]$ in inlet velocity profile, defined as below:

$$\boldsymbol{v}_{in} = -\frac{\eta \boldsymbol{\mu}}{R_{in}} \left(1 - \frac{r^2}{R_{in}^2}\right) \boldsymbol{n}_{in}. \tag{4.8}$$

Here, R_{in} is the maximum radius of an inlet, r is the distance between mesh nodes of the inlet and corresponding center and $\boldsymbol{n}_{in}$ denotes outward normal to the inlet. With Navier-Stokes state equations, the mathematical problem is given by problem 3.5 and at the continuous level we consider the following solution spaces:

$$V(\Omega_a) = \left[H^1_{\Gamma_{in} \cup \Gamma_w}(\Omega_a)\right]^3 := \left\{ \boldsymbol{v} \in \left[H^1(\Omega_a)\right]^3 \mid \boldsymbol{v}|_{\Gamma_{in}} = \boldsymbol{v}_{in} \wedge \boldsymbol{v}|_{\Gamma_w} = \boldsymbol{0} \right\},$$

$$P(\Omega_b) = L^2(\Omega_a), \quad \text{and} \quad U(\Gamma_o) = \left[L^2(\Gamma_o)\right]^3.$$

We randomly sample training set Λ of 100 parameters and start the offline phase of POD–Galerkin by collecting the snapshots. The snapshots in this case are the solution of the Galerkin finite element optimality system (2.48) for all $\boldsymbol{\mu} \in \Lambda$ (see figure 4.3.1). At this level, we utilize $S_h = \mathbb{P}2 - \mathbb{P}1 \equiv Z_h$ for state and adjoint velocity and pressure respectively and $U_h = \mathbb{P}2$ for control. Thus, at the snapshots level the fulfillment of LBB inf-sup condition (2.42) is guaranteed and thanks to the equivalence between state and adjoint finite element spaces, Brezzi's inf-sup condition (see theorem 2.7(ii)) is fulfilled too at this level. Therefore, the stability of the snapshots is ensured and we illustrate it for a few snapshots of state velocity and control for $\mu = 72.923$, 75.073 and $\mu = 78.527$ in figure 4.3.1. We have seen in section 2.6 case I(a) (see table 2.2(case I(a))), that one snapshot in this case takes 1214.3 seconds. Furthermore, we reiterate that the non-linear optimality system 2.48 is solved through Newton method for each snapshot.

The POD bases are constructed by solving the eigenvalue problems (3.9) for the collected snapshots. We report 8 eigenvalues in decreasing order in figure 4.3.2. It is evident that 6 eigenvalues successfully capture 99.9 % energy of the snapshots, thus we can discard the rest. From $\mathrm{N}_{max} = 6$ POD modes, we generate the supremizer enriched and aggregated reduced spaces comprising of 79 reduced bases in total, subdivided into 24 bases each for state and adjoint velocity, 12 reduced bases each for state and adjoint pressure, 6 reduced bases for control and 1 basis corresponds to the lifting function for non-homogenuous inlet Dirichlet conditions. We remark the Brezzi's inf-sup condition (see theorem 3.2) and LBB inf-sup condition (see equation (3.14)) are satisfied by the reduced order spaces constructed in this way. This phase ends with the construction of reduced order spaces and requires total CPU time of $16,825.9$ seconds.

For the online phase, we take $\mu = 80$ and solve the reduced order optimality system given by equations (3.24) using Newton method. This phase takes 109.3 seconds only and

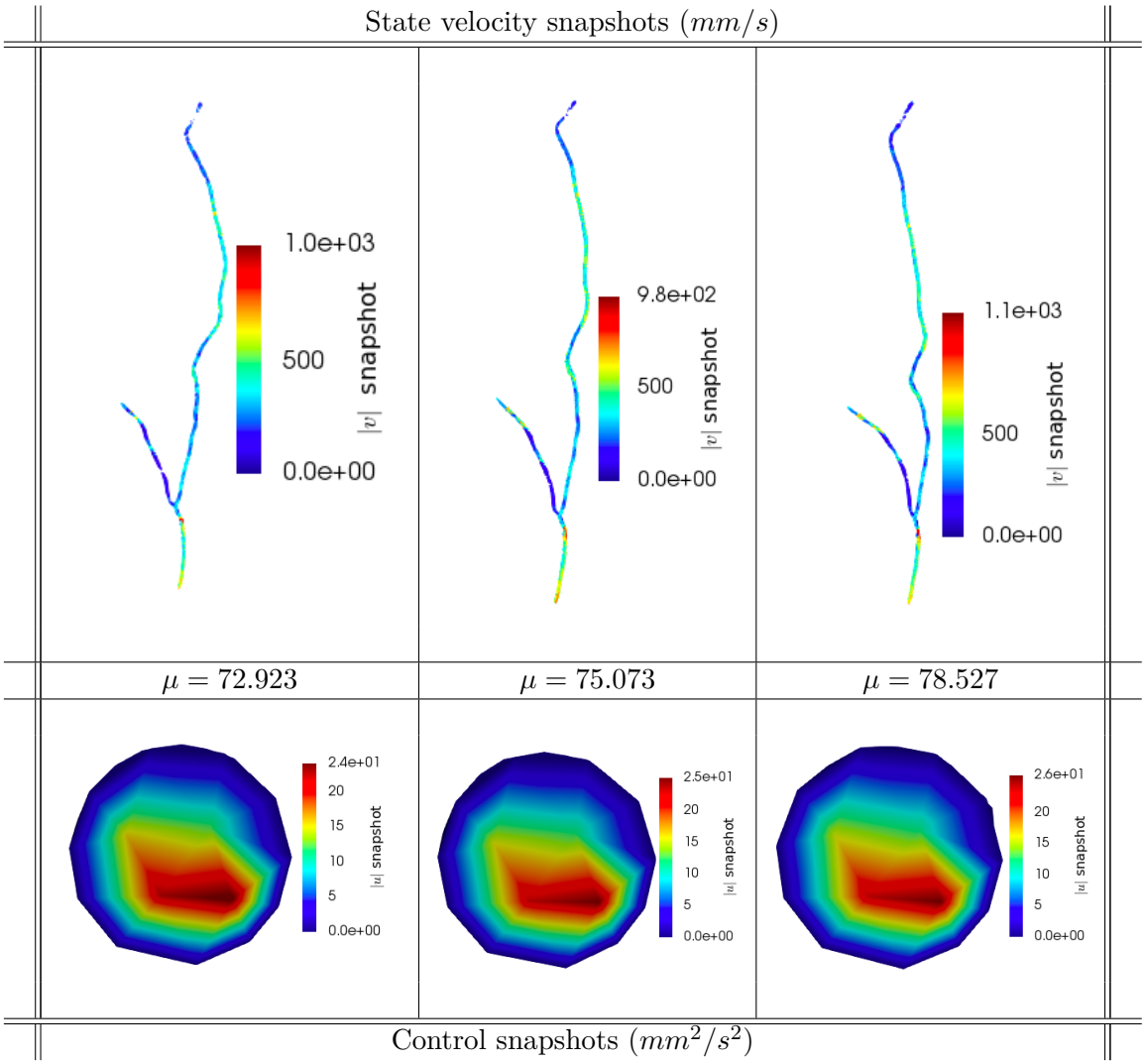

Figure 4.3.1: Case I(a): Snapshots of state velocity and boundary control magnitude for $\mu = 72.923$, $\mu = 75.073$ and $\mu = 78.527$ (from left to right).

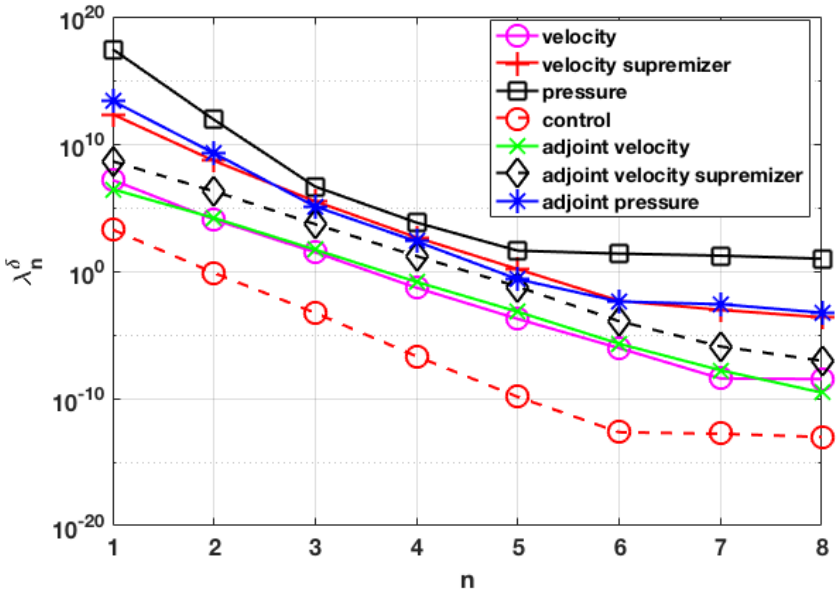

Figure 4.3.2: Case I(a): eigenvalues reduction

the reduced order controlled velocity and boundary control are generated from 49 and 6 reduced bases respectively. We report the reduced order controlled velocity and boundary control in figures 4.3.3(a) & (b), respectively. The full order approximations of controlled velocity and boundary control for $\mu = 80$, using 433288 degrees of freedom, are reported in figure 2.6.4 case I(a)(b) & case I(a)(c), respectively. It is evident that both Galerkin finite element solution and POD–Galerkin solution match each other, hence the accuracy of Galerkin finite element solutions is retained in this case.

In figure 4.3.4(a), we report the error plots $\mathcal{E}_{\boldsymbol{\delta}}$ for $\boldsymbol{\delta} = \boldsymbol{v}, p, \boldsymbol{u}, \boldsymbol{w}, q$, calculated using equation (4.3). $\mathcal{E}_{\boldsymbol{v}}$ decreases from 10^1 to 10^{-5} approximately, $\mathcal{E}_p$ decreases from 10^6 to 10^{-2} and $\mathcal{E}_{\boldsymbol{u}}$ decreases to 10^{-6} as n goes from 1 to 6. Error reduction for adjoint variables' approximations follows similar pattern as the error reduction for state variables. Absolute average error and absolute relative error are calculated using equations (4.4) – (4.4) and are reported in figure 4.3.4(b). $\mathcal{E}_T$ reduces from approximately 10^6 to 10^{-2} for $n = 1, \cdots, \mathrm{N}_{max}$ with same behavior for maximum $\mathcal{E}_T$. A reduction from 10^{-2} to 10^{-10} is achieved for both $\mathcal{E}_{T_{rel}}$ and maximum $\mathcal{E}_{T_{rel}}$ in this case.

Figure 4.3.4(c) shows the difference between $\mathcal{J}$ computed through full order and reduced order methods. It is calculated using equation (4.7) and a reduction from approximately 10^2 to 10^{-8} is observed with similar behavior for relative error as n increases.

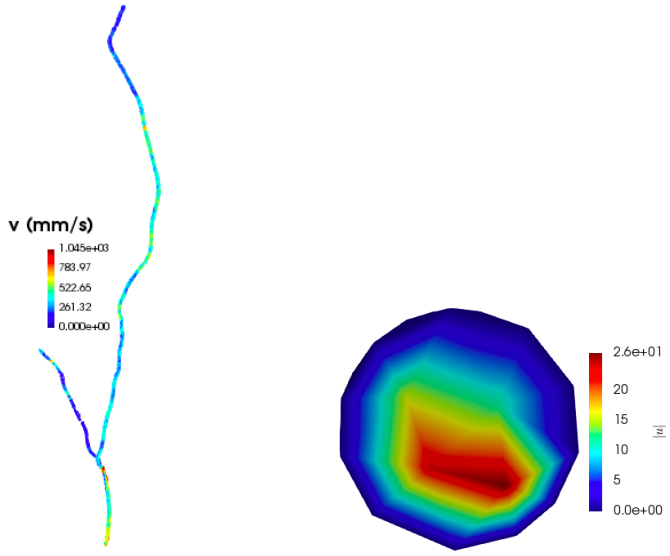

Figure 4.3.3: Case I(a): POD–Galerkin approximation of controlled velocity (mm/s) (left). POD–Galerkin approximation of boundary control (mm^2/s^2) (right).

4.3.2 Case I(b): single graft connection

In the second case, we will consider another subgeometry extracted from the triple coronary artery bypass grafts geometry shown in figure 4.1.1(b) and we will label it by Ω_b. In this case, the graft connection is between saphenuous vein (SV) and first obtuse marginal artery (OM1) (see figure 2.6.1(b)). The parameters in this case are Reynolds number at the inlets of both saphenuous vein and first obtuse marginal artery, which will generate the inlet velocity through the expression (4.8). The mathematical problem is given by problem 3.5 and we consider $V(\Omega_b) = \left[H^1_{\Gamma_{in}\cup\Gamma_w}(\Omega_b)\right]^3 := \left\{\boldsymbol{v} \in \left[H^1(\Omega_b)\right]^3 \mid \boldsymbol{v}|_{\Gamma_{in}} = \boldsymbol{v}_{in} \wedge \boldsymbol{v}|_{\Gamma_w} = \mathbf{0}\right\}$, $P(\Omega_b) = L^2(\Omega_b)$ and $U(\Gamma_o) = \left[L^2(\Gamma_o)\right]^3$ at the continuous level.

In this case $\mathcal{D} = [45, 50]$ and sample a training set Λ of parameters such that $|\Lambda| = 100$. The snapshots are collected by solving problem 3.6 for all $\boldsymbol{\mu} \in \Lambda$ through Newton method. Since at the snapshots level, we are utilizing stable Tayloor-Hood pair for velocity and pressure, we remark that the LBB inf-sup condition will be satisfied at the finite element level. Moreover, we keep $S_h \equiv Z_h$ at this level to ensure Brezzi's inf-sup condition. Thus, the snapshots enclose stable and unique solutions corresponding to $\boldsymbol{\mu} \in \Lambda$ (see figure 4.3.5). We recall that one snapshot calculation in this case takes 634 seconds of CPU time (see table 2.2 case I(b)).

In figure 4.3.6, we show 8 eigenvalues in decreasing order on a logarithmic scale and notice that 6 eigenvalues capture 99.9 % energy of the snapshots, or in other words, full order solutions. Thus, POD bases are constructed from $\mathrm{N}_{max} = 6$ retained eigenvectors

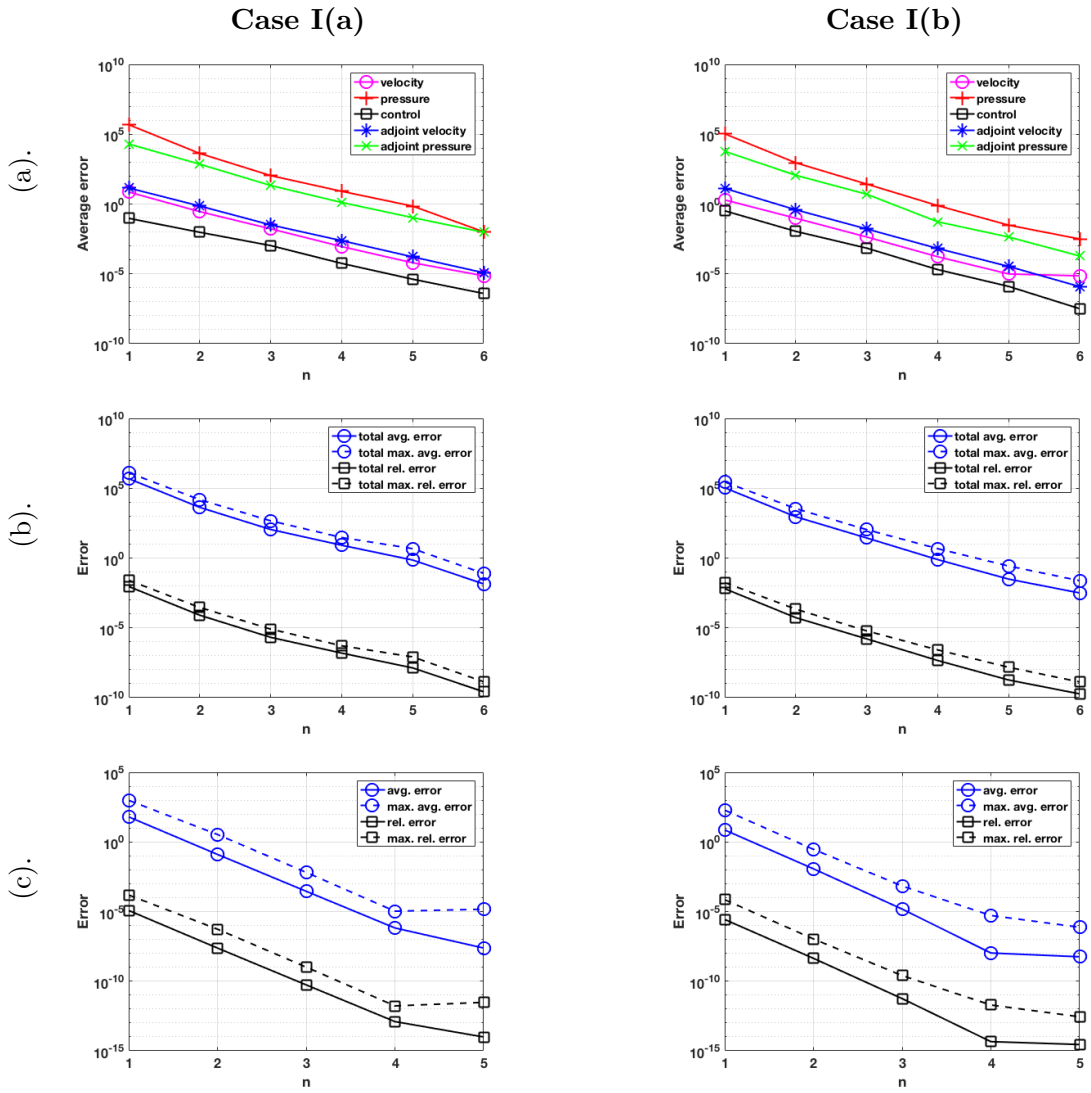

Figure 4.3.4: (a). Average error between FE and POD–Galerkin approx. of $\boldsymbol{\delta} = \boldsymbol{v}, p, \boldsymbol{u}, \boldsymbol{w}, q$. (b). Absolute average error and absolute relative error between Galerkin FE and POD–Galerkin approximations. (c). Error between FE and POD–Galerkin reduction of $\mathcal{J}$.

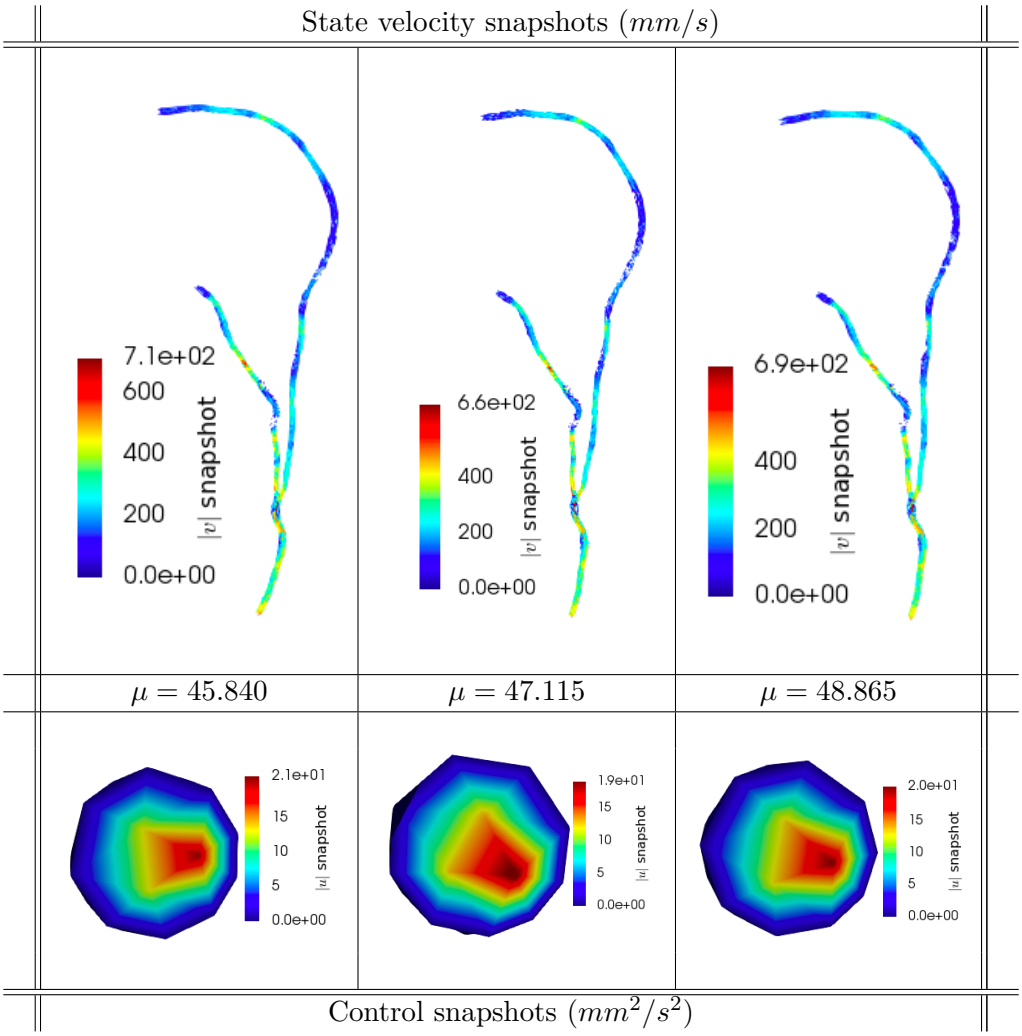

Figure 4.3.5: Case I(b): Snapshots of state velocity (mm/s) and boundary control magnitude (mm^2/s^2) for $\mu = 45.840$, $\mu = 47.115$ and $\mu = 48.865$ (from left to right).

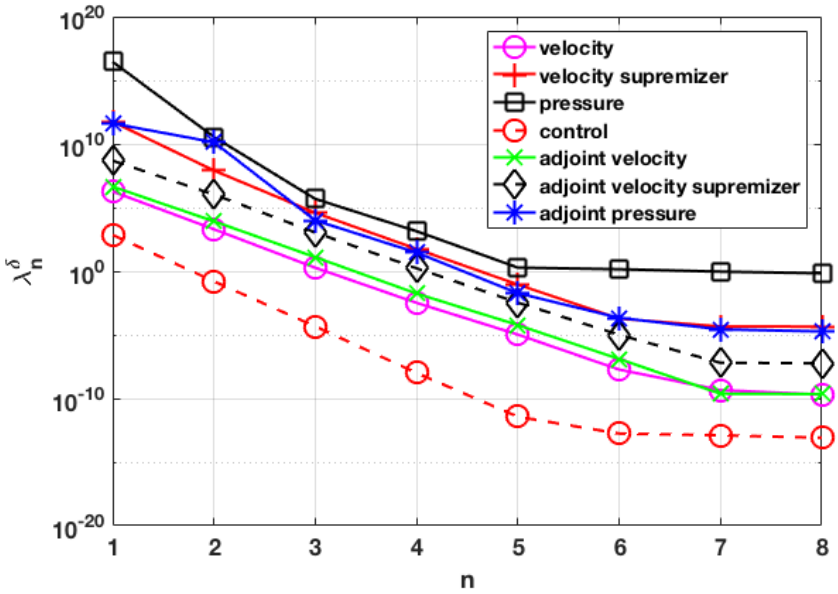

Figure 4.3.6: Case I(b): eigenvalues reduction

and the reduced order spaces comprise of $\mathrm{N}_{\boldsymbol{v}} = 25$, $\mathrm{N}_{\boldsymbol{w}} = 24$, $\mathrm{N}_p = 12$, $\mathrm{N}_q = 12$ and $\mathrm{N}_u = 6$ POD bases. For online $\mu = 50$, the reduced order approximation of state velocity and boundary control are demonstrated in 4.3.7. The Galerkin finite element solution for $\mu = 50$ are shown in figure 2.6.4 case I(b)(b) and figure 2.6.4 case I(b)(c), respectively. Comparing the two solutions we note that they are the same, thus, reduced order framework preserves the accuracy of high order Galerkin finite element methods in this case.

Furthermore, we illustrate the errors in the solution variables $\boldsymbol{v}$, p, $\boldsymbol{u}$, $\boldsymbol{w}$ and q in figure 4.3.4 case I(b)(a). We notice that $\mathcal{E}_{\boldsymbol{v}}$ decreases from 10^1 to approximately 10^{-5} and $\mathcal{E}_p$ decreases from 10^5 to approximately 10^{-3}. The total average and relative errors are calculated through expressions (4.4) – (4.4) and we report that ($\mathcal{E}_T$) decreases from 10^5 to approximately 10^{-3} with same order of reduction observed for total relative error ($\mathcal{E}_{T_{rel}}$) (see figure 4.3.4 case I(b)(b)). The difference between Galerkin finite element and POD–Galerkin approximations of $\mathcal{J}$ is observed to be approximately 10^1 at $n = 1$ and is decreased to 10^{-8} at $n = 5$ (see figure 4.3.4 case I(b)(c)).

4.3.3 Case II: Double graft connections

In this case, we will consider the two geometries shown in the previous examples combined as one geometry (see figure 2.6.1 (c) for details). Here, by combined, we mean that the mathematical problem will be solved on all the mesh nodes, constituting the two coronary

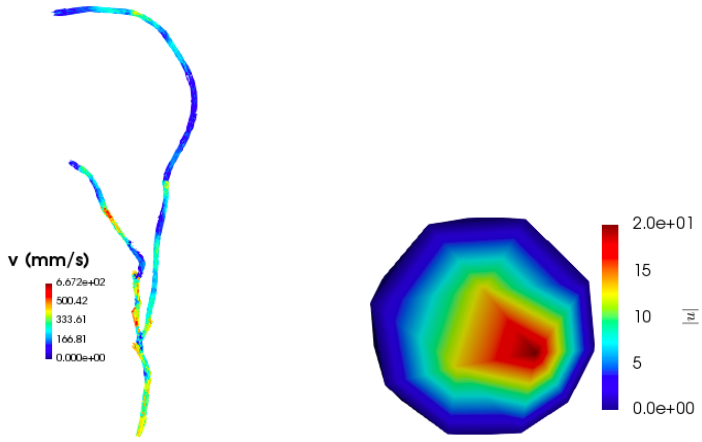

Figure 4.3.7: Case I(b): POD–Galerkin approximation of controlled velocity (mm/s) (left). (b). POD–Galerkin approximation of boundary control (mm^2/s^2) (right).

artery bypass grafts altogether. Thus, the graft connections are between left anterior descending artery (LAD) and right internal mammary artery (RIMA), and between first obtuse marginal artery (OM1) and saphenuous vein (SV). As discussed in case II in chapter 2 section 2.6, we will label the inlets of right internal mammary artery (RIMA) and left anterior descending artery (LAD) as Γ_{in_1} and the inlets of saphenuous vein (SV) and first obtuse marginal artery (OM1) as Γ_{in_2}. Similarly respective outlets are marked as Γ_{o_1} and Γ_{o_2}. We consider two physical parameters $(\boldsymbol{\mu}_1, \boldsymbol{\mu}_2)$, both being Reynolds numbers, that is, $\boldsymbol{\mu} = (\mu_1, \mu_2) = \left(Re|_{\Gamma_{in_1}}, Re|_{\Gamma_{in_2}}\right) \in [70, 80] \times [45, 50]$ appearing in velocity profiles being defined at inlets. Moreover, we consider following solution spaces for the velocity, pressure and control variables respectively at the continuous level:

$$V(\Omega_c) = H^1_{\Gamma_{in_1} \cup \Gamma_{in_2} \cup \Gamma_w}(\Omega_c) = \left[\boldsymbol{v} \in \left[H^1(\Omega_c)\right]^3 : \boldsymbol{v}|_{\Gamma_{in_1}} = \boldsymbol{v_{in}}_1,\ \boldsymbol{v}|_{\Gamma_{in_2}} = \boldsymbol{v_{in}}_2 \text{ and } \boldsymbol{v}|_{\Gamma_w} = \mathbf{0}\right],$$

$$P(\Omega_c) = L^2(\Omega_c), \quad \text{and} \quad U(\Gamma_{o_1} \cup \Gamma_{o_2}) = \left[L^2(\Gamma_{o_1} \cup \Gamma_{o_2})\right]^3.$$

Here,

$$\boldsymbol{v_{in}}_1(\boldsymbol{\mu}_1) = -\frac{\eta \boldsymbol{\mu}_1}{R_{in_1}}\left(1 - \frac{r^2}{R^2_{in_1}}\right)\boldsymbol{n}_{in_1}, \qquad \boldsymbol{v_{in}}_2(\boldsymbol{\mu}_2) = -\frac{\eta \boldsymbol{\mu}_2}{R_{in_2}}\left(1 - \frac{r^2}{R^2_{in_2}}\right)\boldsymbol{n}_{in_2},$$

and $\boldsymbol{v_o} \in L^2(\Omega_c)$.

In this case, our training set Λ comprises of 100 values of parameters, chosen randomly. We collect the snapshots by solving the problem (2.8) with $\mathbb{P}2-\mathbb{P}1-\mathbb{P}2$ discretization and Newton method for all $\boldsymbol{\mu} \in \Lambda$. We report a few state velocity and control snapshots for

$\mu = (70.512, 45.949)$, $\mu = (78.709, 46.289)$ and $\mu = (72.212, 48.930)$ in figure 4.3.9. It is to be noted that in this case, control is not only the outflow conditions needed at either one of the outlets but the outflow conditions needed at both Γ_{o_1} and Γ_{o_2} altogether, to match $\boldsymbol{v}$ with $\boldsymbol{v}_o$, defined by equation (4.2) with $v_{const} = 350\ mm/s$. The eigenvalues

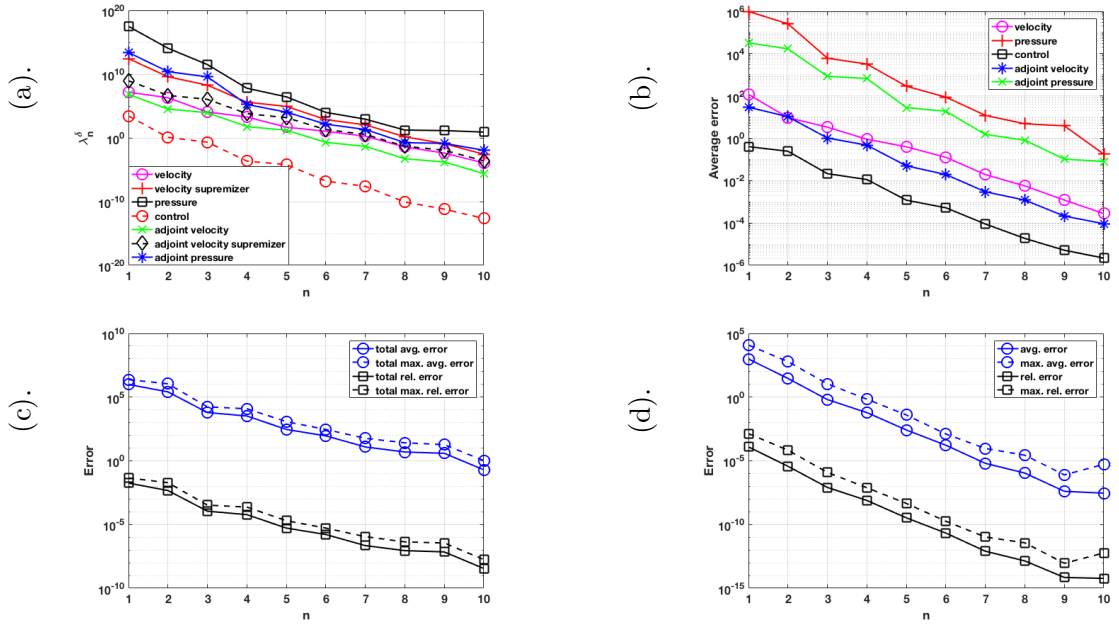

Figure 4.3.8: (a). Eigenvalues' reduction. (b). Average error between FE and POD–Galerkin approx. of $\boldsymbol{\delta} = \boldsymbol{v}, p, \boldsymbol{u}, \boldsymbol{w}, q$. (c). Total error between Galerkin FE and POD–Galerkin approximations. (d). Error between FE and POD–Galerkin reduction of $\mathcal{J}$.

arranged in decreasing order in figure 4.3.8(a) show that 99.9 % energy of full order spaces is successfully captured in 10 eigenvalues, thus we can generate reduced order spaces from $\mathrm{N}_{max} = 10$ POD modes. The offline phase finishes with construction of the POD modes and costs $26,881.7$ seconds.

In the online phase, at a generic k^{th}–iteration, we solve the reduced order optimal flow control system given in equation (3.25) for $\boldsymbol{\mu} = (80, 50)$ and report the reduced order approximations of state velocity and control in figure 4.3.10. Galerkin finite element approximations of the state velocity and control for $\boldsymbol{\mu} = (80, 50)$ are shown in figure 2.2 case II (c). Here, we again make the comparison between the Galerkin finite element method and POD–Galerkin method and remark that the approximated solutions achieved by the two methods are the same, hence verifying the accuracy of POD–Galerkin.

We report a reduction from 10^2 to approximately 10^{-4} and from 10^6 to approximately 10^{-1} in error for velocity and pressure approximations (figure 4.3.8(b)). $\mathcal{E}_{\boldsymbol{u}}$ decreases approximately to 10^{-6} and a similar behavior is observed for adjoint velocity and adjoint

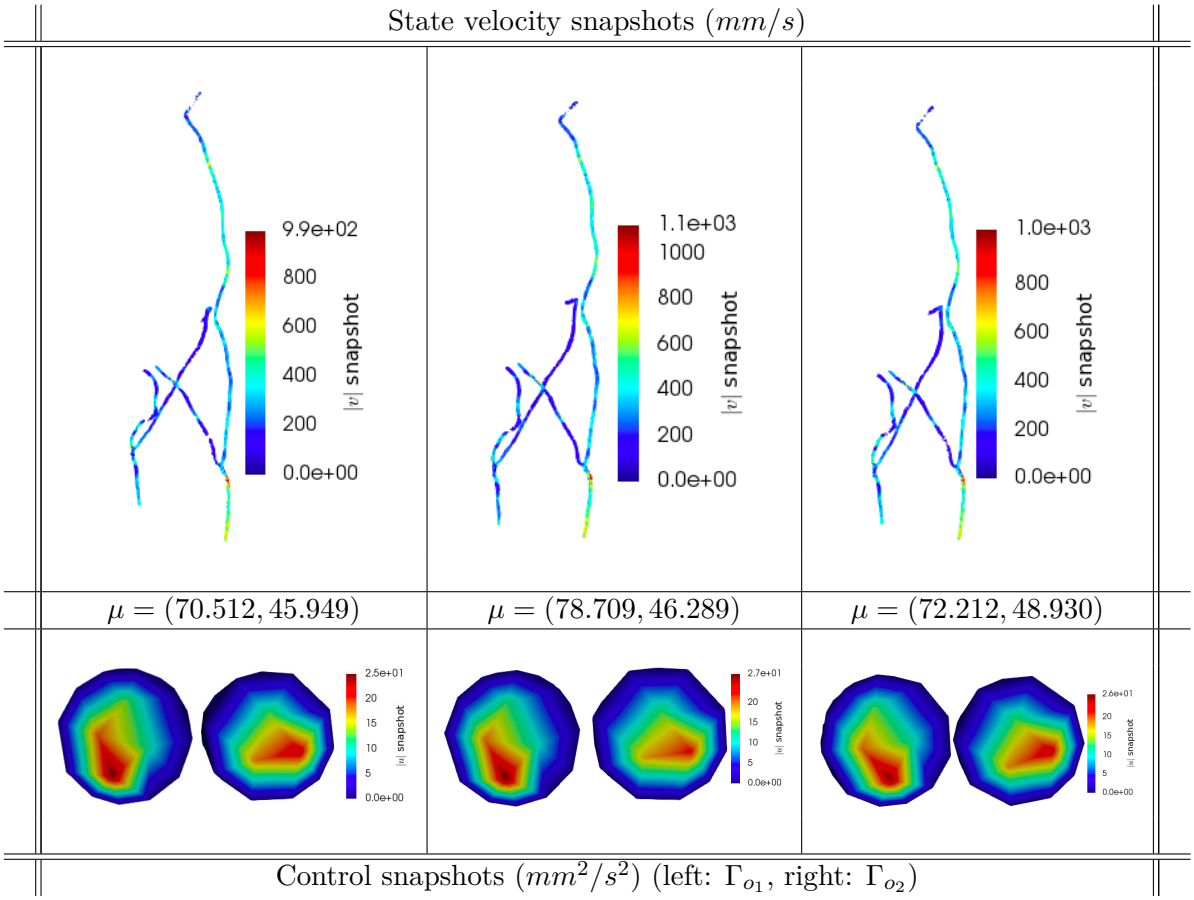

Figure 4.3.9: Case II: Snapshots of state velocity (mm/s) and boundary control magnitude (mm^2/s^2) for $\mu = (70.512, 45.949)$, $\mu = (78.709, 46.289)$ and $\mu = (72.212, 48.930)$ (from left to right).

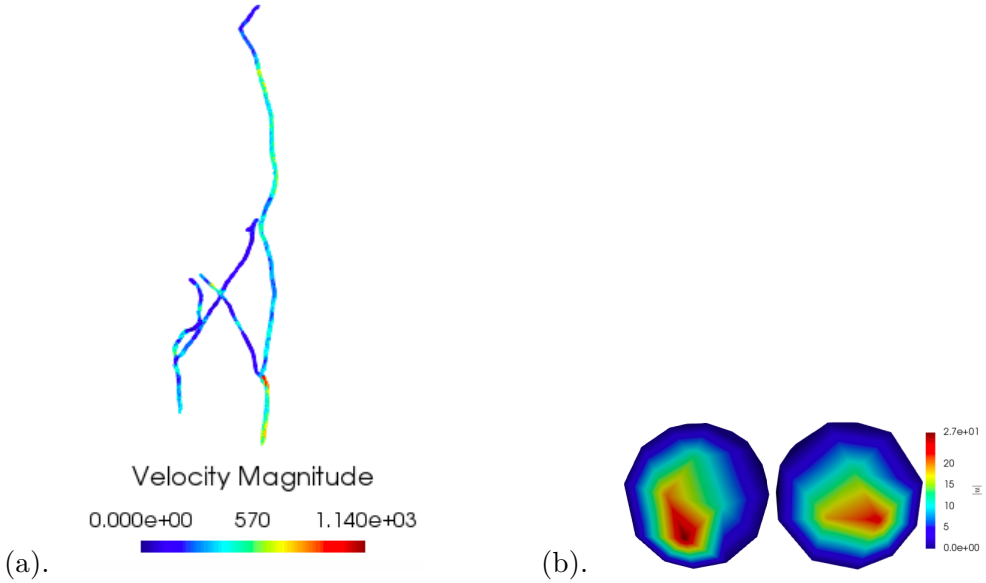

(a). (b).

Figure 4.3.10: Case II: (a). POD–Galerkin approx. of state velocity (mm/s). (b). Boundary control magnitude (mm^2/s^2).

pressure (figure 4.3.8(c)). Total error $\mathcal{E}_T$ reduces from 10^6 to approximately 10^{-1} with a decrease from 10^{-1} to approximately 10^{-8} in corresponding total relative error (figure 4.3.8(c)). Furthermore, the difference between Galerkin FE and POD–Galerkin approximations of $\mathcal{J}$ decreases to about 10^{-7} for $n = 10$ (figure 4.3.8(d)). The computational performances in the three cases with Navier-Stokes constrained optimal flow control problem are reported in table 4.2.

Concluding remarks

In this chapter, we have applied the reduced order framework constructed for Stokes and Navier-Stokes constrained optimal flow control problems in chapter 3 to the patient-specific geometrical models of coronary artery bypass grafts. We make a few remarks concerning the computational performances observed in the numerical results obtained:

(i). In case of Stokes constrained optimal flow control problem, we observe a speed up of $\mathcal{O}\left(10^4\right)$ maximum speed up through POD–Galerkin. In this case, the offline phase takes $\mathcal{O}\left(10^3\right)$ seconds while the online phase only takes $\mathcal{O}\left(10^1\right)$ seconds. We remark that the CPU time is reduced by $\mathcal{O}\left(10^2\right)$ seconds in this case.

(ii). In the case of Navier-Stokes constrained optimal flow control problem, we have considered three different geometries comprising of single and double graft connections.

		Case I(a)	Case I(b)	Case II
Mesh size		42354	27398	605451
Galerkin finite element dofs ($\mathcal{N}$)		433288	280274	715462
No. of reduced order bases N		79	79	132
$\mathcal{D}$		$[70, 80]$	$[45, 50]$	$[70, 80] \times [45, 50]$
$\lvert\Lambda\rvert$		100	100	100
Comp. time	Galerkin FE	1214.3 seconds	634 seconds	1848.13 seconds
	offline phase	16825.9 seconds	12106.8 seconds	26881.7 seconds
	online phase	109.3 seconds	118 seconds	202.27 seconds

Table 4.2: Computational performances for Navier-Stokes constrained optimal flow contol: case I(a), case I(b), case II.

We observe a reduction of $\mathcal{O}\left(10^2\right)$ seconds in computational time as compared to Galerkin finite element solutions of these cases (see chapter 2, section 2.6).

(*iii*). Furthermore, we remark that the absolute relative error in the solution variables in all three cases is reduced upto $\mathcal{O}\left(10^{-8}\right)$. A reduction upto $\mathcal{O}\left(10^{-14}\right)$ is observed for the absolute relative error in the objective functional. Thus, in these applications, the reduced order methods attain the same accuracy as full-order methods.

(*iv*). Lastly, we remark that in the case of double graft connections, the control accounts for the combined outflow conditions at the two outlets Γ_{o_1} and Γ_{o_2}.

We remark that in this work, we have utilized arbitrary values for velocity desired to be matched through the optimal flow control framework in the real-patient cardiovascular geometries. It is of interest to further assimilate the framework with real-patient physiological data in time acquired from 4D-flow MRIs. We presume this data to be blood flow velocity or blood flow rate and to be measured in a sub-region of coronary artery bypass grafts. Then, the clinical problem of interest will be to match the provided medical data of a specific patient in the geometrical models of the specific patient, reconstructed from corresponding clinical images. From mathematical perspective, we propose taking different slices/sections of the domain into account according to the sub-region of interest. Thanks to the local knowledge of the centerlines, we propose identification of degrees of freedom in these sections and the physiological measurements can be projected onto solution spaces and assimilated in the discussed mathematical framework through expression (4.2).

In such real-life clinical problems, the full order simulations discussed in chapter 2 can be used if a single clinical scenario is under consideration, for instance, if the clinicians are interested in matching the clinical measurements when the exact inflow velocity is known. Whereas, if the medical problem of interest is to study the effect of different inflow velocities on flow behavior when matching the desired data, using only full order simulations will

not be computationally convenient anymore. In such cases, the reduced order framework introduced in chapter 3 can be applied to attain simulations in time-efficient and reliable manner.

Chapter 5

Concluding remarks and future perspectives

***

5.1. Concluding remarks

In this thesis, we have constructed a projection-based reduced order framework for parametrized optimal flow control problems and we have shown its applications in the clinical case of real-life coronary artery bypass surgery. The work presented in this thesis relies on three parts, that are, (*i*). construction of geometrical models for patient-specific coronary artery bypass grafts from clinical images, (*ii*). construction of an optimal flow control framework with data assimilation proposed for patient-specific physiological data and (*iii*). implementation of reduced order methods in the optimal flow control framework in many-query parameter-dependent settings. We summarize the thesis below:

- We have covered the first part, that is, the patient-specific geometrical reconstruction from clinical images, in the chapter 1 for the case of triple coronary artery bypass grafts surgery. In the section 1.5, we have briefly summarized the algorithm implemented for the purpose. The steps taken into account include pre-processing, level sets segmentation, surface generation through marching cube algorithm, extraction and smoothing of centerlines, maximum inscribed radii polyballs insertion, decapping and tetrahedral mesh generation. Each step relies on a modeling or a programming library, for example, the first few steps rely on VMTK [12, 84], the smoothing of centerlines and the polyballs insertion relies on python-based programming in VMTK and VTK [97], the decapping step is performed with the help of ParaView [5] and VMTK and finally the mesh generation uses TetGen. Furthermore, the pre-processing step constitutes of three stages, namely, resampling, smoothing and enhancement. At the resampling stage we augment the resolution of acquired image to match it with the image segmentation procedure, for example, level sets segmentation, then at the smoothing step, we apply anisotropic diffusion filter to remove high-frequency noise

from the image and at the enhancement step, vessel enhancement filters are applied to make the vessel-shaped structures more visible.

- For the second part, that is, the construction of a numerical optimal flow control pipeline, we refer the reader to chapter 2. Firstly, we have cast the constrained problem into and unconstrained problem by introducing new unknown variables, the Lagrange multipliers or adjoint variables. Then, utilizing first order Karush-Kuhn-Tucker optimality conditions, we have derived the optimal flow control problem in a coupled optimality system that comprises of three coupled equations namely state equation, optimality equation and adjoint equation. Then, we have introduced the nested saddle-point formulation of Stokes and Navier-Stokes constrained boundary control problems. The saddle-point framework gives rise to a compact block structure which eases the formulation and computations in the discretized settings. We have shown the existence of unique and stable solution to such problems through Brezzi's theorem and we have remarked that the theorem will hold true as long as the spaces are chosen with care and with some restrictions, that is, the equivalence relation between state and adjoint spaces.

  Afterwards, we have numerically approximated the optimal flow control problems using Galerkin finite element methods. We reiterate that if the finite element spaces are chosen such that the discrete state spaces are equivalent to the discrete adjoint spaces, then the existence of unique solution can be guaranteed through Brezzi's theorem. In the last section of this chapter, we have applied the numerical optimal flow control framework to the case of triple coronary artery bypass grafts surgery, introduced in chapter 1. Through these applications, we have shown the computational cost for a single simulation is at least $\mathcal{O}\left(10^2\right)$ seconds and for mesh size of $\mathcal{O}\left(10^4\right)$ to $\mathcal{O}\left(10^5\right)$, the finite element degrees of freedom are of $\mathcal{O}\left(10^5\right)$.

- The third part, that is, the implementation of reduced order methods in the optimal flow control framework, has been covered in chapter 3. We have constructed the reduced order spaces following POD–Galerkin for Stokes and Navier-Stokes constrained optimal flow control problems. The construction of these spaces has been based upon energy of *snapshots*, which are taken to be Galerkin finite element solutions to the discrete problem. The parametrization considered in these cases is physical, that is Reynolds number, as their tuning can generate different flow velocities at the inlets, which can be considered as different viscosity based scenarios. Furthermore, we have shown some test cases for idealized Y-shaped geometry, that can be considered similar to a Y-graft. These tests are made in comparison to similar tests made by using only full-order methods in chapter 2.

- In chapter 4, we have applied the reduced order framework constructed in chapter 3 to the clinical case of triple coronary artery bypass grafts. We have considered three different cases with two dealing with single coronary artery bypass grafts each and

the third one dealing with two coronary artery bypass grafts. The parametrization considered in this case is in Reynolds number that generate the inflow velocity. Furthermore, we have made the comparisons in term of computational costs and the dimensions of solution spaces with the cardiovascular applications demonstrated in chapter 2.

The numerical results for the application of full-order methods for optimal flow control problems in patient-specific cardiovascular geometries show that for a sufficiently fine mesh size, required for the accuracy of these methods, the number of degrees of freedom is usually large. This is because of the fact that we have additional unknown variables, that are, the adjoint variables, because of the equivalence condition between state and adjoint spaces and because of stable finite element pair of spaces for velocity and pressure, that is generic Lagrange bases comprising of piecewise polynomials of degree 2 for velocity and $\mathbb{P}1$ for pressure. We also analyze the computational time, which is of $\mathcal{O}\left(10^3\right)$ seconds in these applications. This order of computational effort is not expensive for a single simulation, however, this is not the case in cardiovascular problems. It is inevitable to consider many hemodynamics scenarios against different tunings of a flow parameter, to accurately model the hemodynamics for the specific patient. In such problems, spending a computational time of $\mathcal{O}\left(10^3\right)$ seconds repeatedly is quite expensive.

The reduced order methods implemented to address this issue show a reduction in computational cost in terms of CPU time from $\mathcal{O}\left(10^3\right)$ to $\mathcal{O}\left(10^1\right)$ seconds while approximating the numerical solution in the spaces generated from $\mathcal{O}\left(10^2\right)$ bases rather than the spaces comprising of $\mathcal{O}\left(10^5\right)$ degrees of freedom. These results also showed the reduced order methods to preserve the accuracy of Galerkin finite element method. Furthermore, thanks to the affine decomposition assumption, we have decoupled the computational procedured in offline-online phases. The offline phase required high computational effort but since it needs to be performed only once, the effort is necessary and bearable for the applications comprising of parametrized problems. We also remark that the optimal flow control framework satisfactorily quantifies the unknown outflow conditions needed to match the desired data, as is shown by the results for cardiovascular applications in chapter 2.

5.2. Future perspectives

In this section, we will close this thesis with proposing some possible future directions for the extension of this work.

- *Patient-specific data assimilation.* In this work, we have assimilated the optimal flow control framework with arbitrary desired data for the cardiovascular applications. A near-future possible extension of this work is to assimilate the reduced order parametrized optimal flow control framework with patient-specific physiological data to be acquired from 4D-flow MRIs [33].

- *Time-dependent optimal control problems.* Furthermore, in this work, we have constructed the reduced order framework for steady state optimal flow control problems into account, ignoring the time-dependency of coronary flow owing to their small diameter. A possible extension is to construct a reduced order framework based upon the monolithic structured optimality system for all-at-once solution of time-dependent optimal flow control problems [98, 100]. These problems can be applied to aorto-coronary bypass grafts cases in which aorta having large diameter is involved.

- *Surrogate lumped parameter network models in boundary conditions.* Another extendable direction for this work is to implement the control through surrogate lumped parameter network models at the boundaries rather than simpler Neumann conditions. We anticipate more accuracy in the reduction of objective functional and better approximation of hemodynamics variables through this implementation.

- *Fluid-structure interaction (FSI) problems.* Lastly, we remark that in this work we have considered fixed geometrical models and the vessel walls to be rigid. Thus, this work does not take into account the fluid-structure interaction, which is necessary to consider for accurate computational hemodynamics models. Therefore, we propose that a possible future direction for the extension of this work is towards FSI problems [21, 20].

Bibliography

***

[1] multiphenics – easy prototyping of multiphysics problems in fenics. `https://mathlab.sissa.it/multiphenics`. 2019.

[2] RBniCS – reduced order modelling in FEniCS. `https://mathlab.sissa.it/rbnics`. 2019.

[3] V. Agoshkov, A. Quarteroni, and G. Rozza. A mathematical approach in the design of arterial bypass using unsteady Stokes equations. *Journal of Scientific Computing*, 28(2-3):139–165, 2006.

[4] V. Agoshkov, A. Quarteroni, and G. Rozza. Shape design in aorto-coronaric bypass anastomoses using perturbation theory. *SIAM Journal on Numerical Analysis*, 44(1):367–384, 2006.

[5] J. Ahrens, B. Geveci, and C. Law. *ParaView: An End-User Tool for Large Data Visualization, Visualization Handbook*. Elsevier, 2005.

[6] C. Airiau, A. Bottaro, S. Walther, and D. Legendre. A methodology for optimal laminar flow control: Application to the damping of tollmien–schlichting waves in a boundary layer. *Physics of Fluids*, 15(1131-1145), 2003.

[7] R. W. Alexander and G. C. Griffith. Anomalies of the coronary arteries and their clinical significance. *Circulation*, 14:800–805, 1956.

[8] S. Ali. *Stabilized reduced basis methods for the approximation of parametrized viscous ows*. PhD thesis, SISSA, International School for Advanced Studies, 2018.

[9] S. Ali, F. Ballarin, and G. Rozza. Stabilized reduced basis methods for parametrized steady Stokes and Navier-Stokes equations. Submitted, 2019.

[10] M. S. Alnæs, J. Blechta, J. Hake, A. Johansson, B. Kehlet, A. Logg, C. Richardson, J. Ring, M. E. Rognes, and G. N. Wells. The fenics project version 1.5. *Archive of Numerical Software*, 3(100):9–23, 2015.

[11] L. Antiga, J. Peiŕo, and D. A. Steinman. *Cardiovascular Mathematics: Modeling and simulation of the circulatory system*, chapter From image data to computational domains. Springer-Verlag Italia, Milano, 2009.

[12] L. Antiga, M. Piccinelli, L. Botti, B. Ene-Iordache, A. Remuzzi, and D. A. Steinman. An image-based modeling framework for patient-specific computational hemodynamics. *Medical & Biological Engineering & Computing*, 46(11):1097–1112, 2008.

[13] G. Arbia, I. Vignon-Clementel, T.-Y. Hsia, and J.-F. Gerbeau. Modified navier-stokes equations for the outflow boundary conditions in hemodynamics. *European Journal of Mechanics - B/Fluids, Elsevier*, 60:175–188, 2016.

[14] F. Auricchio, M. Conti, A. Lefieux, S. Morganti, A. Reali, G. Rozza, and A. Veneziani. *Cardiovascular Mechanics*, chapter Computational Methods in Cardiovascular Mechanics, page 54. CRC Press Taylor and Francis Group, 2018.

[15] I. Babuška. Error-bounds for finite element method. *Numerische Mathematik*, 16(4):322–333, 1971.

[16] E. Bader, M. Kärcher, M. Grepl, and K. Veroy. Certified reduced basis methods for parametrized distributed elliptic optimal control problems with control constraints. *SIAM Journal on Scientific Computing*, 38(6):A3921–A3946, 2016.

[17] F. Ballarin, E. Faggiano, S. Ippolito, A. Manzoni, A. Quarteroni, G. Rozza, and R. Scrofani. Fast simulations of patient-specific haemodynamics of coronary artery bypass grafts based on a POD-Galerkin method and a vascular shape parametrization. *Journal of Computational Physics*, 315:609–628, 2016.

[18] F. Ballarin, E. Faggiano, A. Manzoni, A. Quarteroni, G. Rozza, S. Ippolito, C. Antona, and R. Scrofani. Numerical modeling of hemodynamics scenarios of patient-specific coronary artery bypass grafts. *Biomechanics and Modeling in Mechanobiology*, 16(4):1373–1399, 2017.

[19] F. Ballarin, A. Manzoni, A. Quarteroni, and G. Rozza. Supremizer stabilization of POD–Galerkin approximation of parametrized steady incompressible Navier–Stokes equations. *International Journal for Numerical Methods in Engineering*, 102(5):1136–1161, 2015.

[20] F. Ballarin and G. Rozza. POD–Galerkin monolithic reduced order models for parametrized fluid-structure interaction problems. *International Journal for Numerical Methods in Fluids*, 82(12):1010–1034, 2016.

[21] F. Ballarin, G. Rozza, and Y. Maday. volume 17, chapter Reduced-order semi-implicit schemes for fluid-structure interaction problems, pages 149–167. Springer International Publishing, 2017.

[22] M. Benzi, G. H. Golub, and J. Liesen. Numerical solution of saddle point problems. *Acta Numerica*, (1-137), 2005.

[23] A. Bermudez. Some applications of optimal control theory of distributed systems. *ESAIM: Control, Optimisation and Calculus of Variations*, 8:129–151, 2002.

[24] C. Bertolotti and V. Deplano. Three-dimensional numerical simulations of flow through a stenosed coronary bypass. *Journal of Biomechanics*, 33:1011–1022, 2000.

[25] P. Bhatnagar, K. Wickramasinghe, E. Wilkins, and N. Townsend. Trends in the epidemiology of cardiovascular disease in the uk. *Heart. British Cardiovascular Society Journals*, 102:1945–1952, 2016.

[26] P. B. Bochev and M. D. Gunzburger. Least-squares finite-element methods for optimization and control problems for the stokes equations. *Computers and Mathematics with Applications*, 48(1035-1057), 2004.

[27] P. B. Bochev and M. D. Gunzburger. *Least-Squares Finite Element Methods*, volume 166 of *Applied Mathematical Sciences*. Springer Science+Business Media, 2009.

[28] M. Bonert, J. G. Myers, S. Fremes, J. Williams, and C. R. Ethier. A numerical study of blood flow in coronary artery bypass graft side-to-side anastomoses. *Annals of Biomedical Engineering*, 30(5):599–611, May 2002.

[29] E. Boutsianis, H. Dave, T. Frauenfelder, D. Poulikakos, S. Wildermuth, M. Turina, Y. Ventikos, and G. Zund. Computational simulation of intracoronary flow based on real coronary geometry. *European Journal of Cardio-Thoracic Surgery*, 26(2):248–256, 2004.

[30] F. Brezzi. On the existence, uniqueness and approximation of saddle-point problems arising from lagrangian multipliers. *Revue française d'automatique, informatique, recherche opérationnelle. Analyse numérique*, 8:129–151, 1974.

[31] F. Cacho, M. D. é, and G. A. Holzapfel. A procedure to simulate coronary artery bypass graft surgery. *Medical & Biological Engineering & Computing*, 45:819–827, 2007.

[32] I. Clementel, C. A. Figueroa, K. E. Jansen, and C. A. Taylor. Outflow boundary conditions for 3d simulations of non-periodic blood flow and pressure fields in deformable arteries. *Computer Methods in Biomechanics and Biomedical Engineering*, pages 1–10, 2010.

[33] F. Condemi, S. Fremes, P. Triverio, and L. Jimenez-Juan. On the use of 4d flow mri to create patient-specific computational fluid dynamics models for patients with coronary artery bypass surgery. In *22nd Annual Scientific Sessions, Society for Cardiovascular Magnetic Resonance, Bellevue, WA*. 2019.

[34] L. Dedè. Optimal flow control for navier-stokes equations: Drag minimization. *International Journal for Numerical Methods in Fluids*, 55(4):347 – 366, 2007.

[35] L. Dedè. Reduced basis method and error estimation for parametrized optimal control problems with control constraints. *Journal of Scientific Computing*, 50(2):287–305, 2012.

[36] M. D'Elia, M. Perego, and A. Veneziani. A variational data assimilation procedure for the incompressible navier-stokes equations in hemodynamics. *Journal of Scientific Computing*, 52(340-359), 2012.

[37] V. Deplano, C. Bertolotti, and O. Boiron. Numerical simulations of unsteady flows in a stenosed coronary bypass graft. *Medical & Biological Engineering & Computing*, 39:488–499, 2001.

[38] E. Earl and H. Mohammadi. *Biomechanics*, volume 4 of *InTechOpen Book Series, Biomedical Engineering*, chapter Biomechanics of Human Blood. InTechOpen, 2019.

[39] M. Fioranelli, A. G. Bottacciaoli, F. Bottacciaoli, M. Bianchi, M. Rovesti, and M. G. Roccia. Stress and inflammation in coronary artery disease: A review psychoneuroendocrineimmunology-based. *Frontiers in immunology*, 9(2031):1–15, 2018.

[40] D. M. Fiss. Normal coronary anatomy and anatomic variations. *Applied Radiolodolgy, the journal of practical medical imaging and management.*, 2007.

[41] L. Formaggia, A. Quarteroni, and A. Veneziani. *Complex Systems in Biomedicine*, chapter The circulatory system: from case studies to mathematical modelling, pages 243–287. Springer, Milan, 2006.

[42] L. Formaggia, A. Veneziani, and C. Vergara. A new approach to numerical solution of defective boundary value problems in incompressible fluid dynamics. *SIAM Journal on Numerical Analysis*, 46(6):2769–2794, 2008.

[43] J. Ghiglieri and S. Ulbrich. Optimal flow control based on pod and mpc and an application to the cancellation of tollmien-schlichting waves. *Optimization Methods and Software*, 00(00):1–34, 2012.

[44] D. N. Ghista and F. Kabinejadian. Coronary artery bypass grafting hemodynamics and anastomosis design: a biomedical engineering review. *BioMedical Engineering OnLine*, 12(129), 2013.

[45] S. E. Greenwald and C. L. Berry. Improving vascular grafts: the importance of mechanical and haemodynamic properties. *The Journal of Pathology*, 190(3):292–299, 2000.

[46] M. D. Gunzburger. *Perspectives in flow control and optimization*. SIAM, Philadelphia, 2003.

[47] M. D. Gunzburger, L. S. Hou, and T. P. Svobodny. *Optimal Control of Viscous Flow*, chapter Optimal Control Problems for a Class of Nonlinear Equations With an Application to Control of Fluids. Other Titles in Applied Mathematics. SIAM, Philadelphia, 1998.

[48] J. A. Henriquez-Pino, W. J. Gomes, J. C. Prates, and E. Buffolo. Surgical anatomy of the internal thoracic artery. *The Annals of Thoracic Surgery*, 64:1041–1045, 1997.

[49] J. S. Hesthaven, G. Rozza, and B. Stamm. *Certified Reduced Basis methods for parametrized partial differential equations*. SpringerBriefs in Mathematics. Springer International Publishing, 2015.

[50] J. G. Heywood, R. Rannacher, and S. Turek. Artificial boundaries and flux and pressure conditions for the incompressible navier-stokes equations. *International Journal for Numerical Methods in Fluids*, 22:325–352, 1996.

[51] S. Hijazi, S. Ali, G. Stabile, F. Ballarin, and G. Rozza. The effort of increasing reynolds number in projection-based reduced order methods: from laminar to turbulent flows. 2018.

[52] M. Hinze, R. Pinnau, M. Ulbrich, and S. Ulbrich. *Optimization with PDE constraints*. Springer, 2009.

[53] L. Hou and S. Ravindran. Numerical approximation of optimal flow control problems by a penalty method: Error estimates and numerical results. *SIAM Journal on Scientific Computing*, 20(5):1753–1777, 1999.

[54] K. Ito and K. Kunisch. Lagrange multiplier approach to variational problems and applications. *Advances in Design and Control. SIAM.*, 2008.

[55] K. Ito and S. Ravindran. A reduced-order method for simulation and control of fluid flows. *Journal of Computational Physics*, 143:403–425, 1998.

[56] K. Ito and S. S. Ravindran. A reduced basis method for control problems governed by pdes. *International Series of Numerical Mathematics - Springer*, 126:153–168, 1998.

[57] K. Ito and S. S. Ravindran. Reduced basis method for optimal control of unsteady viscous flows. *International Journal for Computational Fluid Dynamics*, 15:97–113, 2001.

[58] G. J. d. Jonge, P. M. A. van Ooijen, L. H. Piers, R. Dikkers, R. A. Tio, T. P. Willems, A. F. M. van den Heuvel, F. Zijlstra, and M. Oudkerk. Visualization of anomalous coronary arteries on dual-source computed tomography. *European Radiology*, 18:2425–2432, 2007.

[59] R. Y. Kannan, H. J. Salacinski, P. E. Butler, G. Hamilton, and A. M. Seifalian. Current status of prosthetic bypass grafts: A review. *Journal of Biomedical Materials Research*, 74B(1):570–581, 2005.

[60] M. Kärcher, Z. Tokoutsi, M. A. Grepl, and K. Veroy. Certified reduced basis methods for parametrized elliptic optimal control problems with distributed controls. *Journal of Scientific Computing*, 75(1):276–307, 2018.

[61] H. J. Kim, I. E. Vignon-Clementel, J. S. Coogan, C. A. Figueroa, K. E. Janson, and C. A. Taylor. Patient-specific modeling of blood flow and pressure in human coronary arteries. *Annals of Biomedical Engineering*, 38(10):3195–3209, 2010.

[62] Y.-H. Kim, D.-W. Park, J.-Y. Lee, W.-J. Kim, S.-C. Yun, J.-M. Ahn, H. G. Song, J.-H. Oh, J. S. Park, S.-J. Kang, S.-W. Lee, C. W. Lee, S.-W. Park, and S.-J. Park. Impact of angiographic complete revascularization after drug-eluting stent implantation or coronary artery bypass graft surgery for multivessel coronary artery disease. *Circulation*, 123(21):2373–2381, 2011.

[63] T. S. Koltukluoğlu and P. J. Blanco. Boundary control in computational hemodynamics. *Journal of Fluid Mechanics*, 847:329–364, 2018.

[64] J. P. Ku, M. T. Draney, F. R. Arko, W. A. Lee, F. P. Chan, N. J. Pelc, C. K. Zarins, and C. A. Taylor. In vivo validation of numerical prediction of blood flow in arterial bypass grafts. *Annals of Biomedical Engineering*, 30:743–752, 2002.

[65] K. Kunisch and S. Volkwein. Proper orthogonal decomposition for optimality systems. *ESAIM: Mathematical Modelling and Numerical Analysis*, 42(1):1–23, 2008.

[66] T. Lassila, A. Manzoni, A. Quarteroni, and G. Rozza. A reduced computational and geometrical framework for inverse problems in hemodynamics. *International Journal for Numerical Methods in Biomedical Engineering*, 29(7):741–776, 2013.

[67] T. Lassila, A. Manzoni, A. Quarteroni, and G. Rozza. oundary control and shape optimization for the robust design of bypass anastomoses under uncertainty. In A. Quarteroni and G. Rozza, editors, *Reduced Order Methods for Modeling and Computational Reduction*, volume 9, pages 235–274. Springer MS&A Series, 2014.

[68] P. Libby. Inflammation and cardiovascular disease mechanisms. *American Journal of Clinical Nutrition*, 83:456S–460S, 2006.

[69] P. Libby and P. Theroux. Pathophysiology of coronary artery disease. *Circulation*, 111(3481-3488), 2005.

[70] J. L. Lions. Optimization pour certaines classes d'équations d'évolution non linéaires. *Annali di Matematica Pura ed Applicata*, 72:275–294, 1966.

[71] J. L. Lions. *Optimal Control of Systems Governed by Partial Differential Equations*, volume 170 of *Grundlehren der mathematischen Wissenschaften*. Springer-Verlag Berlin Heidelberg, 1971.

[72] J. L. Lions. *Some Aspects of the Optimal Control of Distribuited Parameter Systems*. SIAM, Philadelphia, 1972.

[73] A. Logg, K.-A. Mardal, G. N. Wells, et al. *Automated Solution of Differential Equations by the Finite Element Method*. Springer, 2012.

[74] A. Logg, G. N. Wells, and J. Hake. Dolfin: a c++/python finite element library. In K.-A. M. A. Logg and G. N. Wells, editors, *Automated Solution of Differential Equations by the Finite Element Method*, volume 84 of *Lecture Notes in Computational Science and Engineering*. Springer, 2012.

[75] H. Manninen, P. Jaakkola, M. Suhonen, S. Rehnberg, R. Vuorenniemi, and P. Matsi. Angiographic predictors of graft patency and disease progression after coronary artery bypass grafting with arterial and venous grafts. *The Annals of Thoracic Surgery*, 66(4):1289–1294, 1998.

[76] R. E. Mates, R. L. Gupta, A. C. Bell, and F. J. Klocke. Fluid dynamics of coronary artery stenosis. *Circulation Research*, 42(1):152–162, 1978.

[77] C. D. Mathers and D. Loncar. Projections of global mortality and burden of disease from 2002 to 2030. *PLoS Medicine*, 3(11):e442, 2006.

[78] D. Mozaffarian, E. Benjamin, A. Go, D. Arnett, and et al. Heart disease and stroke statistics–2015 update: a report from the american heart association. *Circulation*, 131(4):e29–322, 2015.

[79] M. Müller. On the pod method: An abstract investigation with applications to reduced-order modeling and suboptimal control. Master's thesis, Georg-August-Universität zu Göttingen, 2008.

[80] E. G. Nabel and E. Braunwald. A tale of coronary artery disease and myocardial infarction. *The New England Journal of Medicine*, 366:54–63, 2012.

[81] F. Negri, A. Manzoni, and G. Rozza. Reduced basis approximation of parametrized optimal flow control problems for the stokes equations. *Computers & Mathematics with Applications*, 69(4):319–336, 2015.

[82] F. Negri, G. Rozza, A. Manzoni, and A. Quarteroni. Reduced basis method for parametrized elliptic optimal control problems. *SIAM Journal on Scientific Computing*, 35(5):A2316–A2340, 2013.

[83] A. A. Owida, H. Do, and Y. S. Morsi. Numerical analysis of coronary artery bypass grafts: An over view. *Computer Methods and Programs in Biomedicine*, 108:689–705, 2012.

[84] M. Piccinelli, A. Veneziani, D. A. Steinman, A. Remuzzi, and L. Antiga. A framework for geometric analysis of vascular structures: Application to cerebral aneurysms. *IEEE Transactions on Medical Imaging*, 28(8):1141–1155, 2009.

[85] A. Politis, G. Stavropoulos, M. Christolis, F. P. N. Vlachos, and N. Markatos. Numerical modeling of simulated blood flow in idealized composite arterial coronary grafts: Steady state simulations. *Journal of Biomechanics*, 40:1125–1136, 2007.

[86] A. Politis, G. Stavropoulos, M. Christolis, F. P. N. Vlachos, and N. Markatos. Numerical modelling of simulated blood flow in idealized composite arterial coronary grafts: Transient flow. *Journal of Biomechanics*, 41:25–39, 2008.

[87] A. Quarteroni. *Numerical models for differential problems*. Springer-Verlag Italia, Milan, 2009.

[88] A. Quarteroni, A. Manzoni, and F. Negri. *Reduced Basis Methods for Partial Differential Equations: An Introduction*, volume 92. Springer, 2016.

[89] R. M. Romarowski, A. Lefieux, S. Morganti, A. Veneziani, and F. Auricchio. Patient-specific CFD modelling in the thoracic aorta with PC-MRI–based boundary conditions: A least-square three-element Windkessel approach. *International Journal for Numerical Methods in Biomedical Engineering*, 34(11):e3134, 2018.

[90] G. Rozza. On optimization, control and shape design of an arterial bypass. *International Journal for Numerical Methods in Fluids*, 47(10-11):1411–1419, 2005.

[91] G. Rozza. Real-time reduced basis solutions for Navier-Stokes equations: optimization of parametrized bypass configurations. In P. Wesseling, E. Onate, and J. Periaux, editors, *ECCOMAS CFD 2006 Proceedings on CFD*, number 676, pages 1–16. 2006.

[92] G. Rozza. Reduced basis methods for Stokes equations in domains with non-affine parameter dependence. *Computing and Visualization in Science*, 12(1):23–35, 2009.

[93] G. Rozza and A. Quarteroni. Reduced basis approximation for parametrized partial differential equations. In E. Zuazua, C. Le Bris, A. Patera, A. Quarteroni, and T. Hou, editors, *Numerical Models for Differential Equations*, volume vol. 2 of *MS&A, Modelling, Simulation and Application*, pages 556–587. Springer, 2009.

[94] G. Rozza and K. Veroy. On the stability of the reduced basis method for Stokes equations in parametrized domains. *Computer Methods in Applied Mechanics and Engineering*, 196(7):1244–1260, 2007.

[95] S. Sankaran, J. D. Humphrey, and A. L. Marsden. An efficient framework for optimization and parameter sensitivity analysis in arterial growth and remodeling computations. *Computer Methods in Applied Mechanics & Engineering*, 256:200–210, 2013.

[96] S. Sankaran, M. E. Moghadam, A. M. Kahn, E. E. Tseng, J. M. Guccione, and A. L. Marsden. Patient-specific multiscale modeling of blood flow for coronary artery bypass graft surgery. *Annals of Biomedical Engineering*, 40(12):2228–2242, 2012.

[97] W. Schroeder, K. Martin, and B. Lorensen. *The Visualization Toolkit: An Object-oriented Approach to 3D Graphics*. Kitware, 4 edition, 2006.

[98] M. Stoll and A. Wathen. All-at-once solution of time-dependent stokes control. *Journal of Computational Physics*, 232(1):498–515, 2013.

[99] M. Strazzullo, F. Ballarin, R. Mosetti, and G. Rozza. Model reduction for parametrized optimal control problems in environmental marine sciences and engineering. *SIAM Journal on Scientific Computing*, 40(4):B1055–B1079, 2018.

[100] M. Strazzullo, Z. Zainib, F. Ballarin, and G. Rozza. Reduced order methods for parametrized nonlinear and time dependent optimal flow control problems: applications in biomedical and environmental sciences. In preparation, 2019.

[101] C. A. Taylor and C. A. Figueroa. Patient-specific modeling of cardiovascular mechanics. *Annual Review of Biomedical Engineering*, 11:109–134, 2009.

[102] C. A. Taylor, T. A. Fonte, and J. K. Min. Computational fluid dynamics applied to cardiac computed tomography for noninvasive quantification of fractional flow reserve. *Journal of the American College of Cardiology*, 61(2233-2241), 2013.

[103] A. J. Tector, M. L. McDonald, D. C. Kress, F. X. Downey, and T. M. Schmahl. Purely internal thoracic artery grafts: outcomes. *The Annals of Thoracic Surgery*, 72(2):450–455, 2001.

[104] M. Tezzele, F. Ballarin, and G. Rozza. Combined parameter and model reduction of cardiovascular problems by means of active subspaces and POD-galerkin methods. In D. Boffi, L. F. Pavarino, G. Rozza, S. Scacchi, and C. Vergara, editors, *Mathematical and Numerical Modeling of the Cardiovascular System and Applications*, pages 185–207. Springer International Publishing, Cham, 2018.

[105] M. Thiriet and K. H. Parker. *Cardiovascular Mathematics. Modeling and simulation of the circulatory system*, chapter Physiology and pathology of the cardiovascular system: a physical perspective. Springer-Verlag Italia, Milano, 2009.

[106] J. Tiago, T. Guerra, and A. Sequeira. A velocity tracking approach for the data assimilation problem in blood flow simulations. *International Journal for Numerical Methods in Biomedical Engineering*, 33(10), 2017.

[107] A. Timmis, N. Townsend, C. Gale, R. Grobbee, N. Maniadakis, M. Flather, E. Wilkins, L. Wright, R. Vos, J. Bax, M. Blum, F. Pinto, and P. Vardas. European society of cardiology: Cardiovascular disease statistics 2017. *European Heart Journal*, 39:508–577, 2018.

[108] F. Tröltzsch. *Optimal control of partial differential equations, theory, methods and applications*. American Mathematical Society, 2010.

[109] I. E. Vignon-Clementel, C. A. Figueroa, K. E. Jansen, and C. A. Taylor. Outflow boundary conditions for three-dimensional finite element modeling of blood flow and pressure in arteries. *Computer Methods in Applied Mechanics & Engineering*, 195:3776–3796, 2006.

[110] A. D. Villa, E. Sammut, A. Nair, R. Rajani, R. Bonamini, and A. Chiribiri. Coronary artery anomalies overview: The normal and the abnormal. *World Journal of Radiology*, 8(6):537–555, 2016.

[111] M. Yadav, T. Palmerini, A. Caixeta, M. V. Madhavan, E. Sanidas, A. J. Kirtane, G. W. Stone, and P. Généreux. Prediction of coronary risk by syntax and derived scores: Synergy between percutaneous coronary intervention with taxus and cardiac surgery. *Journal of the American College of Cardiology*, 62(14):1219–1230, 2013.

[112] A. E. Yılmaz. *LES-based optimal flow control with applications to wind turbines*. PhD thesis, Arenberg Doctoral School, Faculty of Engineering Science, KU Leuven, 2019.

[113] Z. Zainib, F. Ballarin, S. Fremes, P. Triverio, L. Jimènez-Juan, and G. Rozza. Reduced order methods for parametric optimal flow control in coronary bypass grafts, towards patient-specific data assimilation. Submitted, 2019.